

Imperial College of Science, Technology and Medicine
Department of Materials

Atomistic Simulation of Fission Products in Zirconia Polymorphs

Alexandros Kenich

Submitted in part fulfilment of the requirements for the degree of
Doctor of Philosophy and the Diploma of Imperial College

April 2019

DECLARATION

I declare that the work presented in this thesis is my own, and that all efforts from others are referenced.

The copyright of this thesis rests with the author and is made available under a Creative Commons Attribution Non-Commercial No Derivatives licence. Researchers are free to copy, distribute or transmit the thesis on the condition that they attribute it, that they do not use it for commercial purposes and that they do not alter, transform or build upon it. For any reuse or redistribution, researchers must make clear to others the licence terms of this work.

Abstract

- The inner oxide of LWR fuel cladding was studied.
- In particular, its role in PCI failures.
- We used quantum mechanical simulation methods to predict defect energies in ZrO_2 .
- We used these energies to determine defect equilibria in the different phases of ZrO_2 .
- The first study was entirely on undoped ZrO_2 . We predicted intrinsic defect energies and equilibria, as well as defect volumes and relative structural stability of the monoclinic, tetragonal and cubic phases.
- Along the way, we found that simulating the cubic phase using QM methods would produce an easily destabilised structure, prone to collapse when defects are introduced.
- The second study was focused on iodine defects in the monoclinic and tetragonal phase.
- We found that there is significant competition between iodine and oxygen for anion sites in the tetragonal phase. This is not the case for the monoclinic phase.
- The third study was about tellurium, iodine, xenon and caesium in the tetragonal phase only.
- We propose a new initiation mechanism for PCI failures, whereby iodine diffuses deep into the ZrO_2 layer, past the monoclinic portion but short of the oxide-metal interface. ZrO_2 in this region of the oxide is predominantly tetragonal phase. The iodine nuclei then decay into xenon nuclei, which are larger and have less coherence with the ZrO_2 matrix. These xenon atoms impose a significant strain locally which will open cracks and initiate new ones. At a critical concentration of iodine, this effect bares enough fresh metal surface such that the corrosive effect of iodine outpaces the development of a passivating oxide layer, leading to failure of the clad.

Acknowledgements

EPSRC, Imperial College HPC, PACE, UoM, Westinghouse, ICO CDT, CNE, Dept. of Materials, wife and family

Contents

| | |
|---|------------|
| Abstract | i |
| Acknowledgements | iii |
| 1 Introduction | 1 |
| 1.1 Nuclear Power | 1 |
| 1.1.1 Fission | 3 |
| 1.1.2 Reactor design | 4 |
| 1.1.3 Nuclear reactor fuel pins | 6 |
| 1.1.4 Effects of radiation on materials | 7 |
| 1.1.5 Fission products, their distribution and decay chains | 8 |
| 1.2 Pellet-cladding interaction (PCI) | 8 |
| 1.2.1 Effect of power ramps | 8 |
| 1.2.2 Pellet-clad gap and bonding | 9 |
| 1.2.3 Iodine corrosion of zirconium | 9 |
| 1.3 Oxidation of zirconium | 9 |
| 1.3.1 Oxygen solubility of zirconium | 9 |
| 1.3.2 Oxide growth mechanism | 10 |
| 1.3.3 Outer oxide vs inner oxide | 10 |
| 1.3.4 Sources of oxygen | 10 |
| 1.4 Atomistic Simulation | 13 |
| 1.4.1 Classical approach - molecular dynamics | 13 |
| 1.4.2 Quantum mechanical approach - DFT | 13 |
| 1.4.3 Band gap | 13 |

| | | |
|----------|--|-----------|
| 2 | Crystallography and Point Defects | 16 |
| 2.1 | ZrO ₂ phases and stabilisation | 16 |
| 2.1.1 | Monoclinic | 17 |
| 2.1.2 | Tetragonal | 18 |
| 2.1.3 | Cubic | 18 |
| 2.1.4 | Other phases | 19 |
| 2.1.5 | Pressure stabilisation (isochoric + autostabilisation) | 22 |
| 2.1.6 | Dopant stabilisation (lower valence cations) | 22 |
| 2.1.7 | Kröger-Vink notation | 23 |
| 3 | Computational Methodology | 24 |
| 3.1 | Density functional theory | 24 |
| 3.1.1 | The Schrödinger equation | 24 |
| 3.1.2 | Kohn-Sham Method | 25 |
| 3.1.3 | Pseudopotentials | 27 |
| 3.2 | Periodic boundaries | 29 |
| 3.2.1 | Bloch's theorem | 29 |
| 3.2.2 | Plane-waves | 31 |
| 3.3 | Computational details | 32 |
| 3.3.1 | Cell dimensions and initialisation | 32 |
| 3.3.2 | Geometry optimisation | 33 |
| 3.3.3 | Convergence criteria for geometry optimisation | 34 |
| 3.3.4 | Charged cell correction | 34 |
| 3.3.5 | Stiffness tensor generation | 35 |
| 3.3.6 | Strain method for defect volumes | 35 |
| 3.3.7 | Isobaric method for defect volumes | 35 |
| 3.4 | Defect equilibria | 36 |
| 3.4.1 | Effect of space charge | 37 |
| 3.5 | Convergence testing | 37 |
| 3.5.1 | Plane-wave cut-off energy | 37 |
| 3.5.2 | k-point convergence | 38 |
| 3.5.3 | Exchange-correlation functionals | 40 |
| 3.5.4 | On-the-fly pseudopotentials | 41 |

| | | |
|----------|--|-----------|
| 3.5.5 | Unit cells | 41 |
| 3.5.6 | Chemical potential of iodine | 42 |
| 3.5.7 | +U study | 43 |
| 4 | Defects | 47 |
| 4.1 | Placeholder | 47 |
| 4.1.1 | Incorporation and defect formation energies | 47 |
| 4.2 | Brouwer diagrams | 50 |
| 4.2.1 | Defect equilibria | 50 |
| 4.2.2 | Oxygen pressure dependence | 51 |
| 5 | Intrinsic defect study | 52 |
| 5.1 | Introduction | 52 |
| 5.1.1 | Applications | 52 |
| 5.1.2 | Crystal structures | 52 |
| 5.1.3 | Previous work | 53 |
| 5.2 | Methodology | 53 |
| 5.2.1 | Simulation parameters | 53 |
| 5.2.2 | Temperature dependence | 53 |
| 5.2.3 | Defect formation energies | 54 |
| 5.2.4 | Brouwer diagrams | 54 |
| 5.3 | Cubic phase collapse | 55 |
| 5.4 | Defect formation energies | 56 |
| 5.5 | Elastic constants and defect relaxation volumes | 56 |
| 5.6 | Helmholtz energies | 58 |
| 5.7 | Defect equilibria | 58 |
| 5.8 | Summary | 60 |
| 6 | Iodine defect equilibria in ZrO_2 | 64 |
| 6.1 | Introduction | 64 |
| 6.1.1 | Iodine stress-corrosion cracking | 66 |
| 6.1.2 | Pellet-cladding interaction | 67 |
| 6.1.3 | Oxygen competition | 67 |
| 6.2 | Methodology | 67 |

| | | |
|----------|---|-----------|
| 6.2.1 | Computational details | 67 |
| 6.2.2 | Incorporation energies | 68 |
| 6.2.3 | Defect Equilibrium Response to Oxygen Partial Pressure | 68 |
| 6.3 | Results | 70 |
| 6.3.1 | Incorporation energies | 70 |
| 6.3.2 | Temperature dependence | 71 |
| 6.3.3 | Dopant concentration dependence | 73 |
| 6.3.4 | Brouwer Diagrams | 74 |
| 6.4 | Summary | 76 |
| 7 | Radioparagenesis of fission products in tetragonal ZrO₂ | 77 |
| 7.1 | Introduction | 77 |
| 7.2 | Methodology | 79 |
| 7.2.1 | Computational Parameters | 79 |
| 7.2.2 | Defect Volumes | 80 |
| 7.2.3 | Defect Equilibrium Response to Oxygen Partial Pressure | 80 |
| 7.3 | Results | 81 |
| 7.3.1 | Brouwer Diagrams | 81 |
| 7.4 | Conclusions | 84 |
| 7.4.1 | Radioparagenesis | 88 |
| 7.4.2 | Site preference of fission products | 90 |
| 7.5 | Methodology | 91 |
| 7.5.1 | Simulation parameters | 91 |
| 7.5.2 | Brouwer diagram generation | 92 |
| 7.5.3 | Defect Volumes | 93 |
| 7.6 | Defect equilibria | 93 |
| 7.6.1 | Tellurium | 93 |
| 7.6.2 | Iodine | 95 |
| 7.6.3 | Xenon | 95 |
| 7.6.4 | Caesium | 97 |
| 7.7 | Summary | 99 |

| | | |
|----------|---|------------|
| 8 | Future work | 100 |
| 8.1 | Fission product empirical potential | 100 |
| 8.2 | Grain boundary transport | 100 |
| 8.3 | Zr/ZrO/ZrO ₂ interface study | 101 |
| | References | 101 |
| | Appendix | 112 |
| A | ParaSweep | 113 |
| B | CASTEP and HPC Scripts | 114 |

List of abbreviations

| | |
|------------|------------------------------------|
| DFT | Density functional theory |
| PCI | Pellet cladding interaction |
| LWR | Light water reactor |
| PWR | Pressurised water reactor |
| BWR | Boiling water reactor |
| GCR | Gas cooled reactor |
| SCC | Stress corrosion cracking |
| NDT | Non destructive testing |
| GGA | Generalised gradient approximation |
| PBE | Perdew-Burke-Ernzerhof |
| LDA | Local density approximation |
| VBM | Valence band maximum |
| CBM | Conduction band minimum |
| DOS | Density of states |
| PP | Pseudopotential |
| RPV | Reactor pressure vessel |

List of Tables

| | | |
|-----|---|----|
| 1.1 | Experimentally determined band gaps alongside values calculated from DFT simulations for each crystal structure of zirconia. Experimental values taken from [1]. | 15 |
| 2.1 | ZrO ₂ crystal structures and their stable temperatures at 1 atm [2]. | 18 |
| 2.2 | Ionic radii of Zr ⁴⁺ and Y ³⁺ in various coordination environments. Values taken from [3]. | 23 |
| 2.3 | Examples of Kröger-Vink notation for several defects in ZrO ₂ | 23 |
| 3.1 | Composition of the supercells in terms of the number of individual unit cells stacked in each direction. | 33 |
| 3.2 | Calculated unit cell parameters for the different crystal structures of ZrO ₂ . Experimental data for pure monoclinic and stabilised tetragonal and cubic phases at 295 K are shown in parentheses [2]. Energy difference between structures is shown with respect to the cubic phase. | 42 |
| 4.1 | Wyckoff positions of interstitial sites used for each crystal structure. | 48 |
| 5.1 | Isolated cluster defect volumes in the three ZrO ₂ structures. | 56 |
| 5.2 | Formation energies in eV of isolated ZrO ₂ defects. | 57 |
| 5.3 | Formation energies of bound defects in ZrO ₂ | 57 |
| 5.4 | Elastic constants for different phases of ZrO ₂ from DFT calculations. | 58 |
| 5.5 | Isolated defect volumes in the three ZrO ₂ structures. | 59 |
| 6.1 | Incorporation energies of neutral iodine interstitials in non-defective supercells. . | 72 |
| 6.2 | Incorporation energies of iodine in oxygen sites of the monoclinic, tetragonal, and cubic ZrO ₂ phases. | 72 |
| 6.3 | Incorporation energies of iodine in zirconium sites of ZrO ₂ | 72 |

| | | |
|-----|---|----|
| 7.1 | Defect volumes and formation energies of the dominant defect types in tetragonal ZrO_2 | 87 |
| 7.2 | Independent fission product yields and half-lives for the major iodine isotopes and precursors in a thermal neutron reactor. Yields from [4, 5]. All isotopes undergo single β^- decay. Metastable states are included. | 88 |

List of Figures

| | | |
|-----|--|----|
| 1.1 | Energy from thermal fission of U-235 as a function of mass ratios of child nuclei. Total energy release includes contributions from gamma rays and subsequent radioactive decays. Taken from [6]. | 2 |
| 1.2 | Plot of neutron number against proton number for nuclei with half-lives greater than 10^{-4} s. Half-life of the dominant decay mode is shown. Taken from [7]. . . . | 4 |
| 1.3 | Plot binding energy per nucleon against mass number. Arrows indicate the reaction shown in equation 1.2. Adapted from [8]. | 5 |
| 1.4 | Partial U-O temperature phase diagram between O/U ratios of 1.2 and 2.25. Figure taken from [9], with phase boundaries from [10–12]. | 11 |
| 1.5 | Plot of the percentage yield of nuclei with a given mass following a fission event. Range of masses corresponding to isotopes of iodine shown in purple and isotopes of yttrium shown in green. | 12 |
| 1.6 | Illustration of the band gap in diamond as a function of interatomic spacing. Taken from [13]. | 14 |
| 1.7 | Electronic density of states for the different crystal structures of ZrO_2 showing the band gap predicted by DFT. | 15 |
| 2.1 | Binary phase diagram of the Zr and O_2 system. Taken from [14]. | 16 |
| 2.2 | A monoclinic zirconia unit cell indicating the two different oxygen bond coordinations. Small spheres represent oxygen ions while large spheres represent zirconium ions. Taken from [15]. | 17 |
| 2.3 | Zirconium centre in monoclinic ZrO_2 showing nearest oxygen atoms and their respective bond co-ordinations. Zirconium atoms are shown in green and oxygen atoms in red. | 17 |
| 2.4 | A) Tetragonal ZrO_2 viewed along the [110] direction. B) Cubic ZrO_2 viewed along the [100] direction. Zirconium atoms are shown in green and oxygen atoms in red. | 18 |
| 2.5 | Illustration of the OII cotunnite crystal structure of ZrO_2 . Zirconium and oxygen ions are shaded dark and light respectively. Taken from [16]. | 19 |

| | | |
|------|--|----|
| 2.6 | Pressure-temperature phase diagram for ZrO_2 . Dash-dotted lines represent more recent data. Diamonds mark transition points during an increase in pressure/temperature, while open circles are used for a decrease in pressure/temperature. Solid circles represent transition points for a fresh, single crystal sample. Taken from [17]. | 20 |
| 2.7 | Density plot of the nearest neighbour Zr-O bond distances in ZrO_2 for each crystal structure. Specific volumes from DFT simulations are $11.99 \text{ \AA}^3\text{ion}^{-1}$, $11.51 \text{ \AA}^3\text{ion}^{-1}$, and $11.13 \text{ \AA}^3\text{ion}^{-1}$ for monoclinic, tetragonal, and cubic phases respectively. | 21 |
| 3.1 | Illustration of an all-electron potential V_{AE} and a pseudopotential V_{PS} with their corresponding wave functions. r_{cut} indicates the radius beyond which both the potentials and their wave functions are the same. Taken from [18]. | 28 |
| 3.2 | Plots of the valence s and p orbital potentials for oxygen. Dashed lines indicate the all-electron potentials while solid lines indicate the corresponding pseudopotential. Dotted vertical line marks the radius beyond which the potentials match. | 29 |
| 3.3 | Plots of the valence s , p and d orbital potentials for zirconium. Dashed lines show the all-electron potentials while solid lines indicate the corresponding pseudopotential. Dotted vertical line marks the radius beyond which the potentials match. | 30 |
| 3.4 | Two dimensional illustration of periodic boundary around a primitive cell. | 32 |
| 3.5 | Tetragonal phase Brouwer diagrams of point defects at iodine concentrations of a) 10^{-5} and b) 10^{-3} , at a temperature of 1500 K. Space charge = 10^{-1} | 38 |
| 3.6 | Plot of the log error of DFT energy against plane-wave cut-off energy for a perfect cell of each crystal structure. The error is calculated with respect to a highly converged value, calculated at a plane-wave cut-off energy of 900 eV. The red arrow indicates the cut-off energy beyond which the error is below 2 decimal places. | 39 |
| 3.7 | Log of the error in the total energy of the system as a function of k-point spacing. The error is calculated relative to a highly converged energy value at a k-point spacing of 0.01 \AA^{-1} . The red arrow indicates the k-point spacing, which ensures an error below 2 decimal points for all structures. | 40 |
| 3.8 | Energy deviation in meV of supercells with candidate OTF pseudopotential pairs. Energy deviations are shown with respect to the pseudopotential pair that resulted in the lowest total energy calculated. | 42 |
| 3.9 | Energy minimisation of two iodine atoms from an initial separation of 3.0 \AA | 43 |
| 3.10 | Calculated band gaps for different +U values in monoclinic, tetragonal and cubic ZrO_2 | 44 |
| 3.11 | Individual lattice parameters as a function of +U term in monoclinic ZrO_2 | 45 |
| 3.12 | Individual lattice parameters as a function of +U term in tetragonal ZrO_2 | 45 |
| 3.13 | Individual lattice parameters as a function of +U term in cubic ZrO_2 | 46 |

| | | |
|-----|--|----|
| 4.1 | Zirconium centre showing nearest oxygen atoms in tetragonal ZrO_2 . Schottky trios indicated by oxygen enumeration. Zirconium atoms are shown in green and oxygen atoms in red. | 49 |
| 4.2 | Zirconium centre showing nearest oxygen atoms in cubic ZrO_2 . Schottky trios indicated by oxygen enumeration. Zirconium atoms are shown in green and oxygen atoms in red. | 50 |
| 5.1 | Helmholtz free energy as a function of temperature for the monoclinic, tetragonal, and cubic crystal structures of ZrO_2 | 60 |
| 5.2 | Monoclinic phase Brouwer diagram of intrinsic defects at 650 K. | 61 |
| 5.3 | Tetragonal phase Brouwer diagrams of intrinsic defects at 1500 K. | 62 |
| 5.4 | Cubic phase Brouwer diagrams of intrinsic defects at 2000 K. | 63 |
| 6.1 | Monoclinic phase Brouwer diagrams of point defects at iodine concentrations of a) 10^{-5} and b) 10^{-3} , at a temperature of 650 K. | 73 |
| 6.2 | Tetragonal phase Brouwer diagrams of point defects at iodine concentrations of a) 10^{-5} and b) 10^{-3} , at a temperature of 1500 K. | 73 |
| 7.1 | Plot of the percentage yield of nuclei with a given mass following a fission event. Range of masses corresponding to isotopes of Te, I, Xe and Cs are highlighted. Adapted from [19]. | 85 |
| 7.2 | Tetragonal phase Brouwer diagrams of point defects at tellurium concentrations of a) 10^{-5} and b) 10^{-3} , at a temperature of 1500 K. Space charge = 0 | 85 |
| 7.3 | Tetragonal phase Brouwer diagrams of point defects at iodine concentrations of a) 10^{-5} and b) 10^{-3} , at a temperature of 1500 K. | 86 |
| 7.4 | Tetragonal phase Brouwer diagrams of point defects at Xenon concentrations of a) 10^{-5} and b) 10^{-3} , at a temperature of 1500 K. Space charge = 0 | 86 |
| 7.5 | Tetragonal phase Brouwer diagrams of point defects at caesium concentrations of a) 10^{-5} and b) 10^{-3} , at a temperature of 1500 K. Space charge = 0 | 87 |
| 7.6 | Tetragonal phase Brouwer diagrams of point defects at Tellurium concentrations of a) 10^{-5} and b) 10^{-3} , at a temperature of 1500 K. Space charge = 0 | 94 |
| 7.7 | Tetragonal phase Brouwer diagrams of point defects at Xenon concentrations of a) 10^{-5} and b) 10^{-3} , at a temperature of 1500 K. Space charge = 0 | 96 |
| 7.8 | Tetragonal phase Brouwer diagrams of point defects at caesium concentrations of a) 10^{-5} and b) 10^{-3} , at a temperature of 1500 K. Space charge = 0 | 98 |

Chapter 1

Introduction

1.1 Nuclear Power

In the summer of 1956, the world's first commercial nuclear power plant was connected to the grid in the north of England. This marked a significant departure from previous forms of commercial energy production, which relied on less energetically lucrative sources such as combustion of coal, oil and gas. Indeed, the closest we had come to utilising nuclear energy commercially was through geothermal power, where the thermal energy is partly due to radiogenic heat from unstable isotopes in the Earth's mantle [17]. Combustion is a chemical process where energy differences between reactants and products are exploited via electron exchange. Nuclear energy however, exploits the energy difference between nuclei. Both rely on the conversion of mass into energy, however, the amount of energy that can be extracted from the nucleus is several orders of magnitude greater.

Consider methane, with an enthalpy of combustion of -887.2 kJ/mol [20]. This is the equivalent of 9.14 eV per particle. By comparison, the energy release from fission of one uranium-235 nucleus is at least 1.65×10^8 eV, as shown in Figure 1.1.

Combustion-based power as a technology has matured over hundreds of years, with modern optimisations only looking to offer fractional percent gains in efficiency. By comparison, nuclear

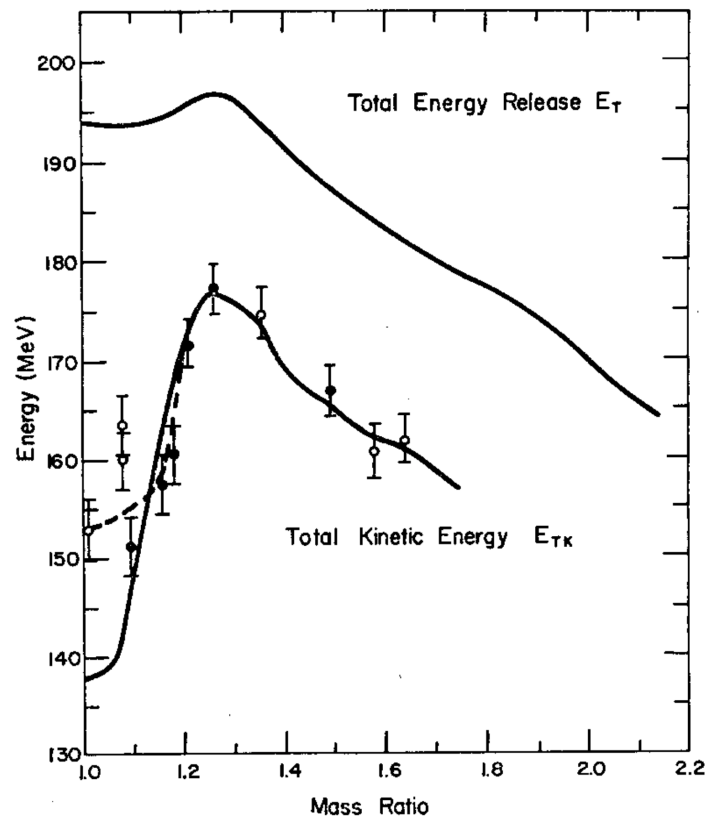


Figure 1.1: Energy from thermal fission of U-235 as a function of mass ratios of child nuclei. Total energy release includes contributions from gamma rays and subsequent radioactive decays. Taken from [6].

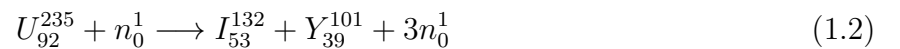
power technology is far from mature, with large improvements yet to be realised. One such feature is load-following, an enormously useful feature for a power plant which is currently unavailable in nuclear reactors. The biggest hurdle to achieving load-following in nuclear reactors is the issue of pellet-cladding interaction (PCI), which is the basis of the work in this thesis.

1.1.1 Fission

Commercial nuclear power plants extract energy through the process of fission, where a large nucleus is split into smaller nuclei. While it is also possible to extract energy from certain nuclei by the process of fusing them into larger ones, no fusion reactor currently exists which achieves a net positive energy output. At a fundamental level, both of these processes rely upon mass-energy equivalence. The relationship between mass and energy is shown using Einstein's famous equation:

$$E = mc^2 \quad (1.1)$$

where E is the energy of the system, m is the mass and c is the speed of light. Using this equation we can analyse a typical fission reaction:



While the number of protons and neutrons are conserved throughout the reaction, a quick calculation will show that there is actually less mass in the products than the reactants by approximately 0.188 amu (3.127×10^{-28} kg). This missing mass, known as the *mass defect*, is converted to energy (~ 175 MeV). In this way, the total mass-energy of the system is conserved.

This change in mass arises due to the phenomenon of *binding energy*. In order for two or more nucleons to be thermodynamically stable when bound together, the total free energy of the bound configuration must be less than the sum of constituent nucleon free energies. Much like

with energy stored in a chemical bond, the binding energy represents the energy required to separate the nucleus into individual protons and neutrons.

Larger nuclei will generally have a greater total binding energy value compared to smaller nuclei, but the mass defect per nucleon will not necessarily be greater in a larger nucleus. It is therefore useful to normalise the binding energy by the mass number. Different isotopes have different binding energies, and any nuclear reaction which increases the binding energy per nucleon will be exothermic, whether by fission or fusion. Figure 1.3 shows a plot of binding energy per nucleon against mass number with the relevant isotopes from Equation 1.2.

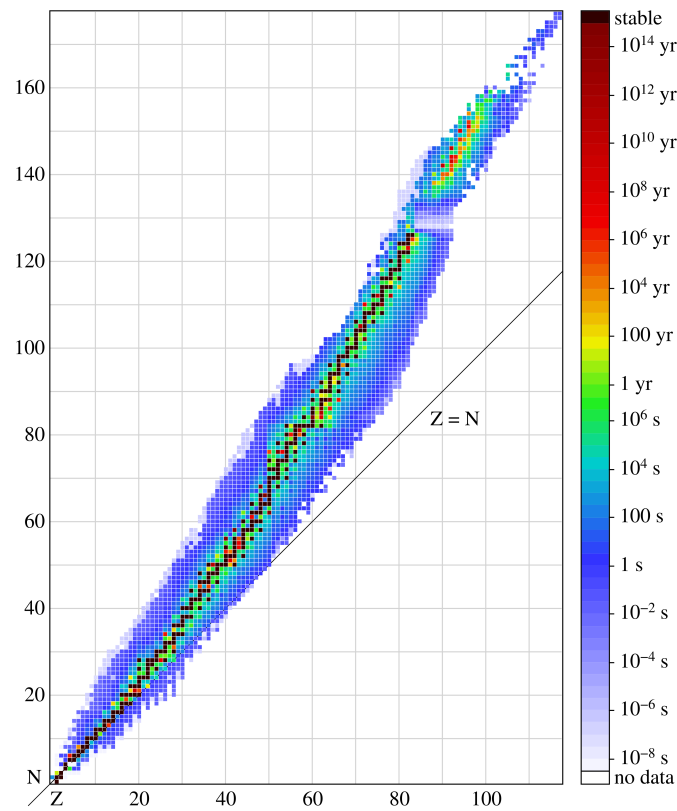


Figure 1.2: Plot of neutron number against proton number for nuclei with half-lives greater than 10^{-4} s. Half-life of the dominant decay mode is shown. Taken from [7].

1.1.2 Reactor design

Commercial nuclear reactors are large boilers in a Rankine cycle, designed to maximise heat transfer to a working fluid. All nuclear plants use steam turbines on the generation side, though the reactor coolant may be another fluid in a separate loop, such as carbon dioxide in gas-cooled

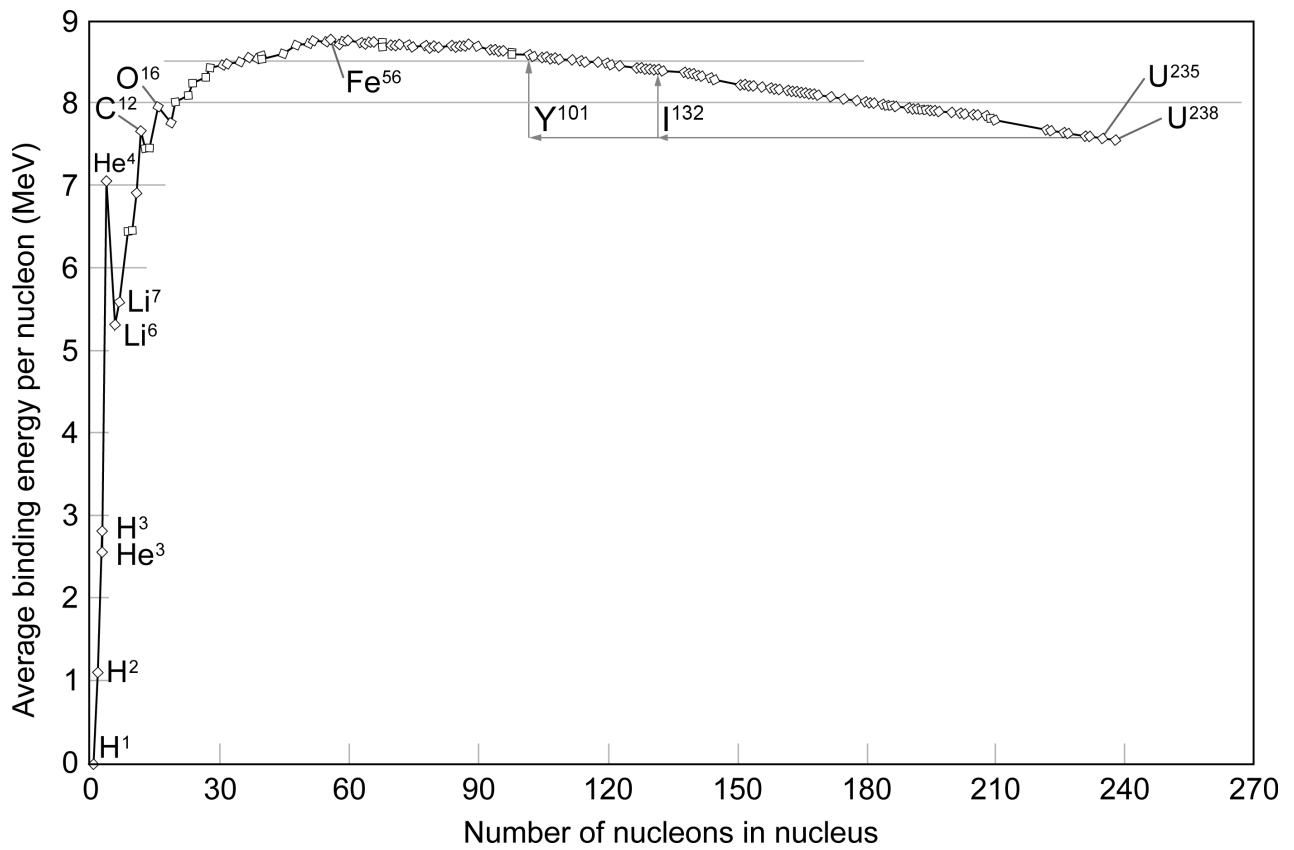


Figure 1.3: Plot binding energy per nucleon against mass number. Arrows indicate the reaction shown in equation 1.2. Adapted from [8].

reactors (GCRs), or even in a separate water loop such as in pressurised water reactors (PWRs) and CANDU. The work in this thesis is focused on zirconium-based claddings which are used worldwide in all commercial reactors except GCRs and sodium-cooled fast reactors. The most prevalent reactor type is the PWR, followed by the boiling water reactor (BWR) REFER TO TABLE.

- LWRs vs other kinds of reactors
- Zirconium cladding used because of strength + low thermal neutron abs cross section
- Thermal energy transferred from fuel to coolant
- RPV is pressurised to 150 bar in PWRs, less in BWRs and even less in CANDU

1.1.3 Nuclear reactor fuel pins

Fuel assemblies in nuclear reactors are bundles of fuel pins. In most commercial reactors, these fuel pins are comprised of a zirconium-based cladding which is filled with UO_2 fuel pellets, each of which are approximately 1 cm^3 in volume. Once loaded with fuel pellets, the fuel pins are capped and filled with inert helium gas, pressurised to between 2 and 25 atm to improve heat transfer from the fuel pellets to the coolant as well as delaying inward creep deformation of the cladding due to the high coolant pressure [21]. In the early stages of a fuel pin's life, there is a small gap between the fuel pellet and the cladding, known as the pellet-cladding gas gap. This gas gap slowly closes with increasing burn-up mostly due to swelling of the fuel pellets.

Zirconium cladding

- Zirconium cladding
- Ceramic fuel pellets
- Pellet-cladding gas gap
- Cladding failure (great review here [22])

1.1.4 Effects of radiation on materials

While ionising radiation is always present in the environment as background radiation, the intensity of radiation in a nuclear reactor is so great that it presents significant engineering challenges because of how it affects different materials.

Radiation hardening (also known as radiation embrittlement) is a phenomenon which affects most materials subjected to ionising radiation. It is characterised by a loss of plasticity caused by radiation damage over time, leading to an increased risk of cracks and failure of components. While zirconium is a very useful nuclear material due to its neutron transparency, it is still susceptible to this type of damage [23]. Beyond certain levels of radiation damage, phase changes may also occur. In ZrO_2 however,

Amorphisation is another effect of radiation damage. This is characterised by a loss of long-range order of atoms in a crystal. This typically occurs beyond a certain threshold of radiation damage depending on the material, called the critical amorphisation dose. Amorphisation is problematic because the loss of a defined crystal structure results in both a reduction in structural stability (amorphous materials have a higher Gibbs free energy than their crystalline counterparts) and causes swelling of the material [24]. In the literature, there is evidence of amorphisation in cubic stabilised ZrO_2 when bombarded with Cs^+ ions up to a fluence of 1×10^{21} ions m^{-2} [25]. However, no amorphisation is seen at an Xe^{2+} fluence of 2×10^{21} ions m^{-2} , or an I^+ fluence of 5×10^{19} ions m^{-2} [26].

One material phenomenon exclusive to nuclear reactor environments is neutron activation. The high free neutron environment leads to neutron capture in various nuclei within the reactor, including those of the fuel assemblies, coolant and RPV. There are many possible (n,x) reactions that may occur in materials experiencing a neutron flux, but of particular concern is transmutation of nuclei following a nuclear capture event. When a stable nucleus captures a neutron and becomes unstable, the nucleus may then emit particles to reduce its free energy, altering its atomic number in the process. This new element will have different chemical properties compared to the parent nucleus by virtue of a different electronic structure. This will change

the elemental composition of a material, typically in an unfavourable way with dopants that negatively affect some desired material property. The extremely large number of nuclei relative to neutron flux means that this effect is small, though over time this becomes more significant due to accumulation of these dopant elements.

- Radiolysis

1.1.5 Fission products, their distribution and decay chains

- Bi-modal distribution of fission products due to binding energy gains (get a good binding energy per nucleon plot)
- Fission products are almost always neutron-rich and will decay by beta-
- Iodine is always paired with yttrium (53+39 protons). Yttrium happens to be a very good cubic phase stabiliser in ZrO_2 and decays into Zr.
- Iodine appears both from direct fission, and from decay of tellurium which is also a common fission product.
- The decay chain we are interested in is $\text{Te} \rightarrow \text{I} \rightarrow \text{Xe} \rightarrow \text{Cs}$

1.2 Pellet-cladding interaction (PCI)

PCI has been known about since 1974. Many studies and reviews have been made [22]

1.2.1 Effect of power ramps

B.Cox PCI failures of Zr alloy fuel cladding [27] talks about how they found out that fission products were necessary for PCI failures on page 260 (citation 54)

1.2.2 Pellet-clad gap and bonding

- At the beginning of life, there is a gas gap between the fuel pellet and the cladding, typically filled with an inert gas like helium during the manufacturing process.
- With increasing burnup, radiation damage in the fuel pellet causes it to swell and therefore reduce the pellet-cladding gap, eventually making contact (and exerting a force) with the cladding.

1.2.3 Iodine corrosion of zirconium

1.3 Oxidation of zirconium

The oxidation of zirconium to produce ZrO_2 occurs during manufacture of the fuel clad when the metal is exposed to oxygen in air. ZrO_2 is a ceramic with material properties that make it desirable in many industrial applications, including solid-oxide fuel cells [28], refractory linings [29], and nuclear waste storage [30].

1.3.1 Oxygen solubility of zirconium

- Oxygen is soluble in zirconium up to 29% molar mass at "insert temperature".
- Several PCI studies have assumed a mechanism whereby the ZrO_2 layer is fractured, allowing iodine to attack fresh metal surface, but these studies always assume that the exposed metal is oxygen-depleted.
- It is not oxygen depleted, therefore they will always overestimate the amount of oxygen necessary to form a new passive oxide layer.

1.3.2 Oxide growth mechanism

An oxide layer will typically form on the surface of zirconium metal even at very low oxygen partial pressures [31]. The oxidation process is mainly driven by the ingress of oxygen ions. Initially, the oxide is highly protective, growing slowly into the metal until it reaches a thickness of approximately 2-3 μm [32, 33], after which the oxide growth mechanism enters a ‘post-transition’ stage where the oxidation kinetics follow a cubic-rate law [34].

1.3.3 Outer oxide vs inner oxide

The fuel cladding of an LWR develops an oxide on both the inner and outer surfaces due to exposure to oxygen in air during manufacture.

1.3.4 Sources of oxygen

The internal oxide layer is present before fuel claddings are pressurised with helium gas and sealed. This is from the normal oxidation of Zr in air, where the oxygen pressure is 0.21 atm. After capping of the fuel rods, the only other available oxygen is from the UO_2 fuel pellets.

Uranium oxides have a wide range of non-stoichiometric compositions, with U/O ratios ranging from 1.67 to 2.24 in solid $\text{UO}_{2\pm x}$, as shown in Figure 1.4. The oxide form U_3O_{8-y} also exists and is more kinetically and thermodynamically stable than UO_2 , but has lower density, making it less suitable for use as a fuel form. The different stoichiometries have different equilibrium O_2 pressures at constant temperature (REF TABLE), allowing some level of tweaking the internal cladding environment depending on whether more or less oxygen is desired.

Oxygen and oxygen precursors may also be produced directly from fission of U_{235} , but this contribution is insignificant compared to changing the stoichiometry of the fuel pellet. Indeed, liberation of oxygen from $\text{UO}_{2\pm x}$ due to fission (which is also a function of the fuel’s stoichiometry) is a more significant contributor to the oxygen pressure than direct production via fission.

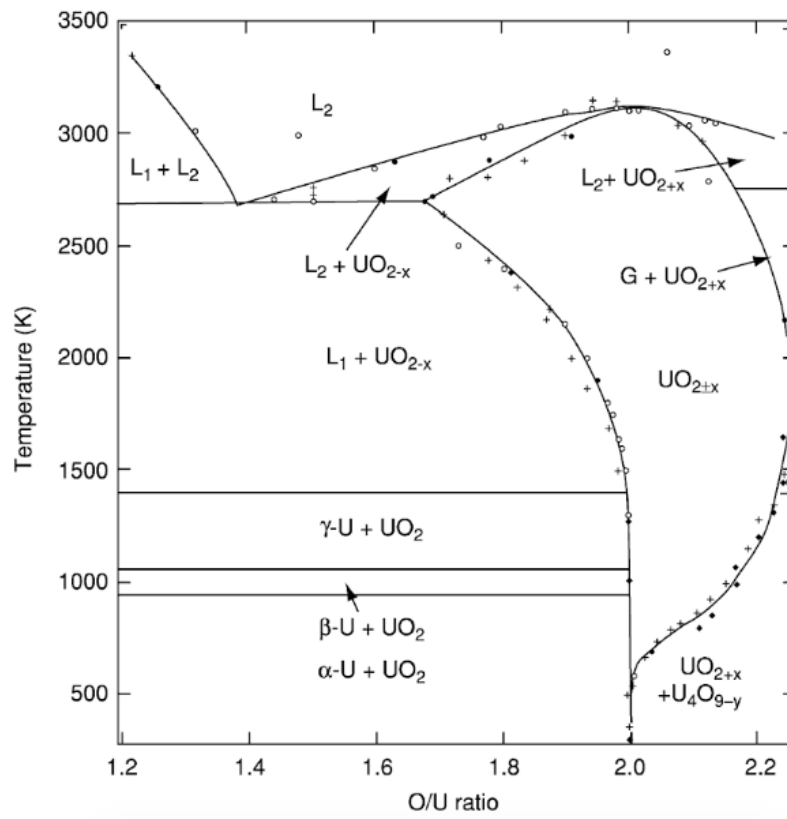


Figure 1.4: Partial U-O temperature phase diagram between O/U ratios of 1.2 and 2.25. Figure taken from [9], with phase boundaries from [10–12].

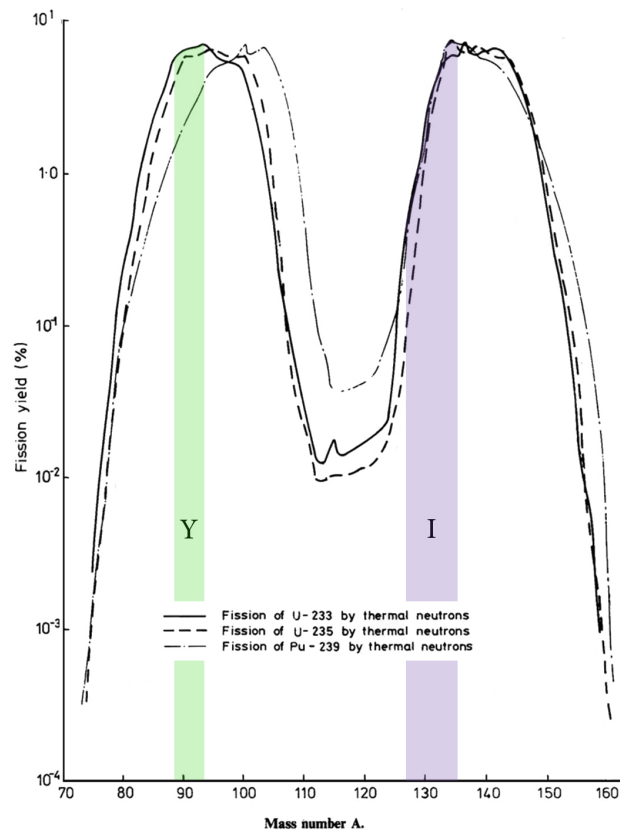


Figure 1.5: Plot of the percentage yield of nuclei with a given mass following a fission event. Range of masses corresponding to isotopes of iodine shown in purple and isotopes of yttrium shown in green.

1.4 Atomistic Simulation

1.4.1 Classical approach - molecular dynamics

- Molecular dynamics allows for large system sizes (millions of atoms) compared to DFT because of the low computational cost of classical potentials.
- These are mainly pair potentials (although many-bodied potentials are also used) which are some combination of a short-range repulsion term (Pauli exclusion, nuclear repulsion if van der waals is taken into account) and a long range Coulombic attraction term

1.4.2 Quantum mechanical approach - DFT

- Up to hundreds of atoms, but far more fundamental data such as electron density.
- Very computationally expensive, but with clever workarounds for bulk crystallographic systems.

1.4.3 Band gap

Materials are sometimes considered to fall into one of two categories; conductors or insulators. While this binary characterisation may work as an approximation for many materials, in reality there is more of a continuum between these two states, and at the heart of this lies the band gap.

It is known that for ions, electron energy levels are quantised, restricting the range of possible electron energies to discrete quantities. More specifically, electrons can only occupy unique quantum states, defined by parameters such as quantum spin and angular momentum. In a crystal, where there are large numbers of electrons and many possible configurations of them, we refer to energy "bands" which are comprised of many quantised energies. There are sometimes gaps between energy bands in crystals corresponding to energy levels that cannot be occupied, meaning that if electrons were to be added at the lowest energy levels one by one, there would

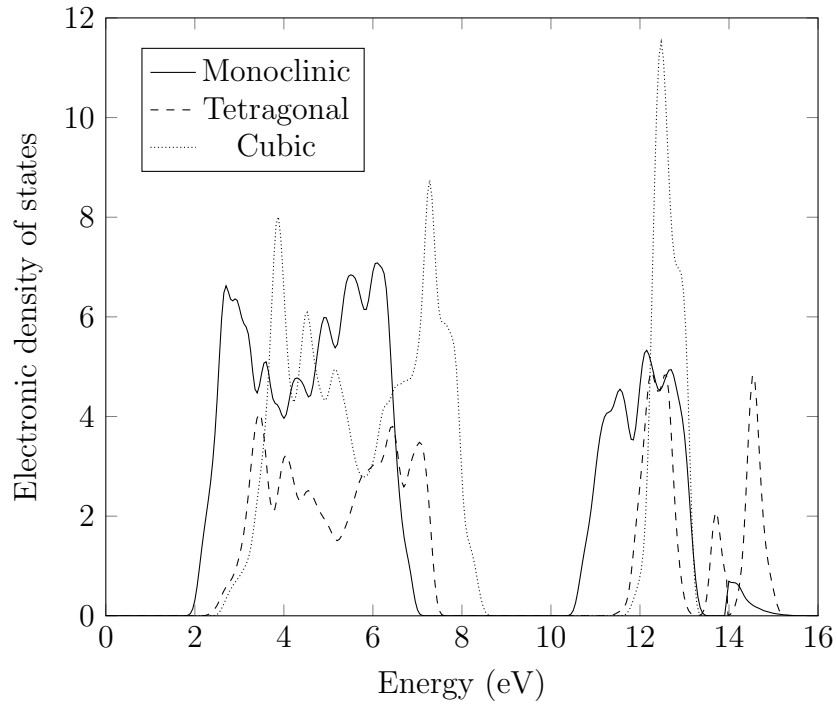


Figure 1.7: Electronic density of states for the different crystal structures of ZrO_2 showing the band gap predicted by DFT.

<http://hyperphysics.phy-astr.gsu.edu/hbase/Solids/band.html>

- Non-metals exhibit an energy gap between valence and conduction electron bands, demarcating insulators and conductors.

Table 1.1: Experimentally determined band gaps alongside values calculated from DFT simulations for each crystal structure of zirconia. Experimental values taken from [1].

| Crystal Structure | Band gap (eV) | |
|-------------------|---------------|------|
| | Expt. | DFT |
| Monoclinic | 5.83 | 3.45 |
| Tetragonal | 5.78 | 4.00 |
| Cubic | 6.10 | 3.55 |

Chapter 2

Crystallography and Point Defects

2.1 ZrO_2 phases and stabilisation

ZrO_2 is unusual in exhibiting three commonly reported polytypes in its binary phase diagram (Figure 2.1). Each will now be described and contrasted.

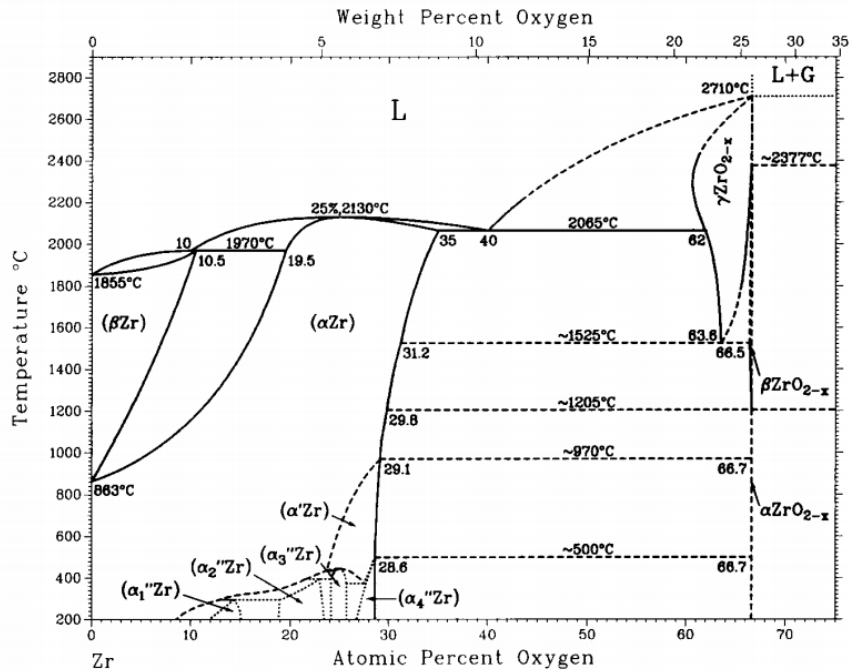


Figure 2.1: Binary phase diagram of the Zr and O₂ system. Taken from [14].

2.1.1 Monoclinic

A unit cell of monoclinic ZrO_2 is illustrated in Figure 2.2. The dashed line (approximately 3.7\AA in length) shows the Zr-O bond which is broken when transitioning to monoclinic from the tetragonal phase.

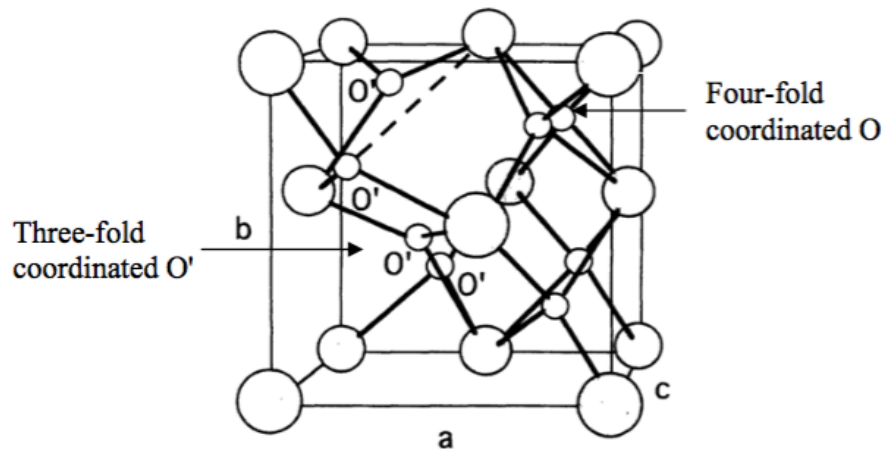


Figure 2.2: A monoclinic zirconia unit cell indicating the two different oxygen bond coordinations. Small spheres represent oxygen ions while large spheres represent zirconium ions. Taken from [15].

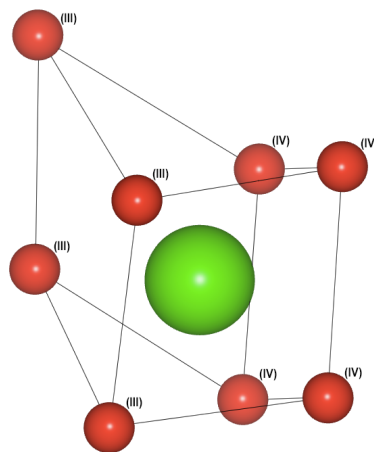


Figure 2.3: Zirconium centre in monoclinic ZrO_2 showing nearest oxygen atoms and their respective bond co-ordinations. Zirconium atoms are shown in green and oxygen atoms in red.

Table 2.1: ZrO_2 crystal structures and their stable temperatures at 1 atm [2].

| Crystal Structure | Space Group | Temperature Range (K) |
|-------------------|--------------|-----------------------|
| Monoclinic | $P2_1/c$ | $T < 1440$ |
| Tetragonal | $P4_2/nmc$ | $1440 < T < 2640$ |
| Cubic | $Fm\bar{3}m$ | $2640 < T < 2950$ |

2.1.2 Tetragonal

2.1.3 Cubic

Cubic phase stability

- The existence of a cubic phase in undoped ZrO_2 is debated. The high temperatures required for stabilisation of the cubic phase and the similarity to the tetragonal phase make it difficult to discern as a third phase.
- Also due to the high temperature, the stability of the cubic phase in DFT calculations may be inaccurate. This is discussed further in Chapter 3.

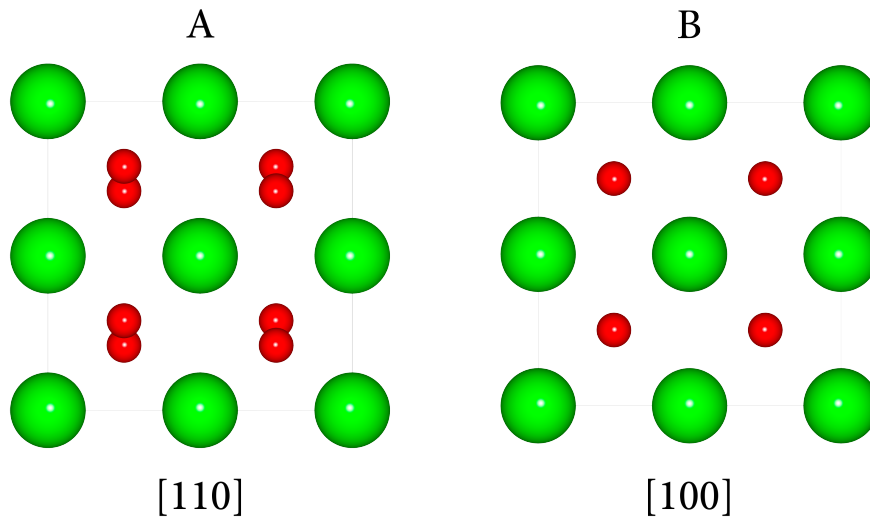


Figure 2.4: **A)** Tetragonal ZrO_2 viewed along the $[110]$ direction. **B)** Cubic ZrO_2 viewed along the $[100]$ direction. Zirconium atoms are shown in green and oxygen atoms in red.

2.1.4 Other phases

Cotunnite

Two orthorhombic phases of ZrO_2 have also been observed at high pressures.

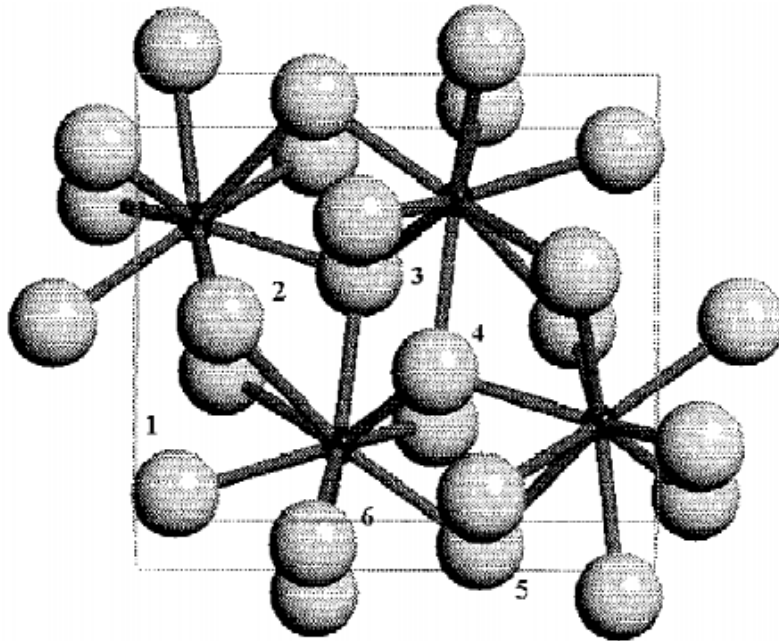


Figure 2.5: Illustration of the OII cotunnite crystal structure of ZrO_2 . Zirconium and oxygen ions are shaded dark and light respectively. Taken from [16].

Volume expansion

The phase transitions in ZrO_2 are accompanied by a change in volume, where the monoclinic phase is the least dense and the cubic phase is the most dense (see Figure 2.7). This is especially significant in the case of the martensitic t- ZrO_2 to m- ZrO_2 transition, where the volume increases by around 9% [35]. This has substantial implications for the creation and opening of cracks as ZrO_2 is a ceramic material with low toughness. This is especially relevant in a reactor scenario where temperature cycling (shutdown/startup or load-following behaviour) may lead to fatigue if the phase transition threshold is passed.

Another consequence of this large volume expansion is that a significant hysteresis effect is observed in the monoclinic/tetragonal phase transition, as shown in Figure 2.6.

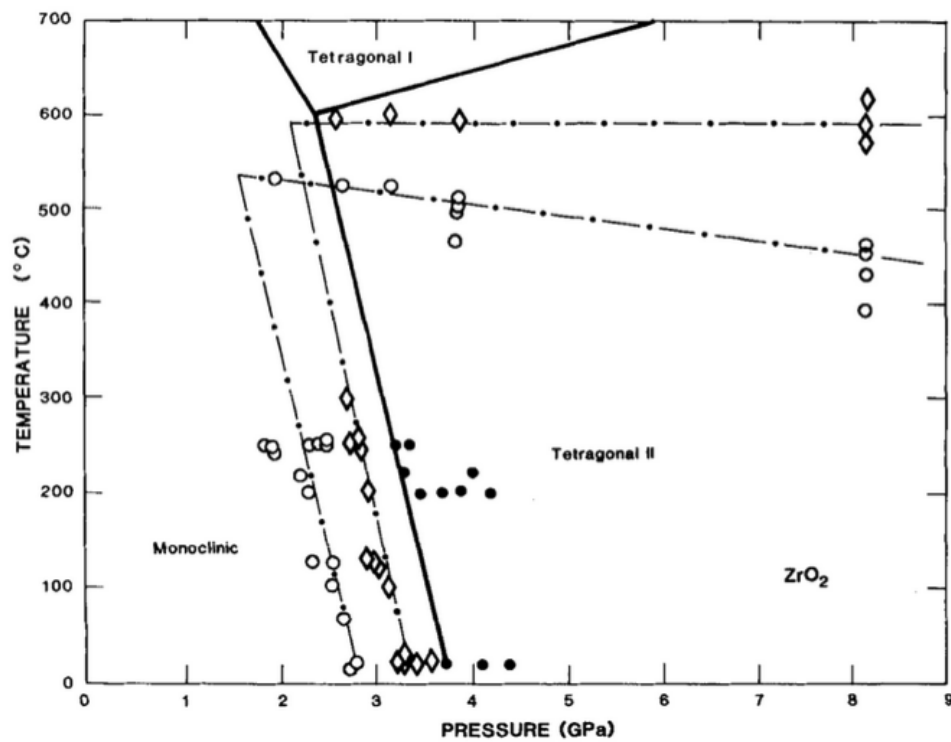


Figure 2.6: Pressure-temperature phase diagram for ZrO_2 . Dash-dotted lines represent more recent data. Diamonds mark transition points during an increase in pressure/temperature, while open circles are used for a decrease in pressure/temperature. Solid circles represent transition points for a fresh, single crystal sample. Taken from [17].

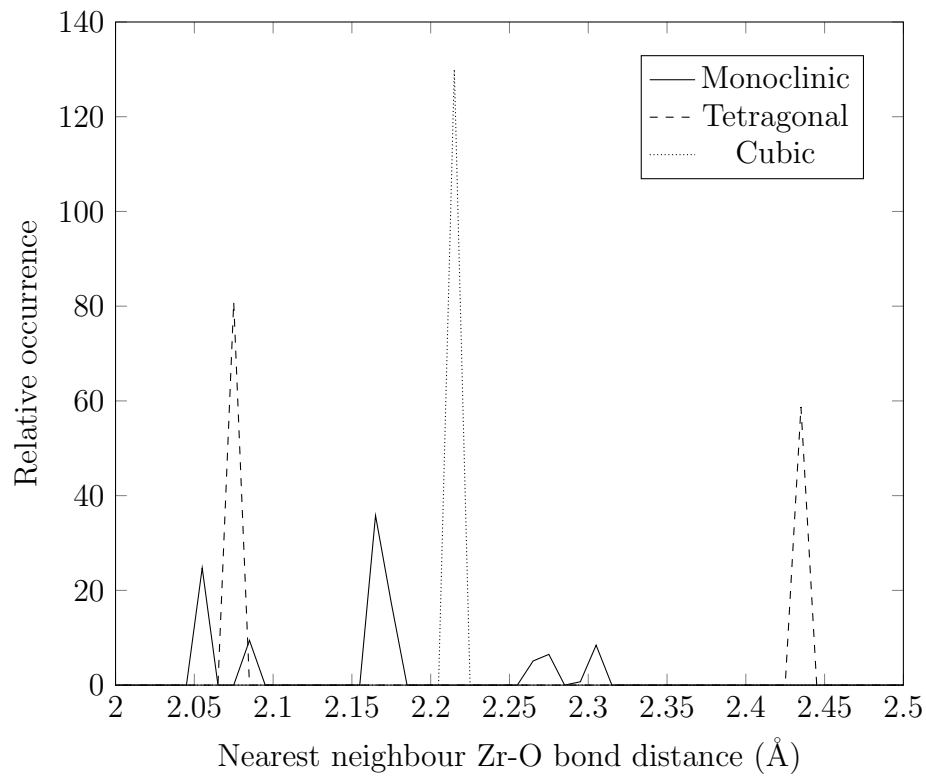


Figure 2.7: Density plot of the nearest neighbour Zr-O bond distances in ZrO_2 for each crystal structure. Specific volumes from DFT simulations are $11.99 \text{ \AA}^3\text{ion}^{-1}$, $11.51 \text{ \AA}^3\text{ion}^{-1}$, and $11.13 \text{ \AA}^3\text{ion}^{-1}$ for monoclinic, tetragonal, and cubic phases respectively.

2.1.5 Pressure stabilisation (isochoric + autostabilisation)

The tetragonal and cubic phases of ZrO_2 are stabilised at high pressure. Since the oxide has a larger volume than the underlying metal (pilling-bedworth ratio of 1.5X), the growth of the oxide will itself impose stresses which may stabilise the tetragonal phase.

2.1.6 Dopant stabilisation (lower valence cations)

Particular kinds of dopants will also stabilise the tetragonal and cubic phases of ZrO_2 . The most technologically significant of which is yttrium, which at concentrations of 15% (atomic), fully stabilises the cubic phase. Zirconia stabilised this way is known as yttria-stabilised zirconia (YSZ). This works by trivalent yttrium promoting the inclusion of charge compensating oxygen vacancy defects (see Equation 2.1). This works in a similar way with several other cation dopants such as trivalent scandium from Sc_2O_3 , or divalent magnesium from MgO (Equation 2.2).



While ZrO_2 would ideally adopt the regular cubic fluorite structure, we only observe cubic stabilisation at elevated temperatures where the ionic radii of the zirconium ion increases (and possibly a stabilising phonon mode contribution). Yttrium is known to stabilise the cubic phase in ZrO_2 at standard conditions. This stabilising effect is observed because the yttrium ion is of the appropriate size to maintain the oxygen ions and vacancies in the VIII coordination at low temperatures, as can be seen from ionic radii values in Table 2.2.

Table 2.2: Ionic radii of Zr^{4+} and Y^{3+} in various coordination environments. Values taken from [3].

| Ion | Coordination | Ionic Radius (\AA) |
|------------------|--------------|-------------------------------|
| Zr^{4+} | IV | 0.59 |
| | V | 0.66 |
| | VI | 0.72 |
| | VII | 0.78 |
| | VIII | 0.84 |
| | IX | 0.89 |
| Y^{3+} | VI | 0.90 |
| | VII | 0.96 |
| | VIII | 1.019 |
| | IX | 1.075 |

2.1.7 Kröger-Vink notation

Kröger-Vink notation [36] is used throughout this thesis to describe defects. It is widely used in physical chemistry and is a useful shorthand for describing chemical reactions where conservation of mass, charge and lattice sites is required. The notation syntax is of the form x_z^y , where x is the substituted atom or missing atom (i.e. a vacancy V), y is the charge of the defect (relative to the lattice species that originally occupied the site) and z is the site the defect occupies. Positive and negative charges are indicated with dots (\bullet) and dashes ($'$) respectively, otherwise a cross (\times) is used to denote a neutral defect. The site may be either a lattice site (such as Zr or O in ZrO_2) or an interstitial site (i). Table 2.3 shows examples of several different types of defects and their respective Kröger-Vink notation.

Table 2.3: Examples of Kröger-Vink notation for several defects in ZrO_2 .

| Defect | Kröger-Vink Notation |
|---|--|
| Anion vacancy | $V_{\text{O}}^{\bullet\bullet}$ |
| Cation vacancy | $V_{\text{Zr}}^{\prime\prime\prime\prime}$ |
| Anion interstitial | $O_i^{\prime\prime}$ |
| Cation interstitial | $Zr_i^{\bullet\bullet\bullet\bullet}$ |
| Iodine (I^- anion) on oxygen site | I_{O}^{\bullet} |

Chapter 3

Computational Methodology

3.1 Density functional theory

Quantum mechanics is the most complete modern theory which describes the behaviour of matter at the energy scale of atoms. It can be used to predict things such as the energy levels of atoms, the interactions of light with matter accurately, and the thermodynamic stability of systems of atoms. Ideally, the mathematical formalisms of quantum mechanics would be used to predict the properties and behaviour of all possible types of molecules and materials. In reality, this is very difficult to achieve, requiring several approximations and abstractions in order to produce a method which, in the end, sacrifices physical accuracy in order to be computationally tractable. The most successful field of study in this domain for most solids is that of density functional theory.

3.1.1 The Schrödinger equation

$$E\Psi(\mathbf{r}) = \hat{H}\Psi(\mathbf{r}) \tag{3.1}$$

Where E is the total energy of the system, Ψ is the wave function, and \hat{H} is the energy Hamiltonian operator which includes the kinetic energy contributions (\hat{T}) and potential energy

contributions (\hat{V}), shown in atomic units in equations 3.3 and 3.4 respectively:

$$\hat{H} = \hat{T} + \hat{V} \quad (3.2)$$

$$\hat{T} = -\sum_i \frac{1}{2} \nabla_{r_i}^2 - \sum_i \frac{1}{2M_i} \nabla_{R_i}^2 \quad (3.3)$$

$$\hat{V} = \sum_{i,j=i+1} \frac{1}{2|r_i - r_j|} + \sum_{i,j=i+1} \frac{Z_i Z_j}{2|R_i - R_j|} - \sum_{i,j} \frac{Z_i}{2|R_i - r_j|} \quad (3.4)$$

where r_i is the position of electron i , R_i is the position of nucleus i and M_i is the mass of nucleus i . Thus, the second term on the right of equation 3.3 relates to the kinetic energy of any associated nuclei, and the first term to electrons.

3.1.2 Kohn-Sham Method

Density Functional Theory (DFT) was developed by Kohn and Sham in 1964 [37] as an ab initio method for solving the wave equation. The Kohn-Sham Hamiltonian (Equation 3.5) is used in the Schrödinger equation.

$$\hat{H}(\rho(\mathbf{r})) = E_{KE}(\rho(\mathbf{r})) + E_P(\rho(\mathbf{r})) + E_{XC}(\rho(\mathbf{r})) \quad (3.5)$$

Where E_{KE} and E_P are the kinetic and potential energy functionals (functions of functions), ρ is the electron density, E_{XC} is the exchange correlation functional, and \mathbf{r} is the position vector. The main approximation is to consider that the electrons only interact with nuclei and the average field generated by all other electrons, and not other electrons explicitly, thus allowing all the terms to be evaluated using the electron density rather than position. An exchange correlation term is then used to include the non-classical electron-electron interactions, namely electron exchange and correlation. Additionally, the exchange correlation term also includes the difference in kinetic energy found due to the use of non-interacting electrons. While Kohn and Sham did provide a proof for the existence of an exchange correlation function, a general form

of the functional has not yet been found, although several forms have been considered, each with their own strengths and weaknesses when applied to different systems. One basic form of the functional which is frequently used is the local density approximation (LDA) CITATION XXX:

$$E_{LDA}(\rho(r)) = [\textit{integral}] \rho(r) E_{uniform}(\rho(r)) dr \quad (3.6)$$

where $\rho(r)$ is the electron density at location r , and $E_{uniform}$ is the exchange-correlation energy of a uniform electron gas (an idealised system). This exchange-correlation functional generates accurate results in materials such as metals where the electron density is relatively uniform, while systems with more variable electron densities (e.g. highly ionic materials) require more complex functionals. A natural extension of the LDA is to also take into account the gradient of the electron density, thus allowing a smoother functional fit when electron density is highly variable with position. Such functionals are collectively referred to as generalised gradient approximations (GGAs). One GGA which has enjoyed widespread use for many different types of systems is the Perdew-Burke-Ernzerhof (PBE) GGA. The accuracy of this functional when modelling solid phase systems is well-established, and its frequent use in DFT studies provides ample reference material for comparing results. After conducting several convergence tests (see 3.5), the PBE GGA was chosen as the exchange-correlation functional to be used for all calculations in this work.

Born-Oppenheimer approximation

The Born-Oppenheimer approximation is a two-step process for evaluating atomic forces, which greatly reduces the computational costs of any atomistic simulation. It exploits the large difference in mass between nuclei and electrons in order to separate their interactions. This allows us to decompose the total wave function into a product of an electronic wave function and a nuclear wave function via a separation of variables approach. The first step involves ignoring the kinetic energy contribution of nuclei by assuming they are stationary, thus we

can remove the nuclear kinetic energy term in Equation 3.3. The stationary nuclei assumption also simplifies the nuclear-nuclear Coulombic repulsion term in Equation 3.4 because $|R_i - R_j|$ becomes a constant throughout the calculation. An electronic Schrödinger equation is then solved where electronic positions are variables and nuclear positions are fixed parameters. This solution contains information of the shape of the electronic orbitals. The next step is to take the electronic distribution and calculate the resultant forces on the nuclei. The nuclear positions are then modified to try to minimise these forces, followed by feeding these nuclear positions back into the electronic Schrödinger equation to obtain the new electronic distribution. This process is repeated until the required convergence criterion (energy change per iteration, forces on nuclei) are satisfied.

3.1.3 Pseudopotentials

The electron-electron interaction component of the potential energy presents a problem when it comes to scaling experimental models. The number of terms in this interaction grows quadratically with the number of electrons in the system, and quickly becomes computationally intractable for even small systems. However, we know that in chemical reactions, the majority of chemical behaviour is determined by relatively few valence electrons, while the more numerous core electrons have a far smaller effect. Consider the zirconium atom with 40 electrons, of which 4 ($4d^25s^2$) are typically involved in bonding and chemical reactions. By only considering only these valence electrons for Coulombic-term calculations, we reduce the system size by 90% which provides much more than a tenfold reduction in computational requirements. Although the core electrons do not participate in chemical reactions, they still influence the properties of the atom, such as the atomic radius. Instead of modelling the core electrons explicitly, we can approximate their aggregate effect with a potential energy function. This is what we aim to achieve by using the pseudopotential method. An example pseudopotential is shown in figure 3.1.3.

Figures 3.1.3 and 3.1.3 show the actual pseudopotentials used throughout this work for oxygen and zirconium respectively. The potentials are shown broken down by the electronic sub-shells

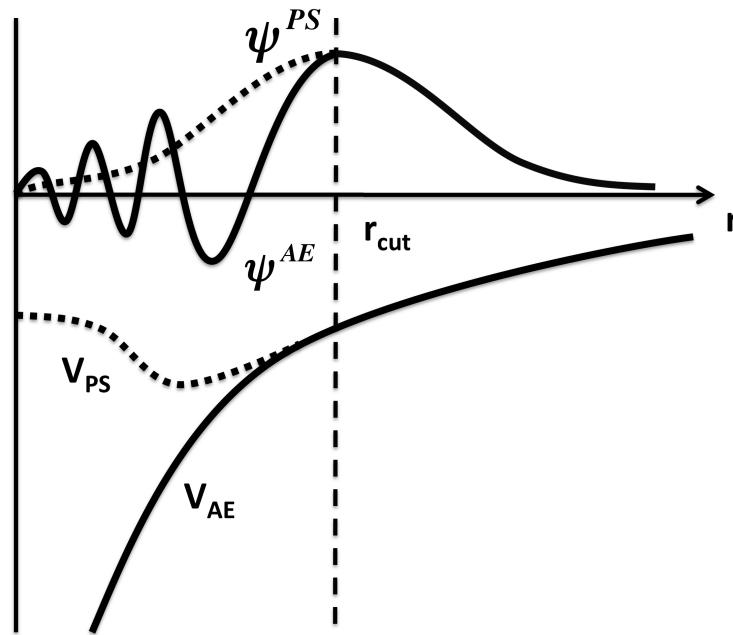


Figure 3.1: Illustration of an all-electron potential V_{AE} and a pseudopotential V_{PS} with their corresponding wave functions. r_{cut} indicates the radius beyond which both the potentials and their wave functions are the same. Taken from [18].

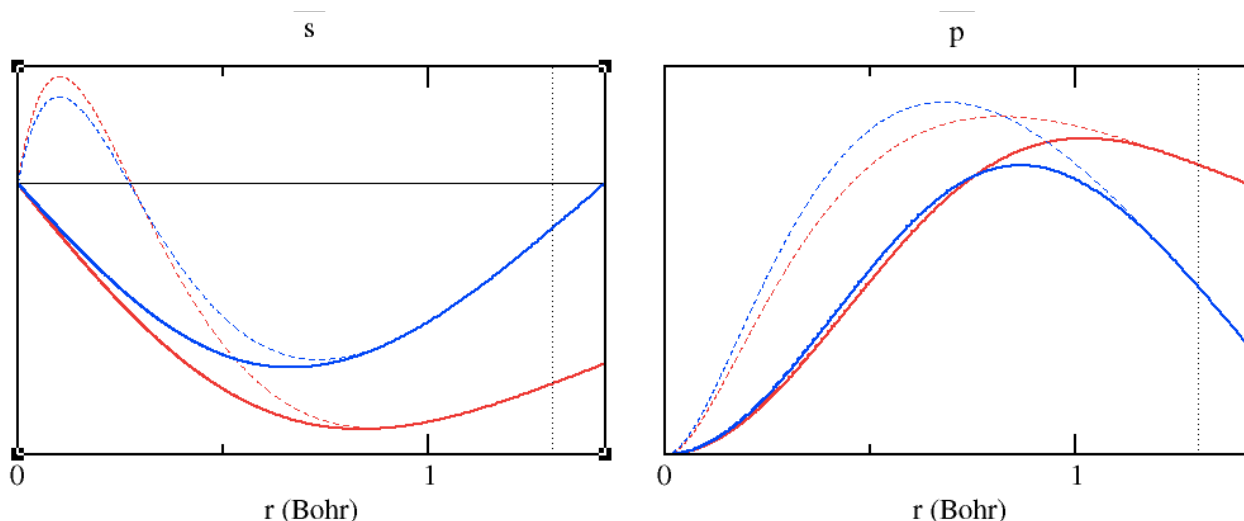


Figure 3.2: Plots of the valence s and p orbital potentials for oxygen. Dashed lines indicate the all-electron potentials while solid lines indicate the corresponding pseudopotential. Dotted vertical line marks the radius beyond which the potentials match.

occupied by the valence electrons.

3.2 Periodic boundaries

3.2.1 Bloch's theorem

The repeating nature of a crystal structure, defined by the lattice vectors plus a basis set of atoms that are repeated, is well-suited for computer models. It allows us to define periodicity in three dimensions for a given unit cell. An example of this periodicity is illustrated in Figure 3.2.2 in two dimensions. Utilising this periodicity is theoretically justified as follows:

- Nuclei are arranged in a periodically repeating pattern, thus their potentials acting on electrons are also periodic.
- If the potential is periodic, it follows that the electron density is also periodic.
- The electron density is equivalent to the square of the wave function magnitude, thus the magnitude of the wave function is also periodic.

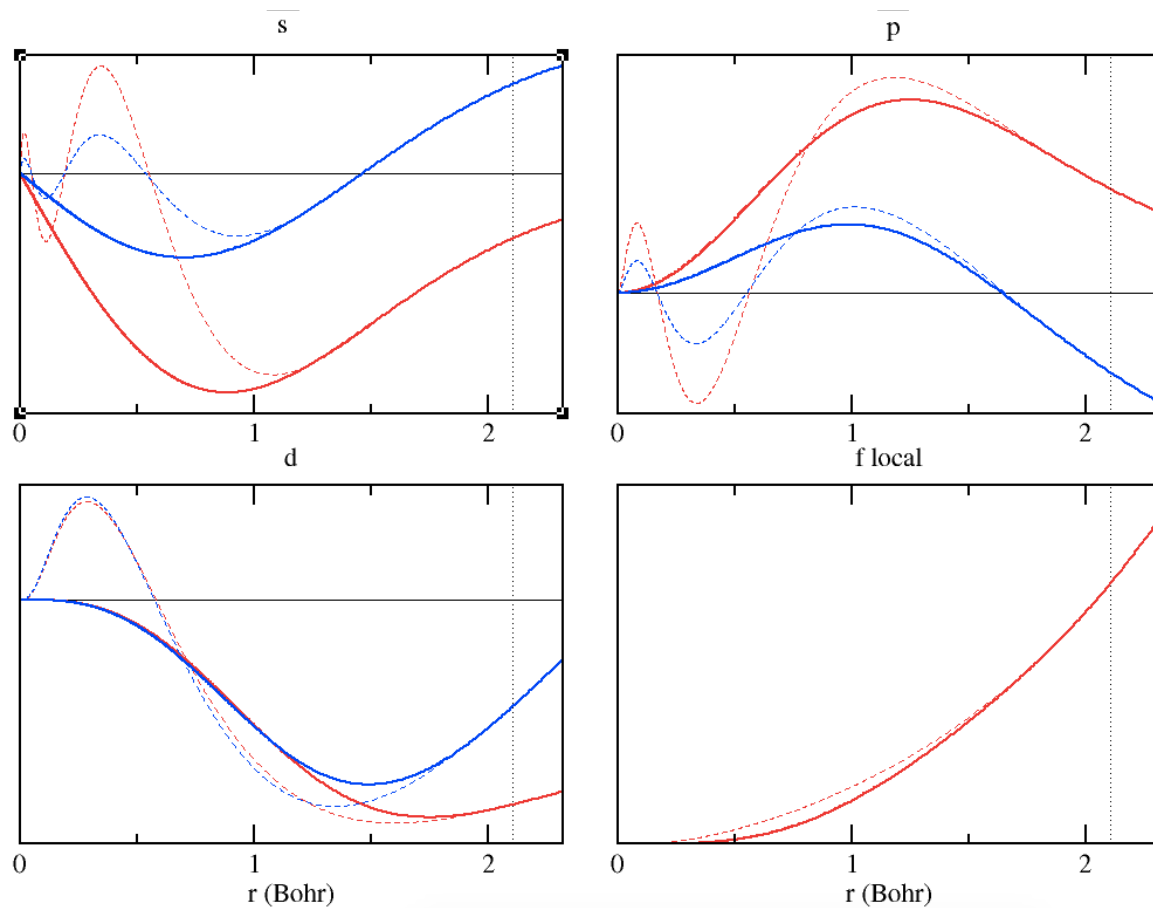


Figure 3.3: Plots of the valence s , p and d orbital potentials for zirconium. Dashed lines show the all-electron potentials while solid lines indicate the corresponding pseudopotential. Dotted vertical line marks the radius beyond which the potentials match.

Knowing that the magnitude of the wave function is periodic greatly simplifies the calculation process; only one ‘period’ of the function needs to be evaluated. However, the phase of the wave function can take any of an infinite number of values and still satisfy the periodicity condition. At this point, we consider Bloch’s theorem which states that the possible wave functions are all quasi-periodic, and thus the wave function can be expressed as in Equation 3.7:

$$\psi_k(\mathbf{r}) = e^{i\mathbf{k}\cdot\mathbf{r}} u_k(\mathbf{r}) \quad (3.7)$$

Where $\psi_k(\mathbf{r})$ is the wave function evaluated at position \mathbf{r} , $e^{i\mathbf{k}\cdot\mathbf{r}}$ is an arbitrary phase factor, and $u_k(\mathbf{r})$ is a periodic function with the same periodicity as the wave function. Solutions to this equation exist for any value of \mathbf{k} and so the general solution can be expressed as an integral over the first Brillouin zone, the primitive lattice cell in reciprocal space. Instead of evaluating the integral over the range of \mathbf{k} (a computationally costly task as it is done for many wave functions), a sum of values at discrete points, known as k-points, is used. This approximation is valid because the wave function varies slowly over \mathbf{k} , thus allowing the integral to be approximated with several appropriately space k-points. In general, a finer k-point grid results in increased accuracy, but at an increased computational cost [38].

3.2.2 Plane-waves

Describing the electron density of a system is done in the context of a basis set. A basis set is simply a collection of functions (known as basis functions) which can be combined to produce some relevant output, typically the mathematical description for the shape of an electron orbital. For example, any sound wave can be generated from a combination of sine functions (basis functions). The purpose of a basis set is to describe the varying amplitude of the electron density in space. Any complete basis set (plane-wave, correlation-consistent, split-valence) may be used to represent the behaviour of electron orbitals, but a plane-wave method was chosen due to their greater suitability for periodic systems (plane-waves are intrinsically periodic).

Figure 3.6 shows the first convergence study where the total energy of simulations with various

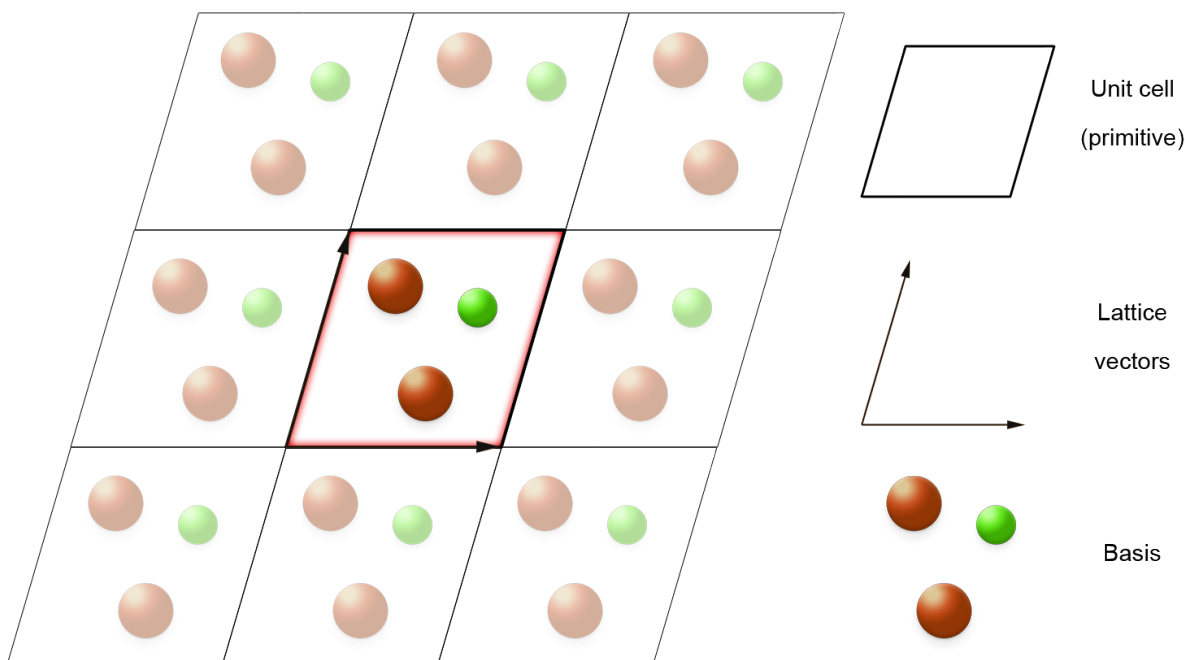


Figure 3.4: Two dimensional illustration of periodic boundary around a primitive cell.

values of E_{cutoff} were compared to a highly converged value, and then plotted on a log scale to see how precision is improved at larger values.

3.3 Computational details

3.3.1 Cell dimensions and initialisation

A supercell method is used for the study of various defects. The first step is to create a unit cell of ZrO_2 in each of the three crystal structures. Each unit cell is then fully relaxed through a geometry optimisation process (see 3.3.2). The resulting cell is then used to construct supercells through tessellation in three dimensions, before being fully relaxed again. This way, we generate systems with up to ten times as many atoms as the unit cell (supercell details can be found in Table 3.1). This is necessary because introducing defects into a small unit cell will result in the defect interacting with itself across the periodic boundary. A supercell increases the distance between the defect and its periodic image, using the bulk material as an interaction buffer. When constructing a supercell, it is important to consider making the supercell equally large in

all directions, such that any directional bias in defect-defect interaction is minimised. Larger supercells carry an increased computational cost when running calculations, limiting the sizes we can achieve. For example, a constant-volume defect calculation with 300 atom supercells will take upwards of 500 hours to complete, whereas the equivalent 100 atom supercell will take just 72 hours (fully relaxed calculations are even more computationally expensive).

Table 3.1: Composition of the supercells in terms of the number of individual unit cells stacked in each direction.

| Crystal Structure | No. unit cells | | | Supercell size (Å) | | | No. atoms |
|------------------------------|-----------------------|---|---|---------------------------|-------|-------|----------------------|
| | a | b | c | a | b | c | |
| Monoclinic ($P2_1/c$) | 2 | 2 | 2 | 10.37 | 10.47 | 10.75 | 96 |
| Tetragonal ($P4_2/nmc$) | 3 | 3 | 2 | 10.85 | 10.85 | 10.56 | 108 |
| Cubic ($Fm\bar{3}m$) | 2 | 2 | 2 | 10.22 | 10.22 | 10.22 | 96 |

3.3.2 Geometry optimisation

The geometry optimisation task in CASTEP follows a simple steepest-descent algorithm which attempts to satisfy certain convergence criteria, depending on the constraints applied to the system. This is an iterative process which takes an initial system state, modifies ion positions slightly and then calculates the difference in properties between the states to check for convergence. The variational principle in quantum mechanics tells us that the lowest system energy calculated is always an upper bound for the ground state energy, thus providing a quick and easy way to check if modifications to the system are actually optimising the geometry. The exception is when the system converges upon a local minima which may or may not be an experimentally observed state. This can be avoided to some extent by having good initial ion placement to optimise from.

3.3.3 Convergence criteria for geometry optimisation

Four convergence criteria are used for the geometry optimisation tasks throughout this work, one of which is only used when performing constant-pressure calculations, such as when a supercell is being fully relaxed. These criteria are evaluated with respect to the previous iteration during the geometry optimisation task:

- *Change in energy per ion* : The largest change in the energy per ion between iterations must be below 10^{-5} eV. Below this value, the total energy improvement towards the ground state for a 100 atom supercell is less than 0.001 eV, and is therefore considered converged.
- *Maximum force on an ion* : The maximum force requirement on any single ion in an iteration must be below 10^{-2} eV/Å. This is required to make sure that the ion position will not change significantly in the following iteration, possibly bringing another convergence criterion above its threshold.
- *Maximum change in ion position* : This must be below 5×10^{-4} Å between iterations to be considered converged. This criterion specifies the maximum ‘rattle’ of the ion that is tolerated once the minimum energy is reached (i.e. displacements above this value may still be important for achieving a correct atomic configuration).
- *Maximum stress (constant-pressure only)* : During unconstrained relaxation, the maximum stress between iterations should be below 5×10^{-2} GPA.

3.3.4 Charged cell correction

When calculating the energy of a system with an overall non-zero charge, this charge introduces a systematic error in the energy value which is a function of the charge magnitude.

- Screened Madelung
- Brouwer diagram script uses screened Madelung constant for the calculation

3.3.5 Stiffness tensor generation

- Calculate DFT energies of unit cell with small strains in various directions
- Use relative change in stress to calculate elastic constants in the form of a 6x6 tensor

3.3.6 Strain method for defect volumes

The volumes of the defective supercells were kept constant because constant pressure calculations have been shown to break the symmetry of the supercell [39], leading to unreliable energy values. The approach to calculating defect volumes relies on calculating the elastic constants of the non-defective supercell, followed by extracting the resultant stress tensor from a defect simulation. The strain tensor of the defective cell can then be calculated using Hooke's law, giving the relaxation volume.

3.3.7 Isobaric method for defect volumes

It is also possible to calculate defect volumes using an isobaric method. This method is more simple than the strain method as there is no need to determine the elastic constants, reducing the number of geometry optimisation jobs from 36 to 1.

After a calculation, CASTEP provides the volume of the resulting cell, defined as the volume enclosed by the calculated lattice parameters. By subtracting the volume of a relaxed, non-defective cell from the volume of a relaxed, defective cell, we obtain a value for the total defect volume.

It is important to consider that if there is a non-zero charge on the system, this will affect the calculated volume. This is because two systems with the same type, amount and arrangement of atoms, but different overall charges, will have different energies (due to the number of electrons). Different electronic orbital occupancies will affect the inter-atomic forces and therefore the shape of the cell.

3.4 Defect equilibria

Brouwer diagrams, also known as Kröger-Vink diagrams, were produced using a method outlined by Murphy et al. [40] to determine defect concentrations as a function of oxygen partial pressure. We start from the statement that the chemical potential of ZrO_2 is equivalent to the sum of the chemical potentials μ of its constituent species, Zr and O:

$$\mu_{\text{ZrO}_2(s)} = \mu_{\text{Zr}}(p_{\text{O}_2}, T) + \mu_{\text{O}_2}(p_{\text{O}_2}, T) \quad (3.8)$$

where T denotes temperature and p_{O_2} denotes oxygen partial pressure. The chemical potential of ZrO_2 in the solid state is assumed to have negligible dependence on T and p_{O_2} relative to μ_{Zr} and μ_{O_2} . Energies can be obtained for bulk ZrO_2 and Zr, but the ground state of oxygen is not correctly reproduced in DFT [41, 42]. Instead, we use the approach of Finnis et al. [43] to infer the oxygen chemical potential from standard state values. We can use the experimental Gibbs free energy to produce an equation where μ_{O_2} is the only unknown:

$$\Delta G_{f, \text{ZrO}_2}^{\ominus} = \mu_{\text{ZrO}_2(s)} - (\mu_{\text{Zr}(s)} + \mu_{\text{O}_2}^{\ominus}) \quad (3.9)$$

where $\Delta G_{f, \text{ZrO}_2}^{\ominus}$ is the experimental Gibbs energy at standard temperature and pressure and $\mu_{\text{O}_2}^{\ominus}$ is the oxygen chemical potential under the same conditions. The values of $\mu_{\text{ZrO}_2(s)}$ and $\mu_{\text{Zr}(s)}$ are calculated from the DFT energies. Once $\mu_{\text{O}_2}^{\ominus}$ is calculated, we can generalise the chemical potential of oxygen for any value of T and p_{O_2} by appending an ideal gas relationship $\Delta\mu(T)$ and a Boltzmann distribution:

$$\mu_{\text{O}_2}(p_{\text{O}_2}, T) = \mu_{\text{O}_2}^{\ominus} + \Delta\mu(T) + \frac{1}{2} k_B \log\left(\frac{p_{\text{O}_2}}{p_{\text{O}_2}^{\ominus}}\right) \quad (3.10)$$

Using our generalised formula for μ_{O_2} , we fix the temperature within the range of thermal phase-stabilisation (1500 K for tetragonal ZrO_2) and calculate μ_{O_2} for many different values of p_{O_2} between 10^{-35} and 10^0 atm, corresponding to oxygen deficient and oxygen rich environments,

respectively (p_{O_2} in air is approximately 0.2 atm). While the tetragonal phase will be stress-stabilised in practice, thermal-stabilisation in such models has been shown to qualitatively approximate the effect of stress-stabilisation, while allowing a wider range of dopant behaviours to be predicted [44]. Equilibrium defect concentrations are then calculated at each μ_{O_2} and plotted against p_{O_2} to produce a Brouwer diagram.

3.4.1 Effect of space charge

The difference in the diffusion rate of oxygen vacancies compared to electrons lead to a build-up (and therefore a resultant) charge in the lattice. In the case of ZrO_2 , we know that this effect will be pronounced due to the small thickness of the layer. We can take this effect into account when generating Brouwer diagrams by assuming an overall charge in the crystal structure instead of charge-neutrality.

Figure 3.5 shows an example of the defect equilibria in tetragonal ZrO_2 with an overall positive space charge. In order for such a condition to be satisfied, higher concentrations of positively charged oxygen vacancy and hole defects are predicted to be present. When extrinsic defects are also present in the lattice in significant concentrations, the space charge condition may influence which defect types are dominant at different oxygen pressures, as different oxidation states may be necessary to satisfy the charge condition.

3.5 Convergence testing

3.5.1 Plane-wave cut-off energy

In order to determine an appropriate value for the plane-wave cut-off energy, a convergence test was performed to determine the relative error in predicted energy compared to a highly converged value. This convergence test was conducted by running multiple geometry optimisation procedures under fully relaxed conditions on a unit cell of ZrO_2 for each phase. A very

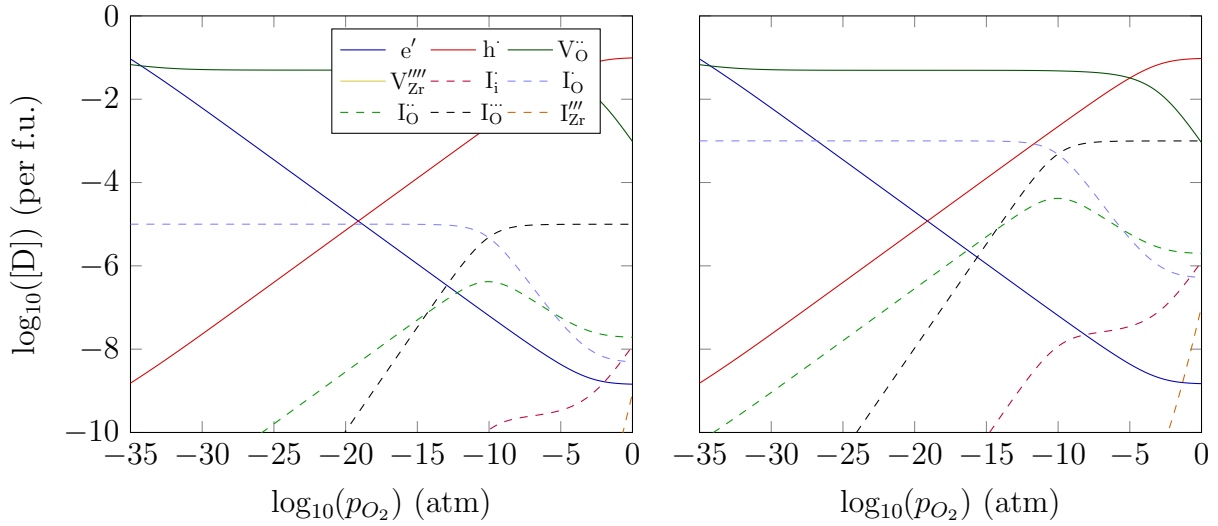


Figure 3.5: Tetragonal phase Brouwer diagrams of point defects at iodine concentrations of a) 10^{-5} and b) 10^{-3} , at a temperature of 1500 K. Space charge = 10^{-1}

small k-point spacing of 0.01 \AA^{-1} was used for each task (highly converged), while increasing the plane-wave cut-off energy from 300 eV to 750 eV in 50 eV increments. The energy of each run was recorded and compared to the energy of a highly converged value taken when a cut-off energy of 900 eV was used. This provides a value for the truncation error at different cut-off energies. Figure 3.6 shows a log plot of the energy error for each phase of ZrO_2 as the cut-off energy is increased.

The error is shown to be independent of phase, with all lines lying on a single path. This is expected because the atoms in each phase are the same, and therefore the electrons involved in the calculations remain unchanged. A cut-off energy of 600 eV was found to produce an error below 0.01 eV, and was subsequently used for future calculations as it provides a good compromise between computational cost and accuracy.

3.5.2 k-point convergence

Too fine a grid in reciprocal space (i.e. a large number of k-points) results in prohibitively computationally expensive simulations, whereas too coarse a grid may have a large truncation error when energies are calculated. To find the optimum spacing of k-points, a convergence

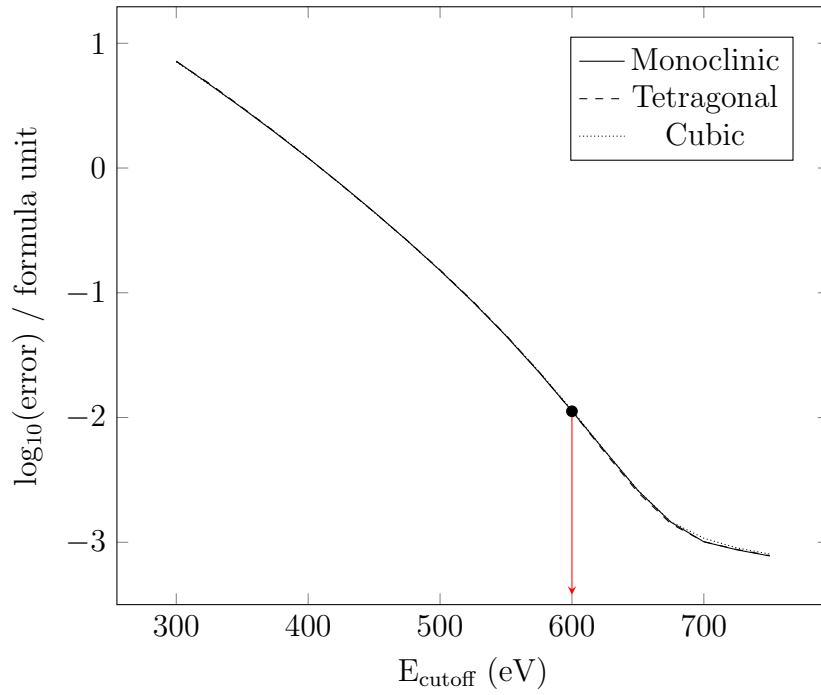


Figure 3.6: Plot of the log error of DFT energy against plane-wave cut-off energy for a perfect cell of each crystal structure. The error is calculated with respect to a highly converged value, calculated at a plane-wave cut-off energy of 900 eV. The red arrow indicates the cut-off energy beyond which the error is below 2 decimal places.

study was performed across a range of k-point spacings, with the output energies compared to a highly converged simulation to obtain a value for the error.

Figure 3.7 shows the energy error for each phase of ZrO_2 as a function of the k-point spacing (given in reciprocal space as \AA^{-1}). The highly converged energy value was calculated with a k-point spacing of 0.01 \AA^{-1} for error calculations. The plot shows a stepwise change in the error value as grid spacing is reduced because there must be an integer number of k-points, but larger spacings do not provide sufficient resolution to effectively fit an integer number of k-points into the reciprocal grid, snapping to the nearest appropriate grid instead. An optimum k-point spacing was chosen at 0.09 \AA^{-1} , which was the largest spacing that kept the error below 0.01 eV for all phases, highlighted in the plot by the red arrow.

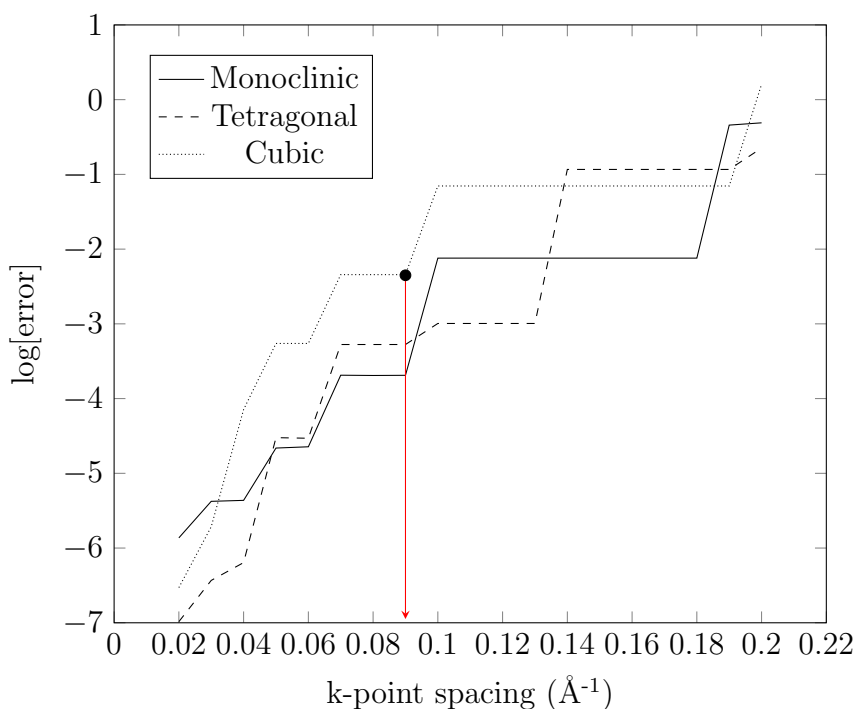


Figure 3.7: Log of the error in the total energy of the system as a function of k-point spacing. The error is calculated relative to a highly converged energy value at a k-point spacing of 0.01 \AA^{-1} . The red arrow indicates the k-point spacing, which ensures an error below 2 decimal points for all structures.

3.5.3 Exchange-correlation functionals

There are a range of possible exchange-correlation functionals available in CASTEP, spanning both empirical and non-empirical types. Empirical exchange-correlation functionals are typically used to capture specific properties or systems particularly well, but perform poorly for generalised systems. Non-empirical exchange-correlation functionals, while still not perfect, are preferred for modelling the widest range of properties. In a sense, non-empirical functions benefit from not being ‘over-fit’ to experimental data. They are also used far more often in the literature, thus providing a rich corpus of work for comparison studies.

While we had already selected the PBE-GGA exchange-correlation functional in this work, it was helpful to conduct a convergence study of our system across all the functionals available in CASTEP in order to see how other functionals compared.

3.5.4 On-the-fly pseudopotentials

Ultra soft pseudopotentials are generated in CASTEP automatically (known as on-the-fly or OTF pseudopotentials) when none are specified for a particular element. Energies must be calculated and compared with the same set of pseudopotentials in order to keep simulations self-consistent. A quick single point calculation was performed on a unit cell of ZrO_2 and the resulting OTF pseudopotentials (one for oxygen and one for zirconium) were saved and used for all subsequent calculations.

It is important to determine the variance in energy values of different pseudopotentials generated in this way in order to avoid systematic error. To assess this error, 9 different pairs of OTF pseudopotentials were generated and used to calculate the total energy of a monoclinic ZrO_2 supercell. The difference in energy was then calculated with respect to the pseudopotential pair that resulted in the lowest energy. These deviations in total energy are shown in Figure 3.8. Across all calculations, the largest difference in total energy calculated was 0.0012 eV, while the average difference was 0.0006 eV. Since we are only concerned with choosing other parameters to achieve a precision of 0.01 eV, and the largest deviation calculated is an order of magnitude below that, we do not need to take any special measures to correct any systematic error from randomly generated OTF pseudopotentials.

3.5.5 Unit cells

Unit cells of ZrO_2 in each phase were fully relaxed at constant pressure and the resulting structures were compared to experimental data. Table 3.2 shows the calculated lattice parameters and energy differences between the three ZrO_2 phases.

The first thing to note is that the correct order of ZrO_2 phases is predicted in the total energy calculations, with monoclinic being the lowest energy phase and cubic being the highest. In addition, the energy difference between phases is small (< 0.1 eV/fu). This is a good indication that the choice of exchange correlation functional can reproduce the energy landscape of the system accurately. This is especially important for when defects are introduced because they

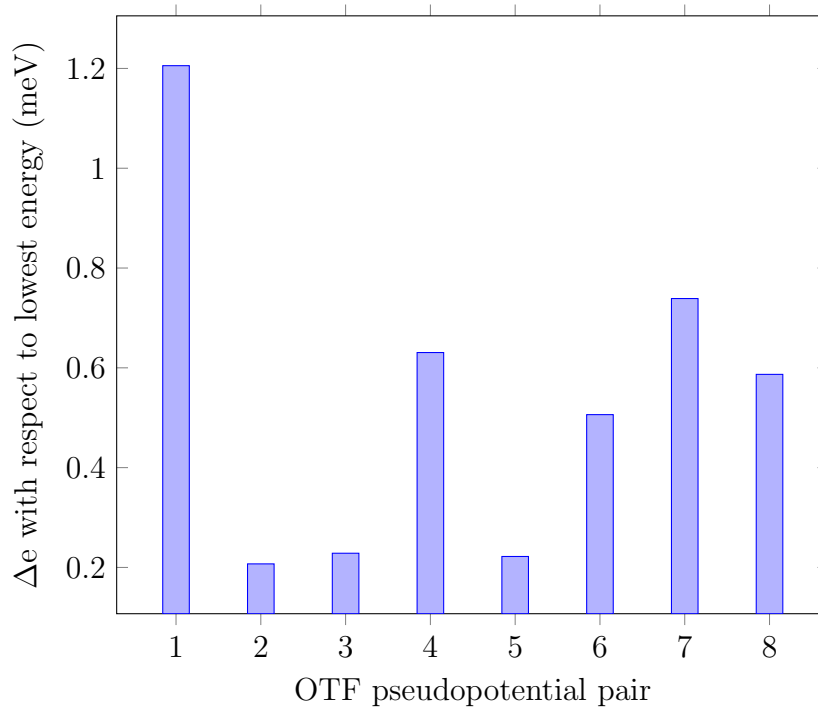


Figure 3.8: Energy deviation in meV of supercells with candidate OTF pseudopotential pairs. Energy deviations are shown with respect to the pseudopotential pair that resulted in the lowest total energy calculated.

may promote stabilisation of one phase over another, and an inaccurate model will not capture this behaviour.

Table 3.2: Calculated unit cell parameters for the different crystal structures of ZrO_2 . Experimental data for pure monoclinic and stabilised tetragonal and cubic phases at 295 K are shown in parentheses [2]. Energy difference between structures is shown with respect to the cubic phase.

| Phase | a (Å) | b (Å) | c (Å) | β (°) | V (Å ³ /fu) | ΔE (eV/fu) |
|-------------------|-------------|-------------|-------------|---------------|------------------------|--------------------|
| m- ZrO_2 | 5.18 (5.15) | 5.24 (5.21) | 5.37 (5.32) | 99.63 (99.23) | 35.96 (35.22) | -0.215 |
| t- ZrO_2 | 3.62 (3.61) | | 5.28 (5.18) | 90 | 34.54 (33.67) | -0.105 |
| c- ZrO_2 | 5.11 (5.09) | | | 90 | 33.38 (32.89) | N/A |

3.5.6 Chemical potential of iodine

To determine the chemical potential of iodine, an energy minimisation of the iodine dimer was performed. Unlike oxygen, iodine dimers do not exhibit a resultant magnetic moment, thus avoiding a source of error in energy calculations with the PBE exchange-correlation functional.

Similar to the ZrO_2 unit cell calculations, the lattice parameter after relaxation (bond length in this case) is compared to experimental data to assess the quality of the simulation parameters.

Figure 3.9 illustrates the energy minimisation of two iodine atoms in a large cell, initially separated by 3.0 \AA . The geometry optimisation task finds an energy minima when the iodine atoms are bonded, at a separation of 2.69 \AA . This agrees well with the experimental value of 2.6745 \AA [45].

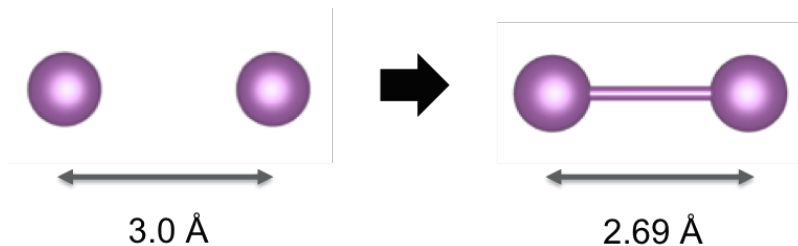


Figure 3.9: Energy minimisation of two iodine atoms from an initial separation of 3.0 \AA .

3.5.7 +U study

In some DFT studies, an additional potential energy term is sometimes included to better capture the Coulomb interaction of localised electrons. An LDA or GGA functional alone will typically not describe this interaction correctly, especially for localised d and f electrons. Of particular concern is the calculated value of the band gap from DFT simulations, as this value may deviate by up to 30% from experimental values. Remedying this shortcoming with an appropriate +U parameter could therefore be valuable in obtaining accurate energies. A +U study of the zirconium atom, with an electronic configuration of $[\text{Kr}]4d^25s^2$, was performed to determine the response to and therefore the viability of an additional potential term for the d electrons.

Figure 3.10 shows the effect on the calculated band gap when introducing a +U term. While the +U term does increase the band gap, the effect is insignificant. Even with +U terms of 10 eV, the calculated band gap falls short of the experimental band gap by at least 1.5 eV. Moreover, with +U terms greater than 4 eV, we begin to see erratic behaviour in the development of both the band gap, and also in the predicted crystal structure.

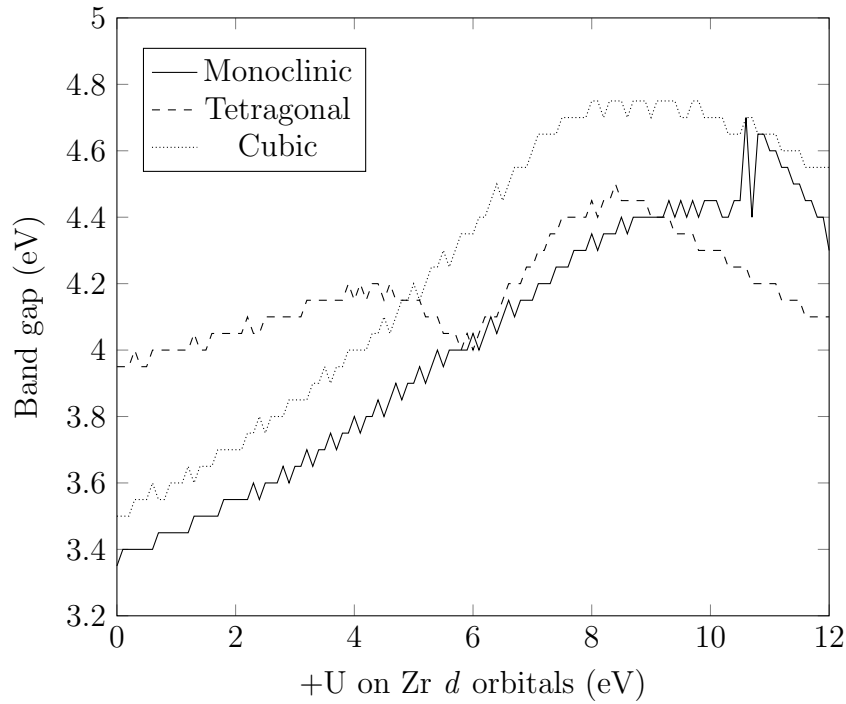


Figure 3.10: Calculated band gaps for different +U values in monoclinic, tetragonal and cubic ZrO_2 .

In monoclinic ZrO_2 , the use of a +U term causes the lattice parameters to change disproportionately, as seen in Figure 3.11. All lattice parameters increased with larger +U terms, however, expansion in the a direction proceeded faster than in the b direction, resulting in the a lattice parameter becoming larger at a +U of 4 eV. +U terms larger than 10.5 eV caused the lattice parameters to snap suddenly onto new values. An investigation of the atomic positions revealed that the monoclinic crystal structure had collapsed into an orthorhombic structure, with the co-ordination number of zirconium ions falling to 6 from 7.

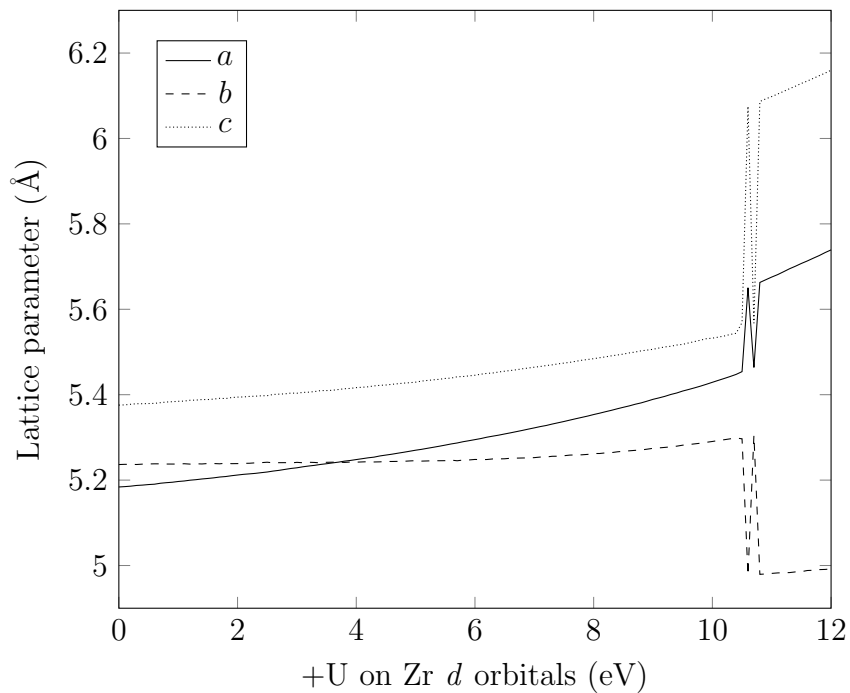


Figure 3.11: Individual lattice parameters as a function of +U term in monoclinic ZrO₂.

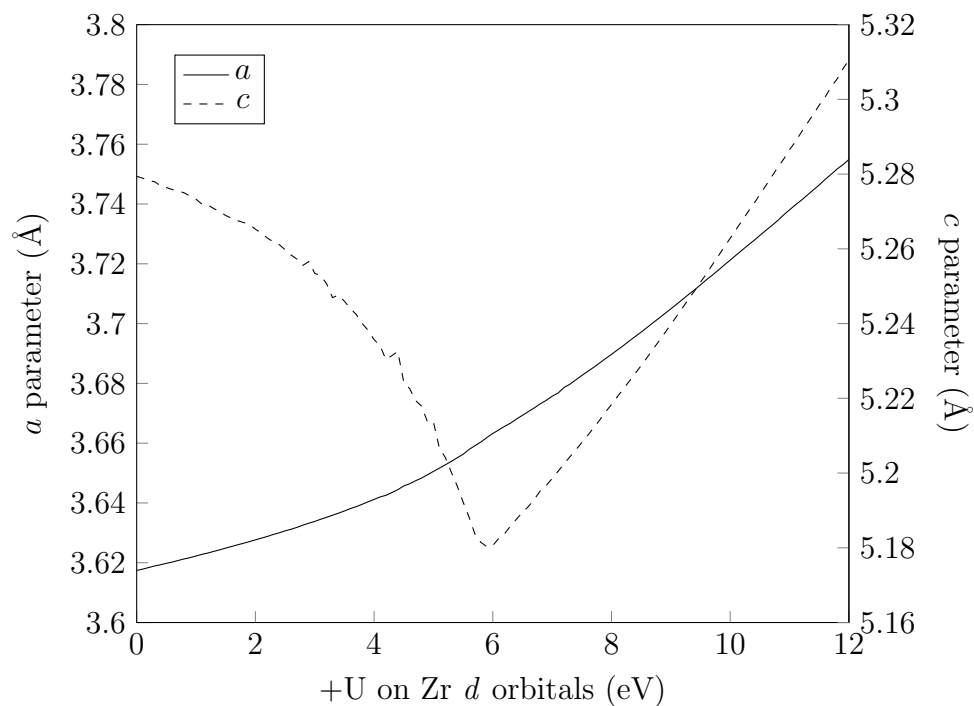


Figure 3.12: Individual lattice parameters as a function of +U term in tetragonal ZrO₂.

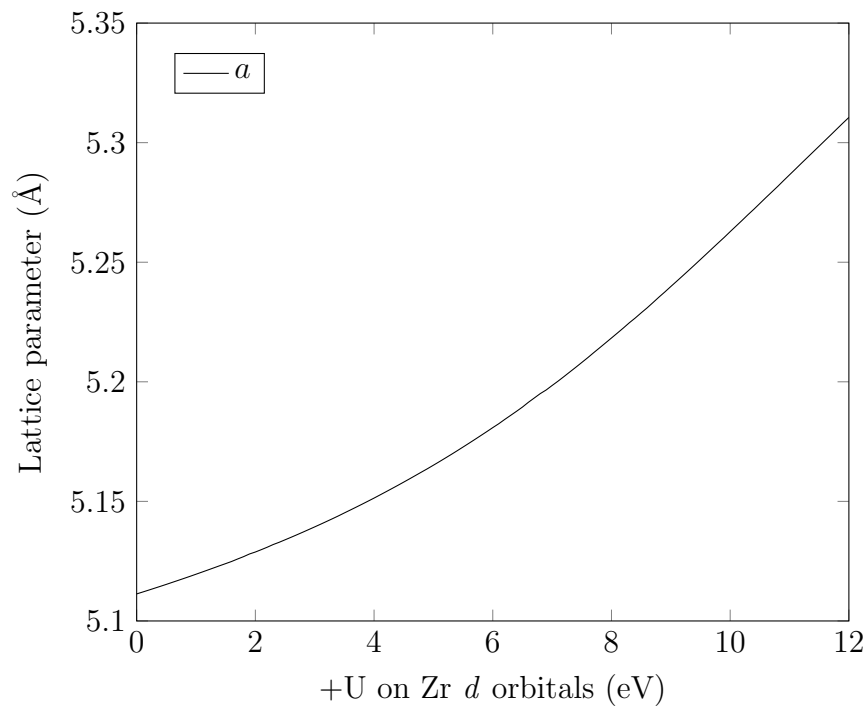


Figure 3.13: Individual lattice parameters as a function of +U term in cubic ZrO_2 .

Chapter 4

Defects

4.1 Placeholder

4.1.1 Incorporation and defect formation energies

Isolated Frenkel defects

Zr and O Frenkel defect formation energies were determined via point defect DFT calculations for the three structures. The formation energies of the isolated Frenkel defect pairs were defined as:

$$E_{Frenkel} = E_{DFT}(V_X^q) + E_{DFT}(X_i^{-q}) - 2E_{DFT}(ZrO_2) \quad (4.1)$$

where X is either Zr or O, $E_{DFT}(V_X^q)$ is the energy of a supercell of ZrO_2 containing a single vacancy of charge q , $E_{DFT}(X_i^{-q})$ is the energy of a supercell of ZrO_2 containing a single interstitial with opposing charge $-q$, and $E_{DFT}(ZrO_2)$ is the energy of the non-defective supercell. Charges ranged from the fully charged case (+2 for oxygen vacancies, -4 for zirconium vacancies) to neutral. The interstitial sites, shown in Table 4.1, were chosen based on standard vacant Wyckoff positions in each crystal structure [46]. In the case of oxygen vacancies in monoclinic

ZrO₂, a defect energy was obtained for both the (III) and (IV) co-ordinated oxygen sites, with the lowest energy value being used in the calculation of the Frenkel defect energy.

Table 4.1: Wyckoff positions of interstitial sites used for each crystal structure.

| Crystal Structure | Interstitial Sites |
|-------------------|--------------------|
| Monoclinic | 2a, 2b, 2c, 2d |
| Tetragonal | 2b, 8e |
| Cubic | 24d, 4b |

Isolated Schottky Defects

Three Schottky energies were calculated for each structure, corresponding to fully charged, partially charged, and uncharged point defect energies. The Schottky formation energy was defined as:

$$E_{Schottky} = E_{DFT}(V_{Zr}^{-2q}) + 2E_{DFT}(V_O^q) - \frac{3(n-1)}{n}E_{DFT}(ZrO_2) \quad (4.2)$$

where n denotes the number of atoms in the supercell, V_O^q denotes an oxygen vacancy with charge q , and q varies from 2 to 0. This form maintains both the mass and charge balance of the Schottky defect description for ZrO₂:

$$Zr_{Zr}^x + 2O_O^x = V_{Zr}^{-2q} + 2V_O^q + ZrO_2 \quad (4.3)$$

This implies a rearrangement rather than complete removal of ions from the system. As with the Frenkel defects, the lowest energy vacancy energies were used to calculate Schottky formation energies. While there are multiple configurations of Schottky defects, such nuance cannot be accurately represented through a sum of individual vacancy defect energies. The values we present for Schottky defect formation energies should therefore be considered the lower bound for defect formation.

Bound Frenkel Defects

Bound Zr and O Frenkel defect formation energies in the three structures were calculated from DFT energies of supercells where a single ion was moved from its lattice site to an interstitial site. The formation energies of the bound Frenkel defect pairs were defined as:

$$E_{BoundFrenkel} = E_{DFT}(BoundFrenkel) - E_{DFT}(ZrO_2) \quad (4.4)$$

where $E_{DFT}(BoundFrenkel)$ is the energy of a supercell of ZrO_2 containing both a vacancy and interstitial defect of the same ion. The two defects were placed as far apart in the supercell as possible (7-8 Å) to avoid recombination. The interstitial defect is assumed to fully compensate the charge of the vacancy defect, resulting in no overall charge on the supercell. The number and type of ions in the defective and non-defective supercell are the same, requiring no further steps to calculate the formation energy.

Bound Schottky Defects

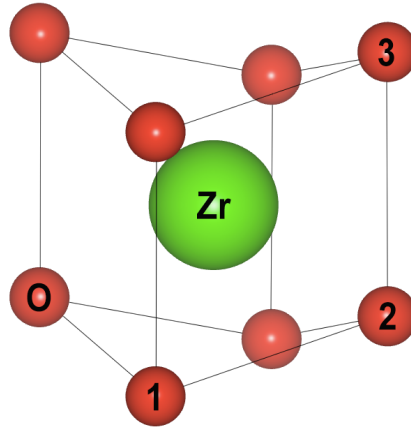


Figure 4.1: Zirconium centre showing nearest oxygen atoms in tetragonal ZrO_2 . Schottky trios indicated by oxygen enumeration. Zirconium atoms are shown in green and oxygen atoms in red.

Bound Schottky defects were modelled in a supercell of ZrO_2 by removing one Zr and two O atoms, in one of several possible nearest neighbour configurations as shown in Figures 2.3, 4.1 and 4.2. Charge neutrality is maintained by the removal of a stoichiometric unit, therefore

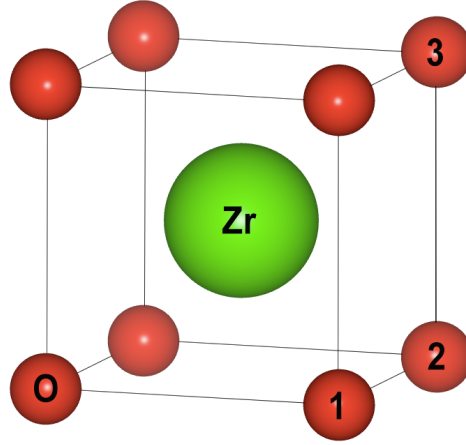


Figure 4.2: Zirconium centre showing nearest oxygen atoms in cubic ZrO_2 . Schottky trios indicated by oxygen enumeration. Zirconium atoms are shown in green and oxygen atoms in red.

these defects were defined as neutral tri-vacancies (NTVs). The NTV formation energy was defined as:

$$E_{NTV} = E_{DFT}(NTV) - \frac{n-3}{n} E_{DFT}(\text{ZrO}_2) \quad (4.5)$$

Where $E_{DFT}(NTV)$ is the energy of a supercell containing the NTV defect. As the defective supercell contains three fewer ions than the non-defective cell, the energy of the non-defective cell was adjusted by a proportional factor in our calculation. This form maintains both mass and charge balance of the Schottky defect description for ZrO_2 described in Equation 4.3.

4.2 Brouwer diagrams

4.2.1 Defect equilibria

Typically in materials, several types of defects will exist simultaneously. These defects will be present at an equilibrium concentration based on their thermodynamic stability. There are several considerations to be made. For example, we expect a crystal lattice to be overall charge-neutral, otherwise we would see extreme behaviour at the macro scale which is not indicative

of a low-energy state.

4.2.2 Oxygen pressure dependence

The equilibrium concentration of defects will be a function of the oxygen partial pressure, amongst other things like temperature and dopant concentrations. For materials in an equilibrium state, they are necessarily in equilibrium with their surroundings. This is why even metals in evacuated vacuum flasks will produce a metal vapour pressure. In the case of ZrO_2 in nuclear fuel cladding, we know that the ambient oxygen pressure will change over time. In particular, fission of UO_2 will result in the liberation of oxygen. This will result in an input of gaseous oxygen in the fuel cladding with increasing burn-up. The main oxygen sink is the Zr fuel cladding, into which the oxide grows. Other oxygen sinks include the oxidation of UO_2 to the ground state oxide U_3O_8 , and oxidation of fission products. Oxidation of UO_2 is a slow process whose kinetics are largely independent of the oxygen partial pressure [47], and will be slowed as free space in the cladding is reduced because it results in swelling of the fuel pellet.

Chapter 5

Intrinsic defect study

5.1 Introduction

5.1.1 Applications

It is important to fully understand the intrinsic defect structure of ZrO_2 because useful material properties may be exploited to improve performance, e.g. by doping with other ions to stabilise one crystal structure. For example, ZrO_2 doped with enough yttrium cations will stabilise the cubic phase and increase the concentration of oxygen vacancies, which is the main charge carrier in a YSZ solid oxide fuel cell.

5.1.2 Crystal structures

ZrO_2 grown at standard conditions on Zr metal exists mainly in either the monoclinic or tetragonal phase [2,48]. A high temperature cubic phase has also been observed in pure ZrO_2 , but it's similarity to the tetragonal phase often leads to them being mischaracterised in experimental studies.

5.1.3 Previous work

Previous works studying intrinsic defects in the ZrO_2 system have utilised quantum mechanical methods to determine defect formation energies in the monoclinic phase [49–51] and defect equilibria in the tetragonal phase [52]. The cubic phase is mainly studied as a dopant-stabilised system [53,54], with few undoped defect studies in the literature [55,56]. Building upon previous quantum mechanical studies, we provide a comprehensive account of intrinsic defect energies, defect volumes, and defect equilibria for all three common crystal structures of ZrO_2 , using state-of-the-art, accessible methods.

5.2 Methodology

5.2.1 Simulation parameters

Density functional theory (DFT) calculations were performed using CASTEP 8.0 [57]. Ultra-soft pseudo-potentials were used throughout, employing a 600 eV cut-off energy. The Perdew, Burke and Ernzerhof (PBE) [58] parameterisation of the generalised gradient approximation (GGA) was used to describe the exchange correlation functional. A Monkhorst-Pack sampling scheme [59] was used for Brillouin zone integration, with a minimum k -point separation of 0.09 \AA^{-1} . The Pulay method for density mixing [60] was used to improve convergence of simulations.

The electrical energy convergence criterion was set to $1 \times 10^{-6} \text{ eV}$. The maximum force between atoms was limited to $1 \times 10^{-2} \text{ eV \AA}^{-1}$. A gradient-descent geometry optimisation task was run on the cell until consecutive iterations differed in energy and atomic displacement by less than $1 \times 10^{-5} \text{ eV}$ and $5 \times 10^{-4} \text{ \AA}$, respectively.

5.2.2 Temperature dependence

To determine the temperature dependence of the ground states for the pure crystal structures, a harmonic approximation method as described by Burr et al. was used [61,62]. A

constant-volume phonon calculation was performed for each structure, from which the vibrational enthalpy $H_{vib}(T, V)$ and entropy $S_{vib}(T, V)$ contributions to the Helmholtz free energy were calculated up to a temperature of 2500 K. The complete Helmholtz free energy $F(T, V)$ was then obtained by including the internal energy $U(V)$ and configurational entropy S_{conf} of the system:

$$F(T, V) = U(V) + H_{vib}(T, V) - TS_{vib}(T, V) - TS_{conf} \quad (5.1)$$

5.2.3 Defect formation energies

Defective formation energies are calculated using equation 5.2:

$$E_f = E_{def} - E_{perf} + \sum_i n_i \mu_i + q(\mu_e - E_{VBM}) + E_{corr} \quad (5.2)$$

where E_f is the formation energy, E_{def} is the energy of the defective supercell, E_{perf} is the energy of a non-defective supercell, q is the defect charge, E_{VBM} is the valence band maximum, μ_e is the Fermi energy and E_{corr} is a charged-cell correction term.

5.2.4 Brouwer diagrams

Brouwer diagrams, also known as Kröger-Vink diagrams, were produced using a method outlined by Murphy et al. [40] to determine defect concentrations as a function of oxygen partial pressure. We start from the statement that the chemical potential of ZrO_2 is equivalent to the sum of the chemical potentials μ of its constituent species, Zr and O:

$$\mu_{\text{ZrO}_2(s)} = \mu_{\text{Zr}}(p_{\text{O}_2}, T) + \mu_{\text{O}_2}(p_{\text{O}_2}, T) \quad (5.3)$$

where T denotes temperature and p_{O_2} denotes oxygen partial pressure. The chemical potential

of ZrO_2 in the solid state is assumed to have negligible dependence on T and p_{O_2} relative to μ_{Zr} and μ_{O_2} . Energies can be obtained for bulk ZrO_2 and Zr , but the ground state of oxygen is not correctly reproduced in DFT [41, 42]. Instead, we use the approach of Finnis et al. [43] to infer the oxygen chemical potential from standard state values. We can use the experimental Gibbs free energy to produce an equation where μ_{O_2} is the only unknown:

$$\Delta G_{f, \text{ZrO}_2}^{\ominus} = \mu_{\text{ZrO}_2(s)} - (\mu_{\text{Zr}(s)} + \mu_{\text{O}_2}^{\ominus}) \quad (5.4)$$

where $\Delta G_{f, \text{ZrO}_2}^{\ominus}$ is the experimental Gibbs energy at standard temperature and pressure and $\mu_{\text{O}_2}^{\ominus}$ is the oxygen chemical potential under the same conditions. The values of $\mu_{\text{ZrO}_2(s)}$ and $\mu_{\text{Zr}(s)}$ are calculated from the DFT energies. Once $\mu_{\text{O}_2}^{\ominus}$ is calculated, we can generalise the chemical potential of oxygen for any value of T and p_{O_2} by appending an ideal gas relationship $\Delta\mu(T)$ and a Boltzmann distribution:

$$\mu_{\text{O}_2}(p_{\text{O}_2}, T) = \mu_{\text{O}_2}^{\ominus} + \Delta\mu(T) + \frac{1}{2}k_B \log\left(\frac{p_{\text{O}_2}}{p_{\text{O}_2}^{\ominus}}\right) \quad (5.5)$$

Using our generalised formula for μ_{O_2} , we fix the temperature within the range of thermal phase-stabilisation (1500 K for tetragonal ZrO_2) and calculate μ_{O_2} for many different values of p_{O_2} between 10^{-35} and 10^0 atm, corresponding to oxygen deficient and oxygen rich environments, respectively (p_{O_2} in air is approximately 0.2 atm). While the tetragonal phase will be stress-stabilised in practice, thermal-stabilisation in such models has been shown to qualitatively approximate the effect of stress-stabilisation, while allowing a wider range of dopant behaviours to be predicted [44]. Equilibrium defect concentrations are then calculated at each μ_{O_2} and plotted against p_{O_2} to produce a Brouwer diagram.

5.3 Cubic phase collapse

- When some oxygen Frenkel defects were introduced to the cubic phase supercell, relaxation under constant volume conditions caused a collapse into a pseudo-tetragonal

structure.

- This indicated that the cubic phase as modelled in DFT may not be fully stable.
- Further investigation indicated that the structure of a supercell of c-ZrO₂ broke down even with constrained symmetry, a result corroborated by Burr et al. [63].

5.4 Defect formation energies

Defect volumes of isolated Frenkel defects can be seen in Table 5.1.

Table 5.1: Isolated cluster defect volumes in the three ZrO₂ structures.

| Defect | Relaxation Volume (Å ³) | | |
|--|-------------------------------------|------------|----------|
| | Monoclinic | Tetragonal | Cubic |
| $V_{\text{Zr}}''' + \text{Zr}_i^{\bullet\bullet\bullet}$ | 21.331 | 25.4702 | 21.1309 |
| $V_{\text{Zr}}''' + \text{Zr}_i^{\bullet\bullet}$ | 19.7155 | 23.3463 | 19.9954 |
| $V_{\text{Zr}}'' + \text{Zr}_i^{\bullet\bullet}$ | 18.1149 | 22.2525 | 19.68618 |
| $V_{\text{Zr}}' + \text{Zr}_i^{\bullet}$ | 19.78339 | 18.4096913 | 19.76396 |
| $V_{\text{Zr}}^{\times} + \text{Zr}_i^{\times}$ | 19.99485 | 18.1061 | 20.29223 |
| $V_{\text{O}}^{\bullet\bullet} + \text{O}_i''$ | 0.8839 | 2.4704 | 5.8217 |
| $V_{\text{O}}^{\bullet} + \text{O}_i'$ | 0.9486 | 5.032 | 4.1146 |
| $V_{\text{O}}^{\times} + \text{O}_i^{\times}$ | 0.9576 | 8.26065 | 7.83687 |
| $V_{\text{Zr}}''' + 2V_{\text{O}}^{\bullet\bullet}$ | 3.6979 | -7.647 | 2.9448 |
| $V_{\text{Zr}}'' + 2V_{\text{O}}^{\bullet}$ | 1.0707 | -4.7866 | 1.5564 |
| $V_{\text{Zr}}^{\times} + 2V_{\text{O}}^{\times}$ | 0.64517 | -0.8985 | 2.08973 |

5.5 Elastic constants and defect relaxation volumes

Table 5.4 shows the calculated elastic constants for the monoclinic, tetragonal, and cubic phases of ZrO₂. The cubic phase has the highest stiffness, likely due to the short Zr-O bond lengths in the energy-minimised structure (Figure 2.7). It is expected that at high temperatures where the cubic phase is stable, the resulting increase in bond length would cause a reduction in stiffness.

Table 5.2: Formation energies in eV of isolated ZrO_2 defects.

| Defect | Equation | Formation Energy (eV) | | |
|-------------------|---|-----------------------|------------|--------|
| | | Monoclinic | Tetragonal | Cubic |
| Zr Frenkel | $\text{Zr}_{\text{Zr}}^{\times} \rightarrow \text{V}_{\text{Zr}}^{\prime\prime\prime} + \text{Zr}_{\text{i}}^{\bullet\bullet\bullet}$ | 5.428 | 5.639 | 5.610 |
| | $\text{Zr}_{\text{Zr}}^{\times} \rightarrow \text{V}_{\text{Zr}}^{\prime\prime} + \text{Zr}_{\text{i}}^{\bullet\bullet}$ | 8.695 | 8.939 | 8.476 |
| | $\text{Zr}_{\text{Zr}}^{\times} \rightarrow \text{V}_{\text{Zr}}^{\prime\prime} + \text{Zr}_{\text{i}}^{\bullet}$ | 12.118 | 12.058 | 11.628 |
| | $\text{Zr}_{\text{Zr}}^{\times} \rightarrow \text{V}_{\text{Zr}}^{\prime} + \text{Zr}_{\text{i}}^{\bullet}$ | 16.021 | 15.696 | 13.319 |
| | $\text{Zr}_{\text{Zr}}^{\times} \rightarrow \text{V}_{\text{Zr}}^{\times} + \text{Zr}_{\text{i}}^{\times}$ | 20.563 | 20.094 | 18.170 |
| O Frenkel | $\text{O}_{\text{O}}^{\times} \rightarrow \text{V}_{\text{O}}^{\bullet\bullet} + \text{O}_{\text{i}}^{\prime\prime}$ | 4.457 | 4.000 | 3.728 |
| | $\text{O}_{\text{O}}^{\times} \rightarrow \text{V}_{\text{O}}^{\bullet} + \text{O}_{\text{i}}^{\prime}$ | 6.432 | 6.588 | 7.055 |
| | $\text{O}_{\text{O}}^{\times} \rightarrow \text{V}_{\text{O}}^{\times} + \text{O}_{\text{i}}^{\times}$ | 7.518 | 7.452 | 8.477 |
| Schottky | $\emptyset \rightarrow \text{V}_{\text{Zr}}^{\prime\prime\prime} + 2\text{V}_{\text{O}}^{\bullet\bullet}$ | 5.120 | 3.778 | 1.752 |
| | $\emptyset \rightarrow \text{V}_{\text{Zr}}^{\prime\prime} + 2\text{V}_{\text{O}}^{\bullet}$ | 11.353 | 10.832 | 9.624 |
| | $\emptyset \rightarrow \text{V}_{\text{Zr}}^{\times} + 2\text{V}_{\text{O}}^{\times}$ | 18.554 | 18.232 | 17.073 |

Table 5.3: Formation energies of bound defects in ZrO_2 .

| Defect | Formation Energy (eV) | | |
|-------------------|-----------------------|------------|--------|
| | Monoclinic | Tetragonal | Cubic |
| O Frenkel | 4.1212 | 4.0290 | 6.4397 |
| Zr Frenkel | 8.4232 | 7.8633 | 6.3274 |
| NTV1 | 5.2272 | 3.5813 | 2.6961 |
| NTV2 | 5.1405 | 4.2312 | 0.1798 |
| NTV3 | 4.6620 | 3.3623 | 2.4089 |

The monoclinic and tetragonal phases have similar stiffness in the principal axes, but vary significantly under shearing conditions. In particular, the tetragonal phase exhibits much smaller C_{44} and C_{55} components. This may be due to the strong directional anisotropy of the tetragonal phase due to the larger c parameter.

Table 5.4: Elastic constants for different phases of ZrO_2 from DFT calculations.

| Elastic Component | Stiffness (GPa) | | |
|-------------------|-----------------|------------|--------|
| | Monoclinic | Tetragonal | Cubic |
| C_{11} | 338.86 | 334.30 | 523.38 |
| C_{12} | 151.80 | 207.30 | 92.93 |
| C_{13} | 89.37 | 48.93 | 92.93 |
| C_{22} | 348.37 | 334.20 | 523.39 |
| C_{23} | 143.04 | 48.93 | 92.93 |
| C_{33} | 262.17 | 250.50 | 523.38 |
| C_{44} | 76.35 | 9.38 | 61.98 |
| C_{55} | 71.65 | 9.38 | 61.98 |
| C_{66} | 114.19 | 152.60 | 61.99 |

5.6 Helmholtz energies

The calculated Helmholtz energies plotted in Figure 5.1 show the correct order of stability for the three phases of ZrO_2 at low temperatures (monoclinic – > tetragonal – > cubic) . However, as temperature is increased, only a transition from monoclinic to tetragonal is seen. The cubic phase Helmholtz energy does fall below the monoclinic curve, but never below the tetragonal curve, thus predicting no tetragonal to cubic phase transition. It must also be noted that the transition temperatures are not predicted accurately. The tetragonal phase is predicted to have a lower energy than monoclinic at approximately 400 K.

5.7 Defect equilibria

The intrinsic defect equilibria are shown in Brouwer diagrams in Figures 5.2, 5.3 and 5.4. The monoclinic phase exhibits the smallest overall concentration of intrinsic defects due to the low

Table 5.5: Isolated defect volumes in the three ZrO_2 structures.

| Defect | Volume (\AA^3) | | |
|--|---------------------------|------------|----------|
| | Monoclinic | Tetragonal | Cubic |
| V_{Zr}'''' | 55.9495 | 67.4062 | 48.468 |
| V_{Zr}''' | 42.4752 | 51.0824 | 36.944 |
| V_{Zr}'' | 29.9013 | 34.2764 | 25.9264 |
| V_{Zr}' | 17.1031 | 18.4276 | 15.0761 |
| V_{Zr}^\times | 4.05915 | 4.70160 | 4.31893 |
| $\text{Zr}_i^{\bullet\bullet\bullet\bullet}$ | -34.6185 | -41.936 | -27.3371 |
| $\text{Zr}_i^{\bullet\bullet\bullet}$ | -22.7597 | -27.7361 | -16.9486 |
| $\text{Zr}_i^{\bullet\bullet}$ | -11.7864 | -12.0239 | -6.24022 |
| Zr_i^{\bullet} | 2.68029 | -0.0179087 | 4.68786 |
| Zr_i^\times | 15.9357 | 13.4045 | 15.9733 |
| $V_{\text{O}}^{\bullet\bullet}$ [4coord] | -22.5154 | -37.5266 | -22.7616 |
| V_{O}^{\bullet} [4coord] | -12.4114 | -19.5315 | -12.1850 |
| V_{O}^\times [4coord] | -0.686074 | -2.80005 | -1.1146 |
| $V_{\text{O}}^{\bullet\bullet}$ [3coord] | -26.1258 | | |
| V_{O}^{\bullet} [3coord] | -14.4153 | | |
| V_{O}^\times [3coord] | -1.70699 | | |
| O_i'' | 27.0097 | 39.997 | 28.5833 |
| O_i' | 15.3639 | 24.5635 | 16.2996 |
| O_i^\times | 2.66459 | 11.0607 | 8.95147 |

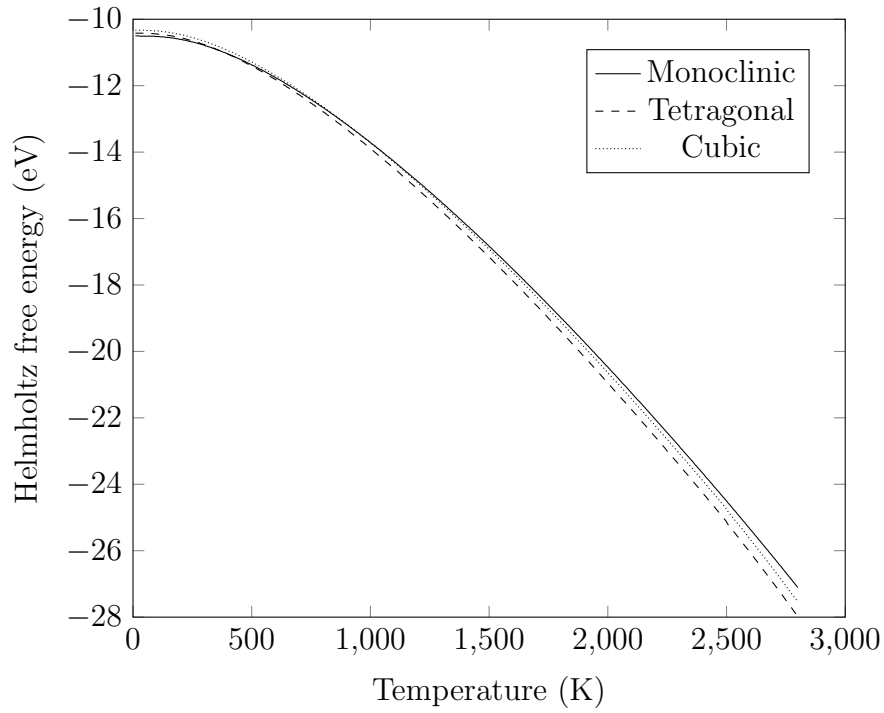


Figure 5.1: Helmholtz free energy as a function of temperature for the monoclinic, tetragonal, and cubic crystal structures of ZrO_2 .

temperature (650 K) relative to the other tetragonal (1500 K) and cubic (XXX K) phases.

5.8 Summary

The main defects in ZrO_2 are oxygen vacancies and zirconium vacancies at low and high oxygen pressures respectively.

The cubic phase cannot be modelled accurately due to instabilities outlined by Burr et al. in [REF] For this reason, it was decided that the cubic phase would not be considered when conducting extrinsic dopant simulation studies in ZrO_2 .

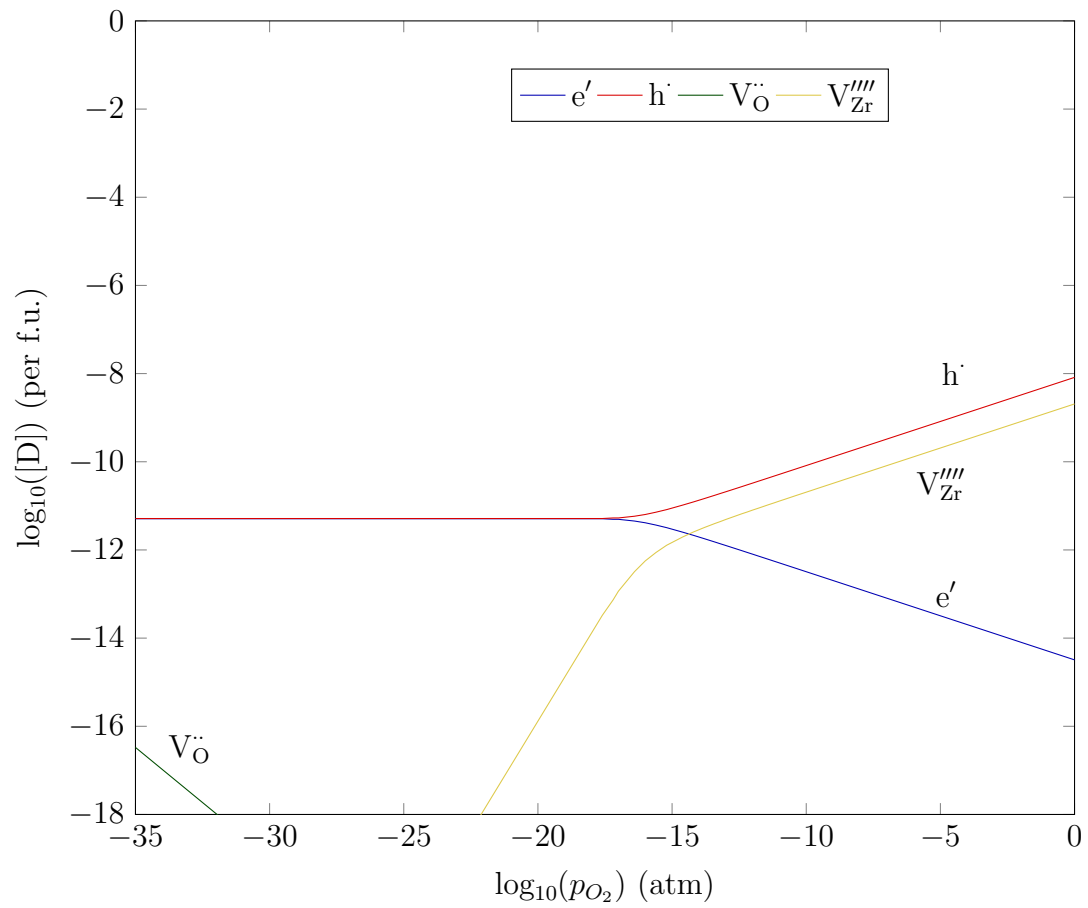


Figure 5.2: Monoclinic phase Brouwer diagram of intrinsic defects at 650 K.

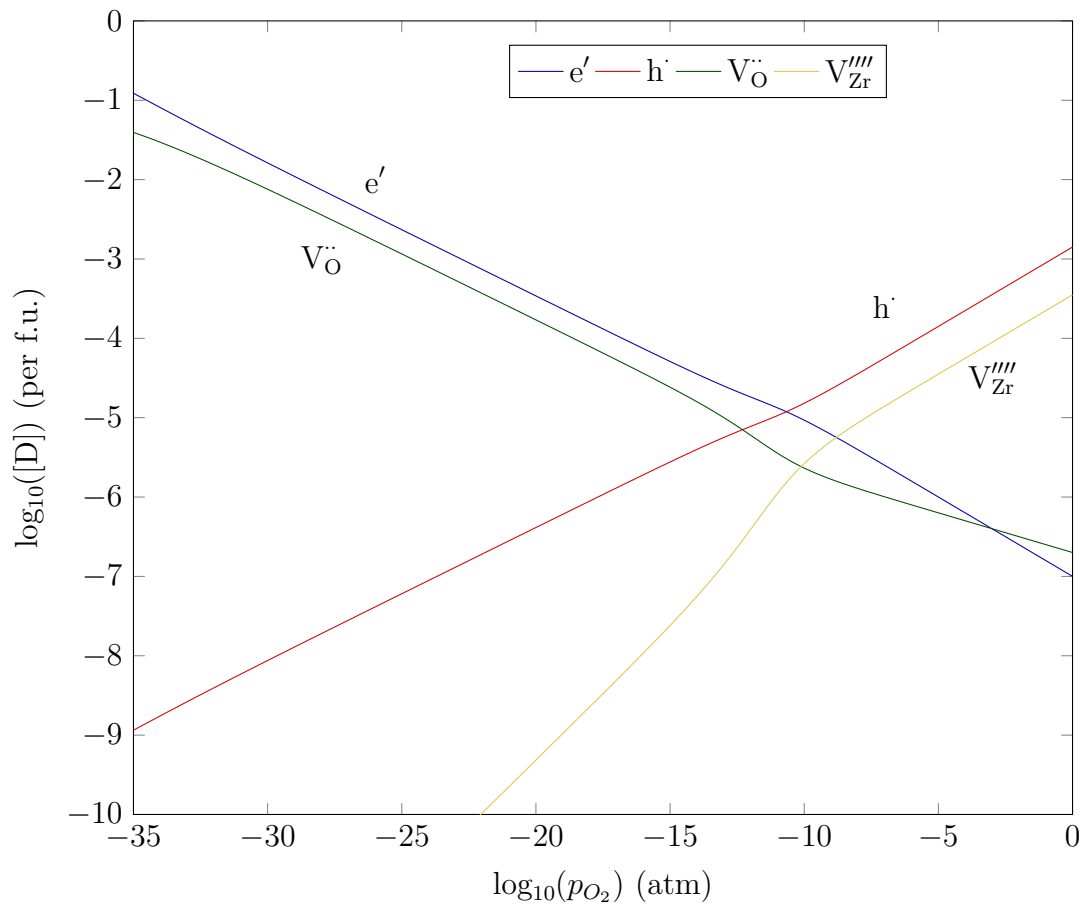


Figure 5.3: Tetragonal phase Brouwer diagrams of intrinsic defects at 1500 K.

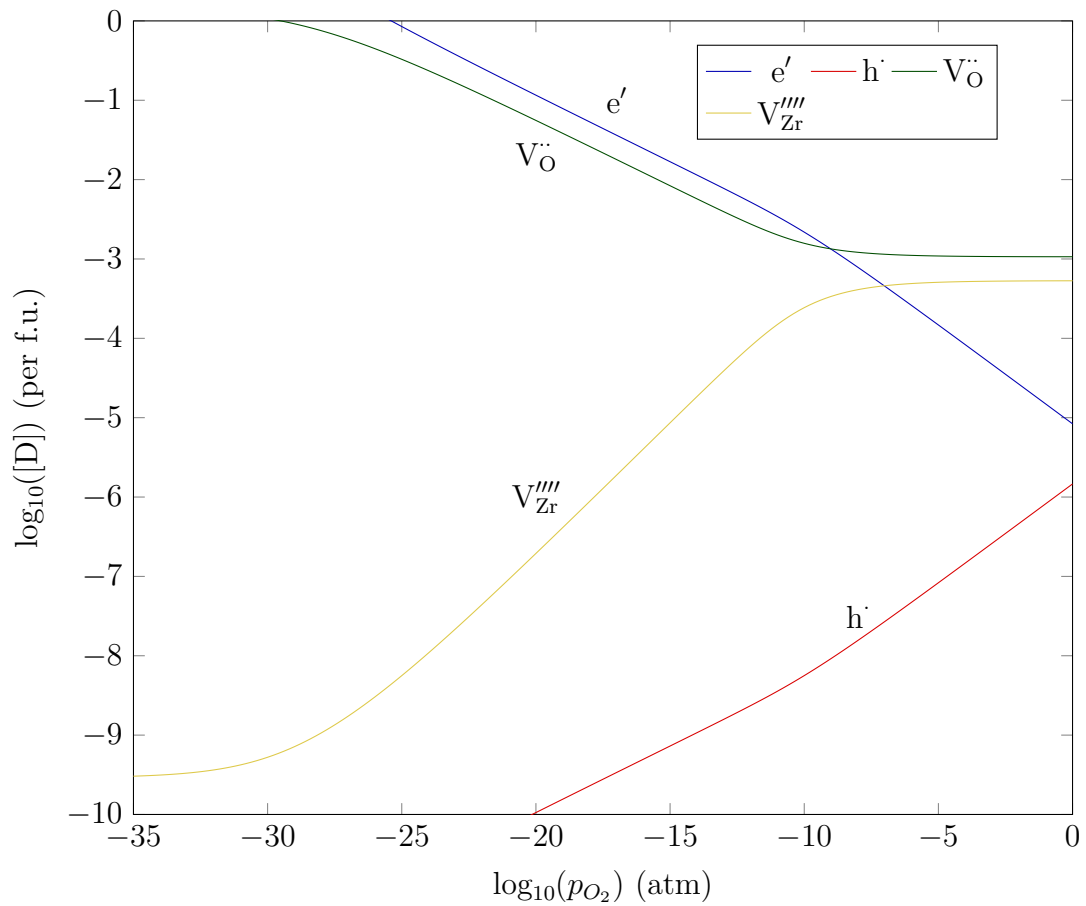


Figure 5.4: Cubic phase Brouwer diagrams of intrinsic defects at 2000 K.

Chapter 6

Iodine defect equilibria in ZrO_2

6.1 Introduction

Stress-corrosion cracking (SCC) in nuclear fuel pins is an issue related to early integrity of fuel assemblies in light water reactors (LWRs). SCC studies of the internal surface of zirconium-based fuel claddings have been conducted, which indicate that iodine is likely to be one of the main corrosive species involved in promoting crack growth [27, 64–66]. The exact mechanism for iodine SCC has not yet been determined due to difficulties observing the internal cladding surface in-situ, while experimental studies are not yet capable of reproducing the conditions under which such failures occur. We have therefore adopted a quantum-mechanical simulation approach to model the behaviour of iodine within the oxide layer of the cladding, the layer preceding the zirconium metal.

Iodine is produced in the fuel pellet directly from fission and also from the decay of tellurium precursors. Both iodine and tellurium are relatively common fission products, with combined independent yields from thermal fission of U_{235} above 5% [4, 5, 67–70]. The majority of thermal fission events occur in the outer rim of the fuel pellet, and a fission product penetration depth of up to 8 μm in ZrO_2 [71] suggests a large degree of implantation within the oxide and the Zr metal into which the oxide grows, raising the concentration of I well above the equilibrium value. Iodine and many of its compounds (ZrI_4 , CsI) are volatile and fuel pellets contain many

cracks and spaces through which iodine may be rapidly transported to the cladding. When reactor power is increased during start-up, iodine is released in substantial quantities from the UO_2 pellet [72]. This is believed to cause crack propagation in the cladding when combined with stresses imposed on the cladding by the fuel pellet, a phenomenon known as pellet-cladding interaction (PCI). Upper limits on power ramping and holding times have therefore been established by fuel suppliers to mitigate potential PCI failures [73]. While these restrictions have reduced or prevented the incidence of PCI failures, they also impose costs on the operator due to longer ramping periods. This also restricts the ability of the nuclear reactor to load-follow grid demand. Cladding/fuel materials resistant to PCI failure are therefore of great interest in the nuclear power industry, promoting research into solutions such as cladding liners and doped fuel pellets [74, 75].

Iodine is an oxidising agent, which, under standard conditions, will oxidise Zr metal to produce ZrI_4 . However, oxygen is also present in the internal fuel pin environment, both from the native ZrO_2 layer on the cladding, and the evolution of oxygen from the fuel pellet during burnup. Liberated oxygen will compete with iodine in the oxidation of the Zr metal, but whereas iodine promotes crack growth under stress, oxygen provides a more protective effect, self-limiting its diffusion into the metal [31, 76]. Furthermore, oxygen is a more powerful oxidising agent than iodine, reacting together to produce I_2O_5 . For these reasons, the internal oxide layer of the cladding is often considered a barrier to the ingress of iodine into the Zr metal.

Unlike oxygen and hydrogen, which readily diffuse into Zr metal to occupy interstitial sites, iodine atoms have been predicted in atomistic studies to have very high energy barriers to bulk interstitial diffusion [77–79]. This is due to the relatively large radius of the iodine atom, which imposes large local strains when penetrating the Zr lattice. This suggests that iodine will instead be transported towards crack tips via grain boundaries. Indeed, intergranular cracking has been observed in PCI failures, but only for a few hundred nm before a more rapid transgranular crack propagation [65]. Conversely, no atomic scale studies of iodine in ZrO_2 were found in the literature.

ZrO_2 grown thermally on Zr metal exists mainly in either the monoclinic or tetragonal phase

[2, 48]. We can expect the internal ZrO_2 layer of the cladding to be mostly monoclinic in early life, with the stress-stabilised tetragonal phase appearing near the oxide/metal interface due to cohesive strains resulting from the lattice mismatch. With increasing burnup however, it is expected that more tetragonal and possibly even the cubic phase of ZrO_2 forms due to vacancy formation and residual stresses in the lattice from radiation damage [26]. Amorphisation due to radiation damage has also been observed in the cubic phase from Cs^+ implantation [25]. In this study however, while defect energies for the cubic phase are reported, we focus our analysis on monoclinic and tetragonal ZrO_2 phases, partly due to difficulties predicting the behaviour of the pure high-temperature cubic phase using energies calculated from a static energy technique.

The effectiveness of the oxide layer as a barrier to iodine is debated, with one study presuming that the oxide is bypassed entirely by iodine due to fracturing, leaving the Zr metal underneath exposed [77]. The outermost part of the oxide, which is porous, exhibits networks of interconnected grain boundary diffusion pathways towards the oxide/metal interface which are certainly wide enough (1-3 nm) to allow iodine transport [80]. The oxygen-saturated Zr at the oxide/metal interface is not, however, taken into account, and it is expected that this will influence the corrosion mechanism due to iodine-oxygen competition: even the much smaller hydrogen atom has its rate of diffusion into the metal reduced by the presence of oxygen, as shown in both computational [81] and experimental hydrogen pick-up studies [82]. This means that some barrier to iodine ingress must already exist near the oxide/metal interface. The varying levels of oxygen across the oxide layer itself also have an effect on defect behaviour, and will therefore influence the initiation mechanisms behind PCI failures. Thus here, we predict iodine incorporation energies and defect equilibria in ZrO_2 as a function of oxygen pressure through Brouwer diagrams, in order to predict the resulting iodine defect response.

6.1.1 Iodine stress-corrosion cracking

Iodine SCC is a phenomenon that has affected LWRs for decades.

6.1.2 Pellet-cladding interaction

Pellet-cladding interaction refers to the interaction between the fuel and the cladding at higher burnups where the gas gap has been closed by the swelling of the fuel pellets. PCI has both a mechanical and a chemical component, sometimes referred to specifically as pellet cladding mechanical interaction (PCMI) and pellet cladding chemical interaction (PCCI) respectively.

6.1.3 Oxygen competition

Oxygen and iodine compete for anion sites in ZrO_2 .

6.2 Methodology

6.2.1 Computational details

Calculations were performed using the CASTEP 8.0 density functional theory (DFT) based code [57]. Ultra-soft pseudo-potentials with a cut-off energy of 600 eV were employed. The Perdew, Burke and Ernzerhof (PBE) [58] parameterisation of the generalised gradient approximation (GGA) was used to describe the exchange correlation functional. A Monkhorst-Pack sampling scheme [59] was used for Brillouin zone integration, with a minimum k -point separation of 0.09 \AA^{-1} . The Pulay method for density mixing [60] was used to improve simulation convergence.

The electronic energy convergence criterion was set to $1 \times 10^{-6} \text{ eV}$ and the maximum force between atoms limited to $1 \times 10^{-2} \text{ eV \AA}^{-1}$. A gradient-descent geometry optimisation task was run on the cell until consecutive iterations differed in energy and atomic displacement by less than $1 \times 10^{-5} \text{ eV}$ and $5 \times 10^{-4} \text{ \AA}$ respectively.

6.2.2 Incorporation energies

The inner oxide of the fuel cladding will be highly defective due to radiation damage, resulting in a high concentration of pre-existing intrinsic defect sites relative to the concentration of iodine. We therefore consider the energy of iodine incorporation on to these existing defect sites. The energies to incorporate iodine at interstitial and substitutional sites in ZrO_2 were calculated from the set of defective and perfect supercell DFT energies. Incorporation energies were established to place iodine into vacancy sites of different charge to generate defects from I_O^\times to $\text{I}_\text{O}^{\bullet\bullet}$, and $\text{I}_{\text{Zr}}^\times$ to $\text{I}_{\text{Zr}}^{\prime\prime\prime}$. I was also incorporated onto the interstitial site.

The incorporation energy equation uses $\frac{1}{2}\text{I}_2$ as the reference state of iodine:

$$E_{\text{inc}}(\text{I}_i^\times) = E_{\text{DFT}}(\text{I}_i^\times) - (E_{\text{DFT}}(\text{ZrO}_2) + \frac{1}{2}\mu_{\text{I}_2}) \quad (6.1)$$

where $E_{\text{inc}}(\text{I}_i^\times)$ is the incorporation energy of a neutral iodine interstitial, $E_{\text{DFT}}(\text{I}_i^\times)$ is the energy of a neutral iodine interstitial, $E_{\text{DFT}}(\text{ZrO}_2)$ is the energy of a non-defective ZrO_2 supercell and μ_{I_2} is the chemical potential of an I_2 molecule, taken from a single point DFT calculation of the I_2 dimer. Similarly, for a substitutional defect:

$$E_{\text{inc}}(\text{I}_\text{O}^n) = E_{\text{DFT}}(\text{I}_\text{O}^n) - (E_{\text{DFT}}(\text{V}_\text{O}^n) + \frac{1}{2}\mu_{\text{I}_2}) \quad (6.2)$$

where I_O^n is an iodine substitutional defect at an oxygen site of charge n and V_O^n is the corresponding oxygen vacancy.

6.2.3 Defect Equilibrium Response to Oxygen Partial Pressure

Brouwer diagrams, also known as Kröger-Vink diagrams, were produced using a method outlined by Murphy et al. [40] to determine defect concentrations as a function of oxygen partial pressure. We start from the statement that the chemical potential of ZrO_2 is equivalent to the

sum of the chemical potentials μ of its constituent species, Zr and O:

$$\mu_{\text{ZrO}_2(s)} = \mu_{\text{Zr}}(p_{\text{O}_2}, T) + \mu_{\text{O}_2}(p_{\text{O}_2}, T) \quad (6.3)$$

where T denotes temperature and p_{O_2} denotes oxygen partial pressure. The chemical potential of ZrO_2 in the solid state is assumed to have negligible dependence on T and p_{O_2} relative to μ_{Zr} and μ_{O_2} . Energies can be obtained for bulk ZrO_2 and Zr, but the ground state of oxygen is not correctly reproduced in DFT [41, 42]. Instead, we use the approach of Finnis et al. [43] to infer the oxygen chemical potential from standard state values. We can use the experimental Gibbs free energy to produce an equation where μ_{O_2} is the only unknown:

$$\Delta G_{f, \text{ZrO}_2}^{\ominus} = \mu_{\text{ZrO}_2(s)} - (\mu_{\text{Zr}(s)} + \mu_{\text{O}_2}^{\ominus}) \quad (6.4)$$

where $\Delta G_{f, \text{ZrO}_2}^{\ominus}$ is the experimental Gibbs energy at standard temperature and pressure and $\mu_{\text{O}_2}^{\ominus}$ is the oxygen chemical potential under the same conditions. The values of $\mu_{\text{ZrO}_2(s)}$ and $\mu_{\text{Zr}(s)}$ are calculated from the DFT energies. Once $\mu_{\text{O}_2}^{\ominus}$ is calculated, we can generalise the chemical potential of oxygen for any value of T and p_{O_2} by appending an ideal gas relationship $\Delta\mu(T)$ and a Boltzmann distribution:

$$\mu_{\text{O}_2}(p_{\text{O}_2}, T) = \mu_{\text{O}_2}^{\ominus} + \Delta\mu(T) + \frac{1}{2} k_B \log\left(\frac{p_{\text{O}_2}}{p_{\text{O}_2}^{\ominus}}\right) \quad (6.5)$$

Using our generalised formula for μ_{O_2} , we fix the temperature within the range of thermal phase-stabilisation (1500 K for tetragonal ZrO_2) and calculate μ_{O_2} for many different values of p_{O_2} between 10^{-35} and 10^0 atm, corresponding to oxygen deficient and oxygen rich environments, respectively (p_{O_2} in air is approximately 0.2 atm). While the tetragonal phase will be stress-stabilised in practice, thermal-stabilisation in such models has been shown to qualitatively approximate the effect of stress-stabilisation, while allowing a wider range of dopant behaviours to be predicted [44]. Equilibrium defect concentrations are then calculated at each μ_{O_2} and plotted against p_{O_2} to produce a Brouwer diagram. Brouwer diagrams at extrinsic defect

concentrations of 10^{-5} and 10^{-3} parts/fu (i.e. parts per ZrO_2 formula unit) were generated to examine low and high dopant concentrations, respectively. These two concentrations were examined because the amount of fission products present at a particular point in a fuel pellet depends on macroscopic parameters, including its position in the core and the time since the last shutdown, but also microscopic parameters such as the radial position in the pellet. These two concentrations were selected because 10^{-3} parts/fu is high enough to model an aggregation of iodine (such as at a crack tip), and 10^{-5} parts/fu was found to be the concentration below which iodine did not have a significant effect on defect equilibria.

6.3 Results

6.3.1 Incorporation energies

Interstitial Sites

Neutral iodine incorporation energies in interstitial sites for each phase are reported in Table 6.1. The $2a$ and $2c$ sites in monoclinic ZrO_2 provide the least unfavourable iodine incorporation energy, followed by the $2b$ and $8e$ sites in tetragonal ZrO_2 , although in all cases energies are positive and large, indicating a large energy penalty against interstitial incorporation. The difference in incorporation energies between monoclinic and tetragonal ZrO_2 is approximately 1 eV, whereas the difference between tetragonal and cubic is 3.5 eV, indicating especially unfavourable conditions in cubic ZrO_2 . These differences are likely due to the larger interstitial sites in the lower-temperature phases, as monoclinic ZrO_2 exhibits the least and cubic ZrO_2 the most dense cell.

While the incorporation energies of iodine in the interstitial sites of ZrO_2 are large, for a fixed iodine concentration, they become relevant as the intrinsic defect populations become small, such as at low temperatures relative to the melting point. This is because interstitial sites are always available, whereas at low intrinsic defect concentrations, substitutional sites become

saturated and accommodation at a lattice site first requires the creation of a vacancy defect, which has a formation energy penalty associated with it.

When Brouwer diagrams are generated, iodine will also be considered as a charged species at an interstitial site. This includes I^+ and I^- , where I^+ is a smaller ion that is more easily accommodated at an interstitial site.

Oxygen Sites

Table 6.2 reports incorporation energies of iodine at various oxygen sites. In each phase, the lowest incorporation energy was that for accommodation at a vacant oxygen site such that iodine is in the 1- oxidation state, resulting in the overall defect I_O^\bullet . This anionic behaviour is expected from a halogen atom in a highly reducing site as it promotes the filling of the p shell.

Zirconium Sites

Incorporation energies of iodine on zirconium sites are reported in Table 6.3. The incorporation energy decreases as the charge of the defect decreases from -4 to 0 (i.e. nominally from I^0 to I^{4+}). This is due to the decrease in the size of the iodine species with increasing positive charge, fitting better into the small Zr^{4+} cation site. This alone does not guarantee the emergence of uncharged iodine defects (I^{4+}) on zirconium sites when all energy terms are considered. In particular, there is also an energy penalty incurred in the change in charge of iodine. A Mulliken population analysis revealed a charge localised on the iodine of +2.31 at the I_{Zr}^\times defect, and a +0.86 charge on the I_{Zr}''' defect, with the remaining charge accommodated by other ions in the lattice.

6.3.2 Temperature dependence

To examine the temperature dependence of the defect equilibria, the concentration of dopant iodine was held constant while temperature was changed.

Table 6.1: Incorporation energies of neutral iodine interstitials in non-defective supercells.

| Structure | Site | Incorporation of I_i^\times (eV) |
|------------|-------|---|
| Monoclinic | $2a$ | 8.55 |
| | $2b$ | 10.81 |
| | $2c$ | 8.79 |
| | $2d$ | 10.94 |
| Tetragonal | $2b$ | 9.49 |
| | $8e$ | 9.53 |
| Cubic | $24d$ | 13.02 |
| | $4b$ | 13.08 |

Table 6.2: Incorporation energies of iodine in oxygen sites of the monoclinic, tetragonal, and cubic ZrO_2 phases.

| Structure | Incorporation energy (eV) | | |
|-----------------------|-----------------------------|---------------------------|----------------------------|
| | $\text{I}_\text{O}^\bullet$ | I_O° | I_O^\times |
| Monoclinic (3 co-ord) | 4.54 | 2.90 | 3.67 |
| Monoclinic (4 co-ord) | 5.63 | 3.77 | 4.87 |
| Tetragonal | 6.19 | 4.02 | 4.44 |
| Cubic | 8.37 | 5.74 | 6.66 |

Table 6.3: Incorporation energies of iodine in zirconium sites of ZrO_2 .

| Structure | Incorporation energy (eV) | | | | |
|------------|------------------------------------|------------------------------------|------------------------------------|------------------------------------|---------------------------------|
| | $\text{I}_{\text{Zr}}^{\text{''}}$ | $\text{I}_{\text{Zr}}^{\text{''}}$ | $\text{I}_{\text{Zr}}^{\text{''}}$ | $\text{I}_{\text{Zr}}^{\text{''}}$ | $\text{I}_{\text{Zr}}^{\times}$ |
| Monoclinic | 6.78 | 3.65 | 0.89 | -2.84 | -5.08 |
| Tetragonal | 7.58 | 3.64 | 1.69 | -2.13 | -4.57 |
| Cubic | 9.70 | 6.81 | 3.01 | 0.38 | -3.14 |

6.3.3 Dopant concentration dependence

To examine the dependence of the defect equilibria on iodine dopant concentration, the temperature was held constant while iodine concentration was changed.

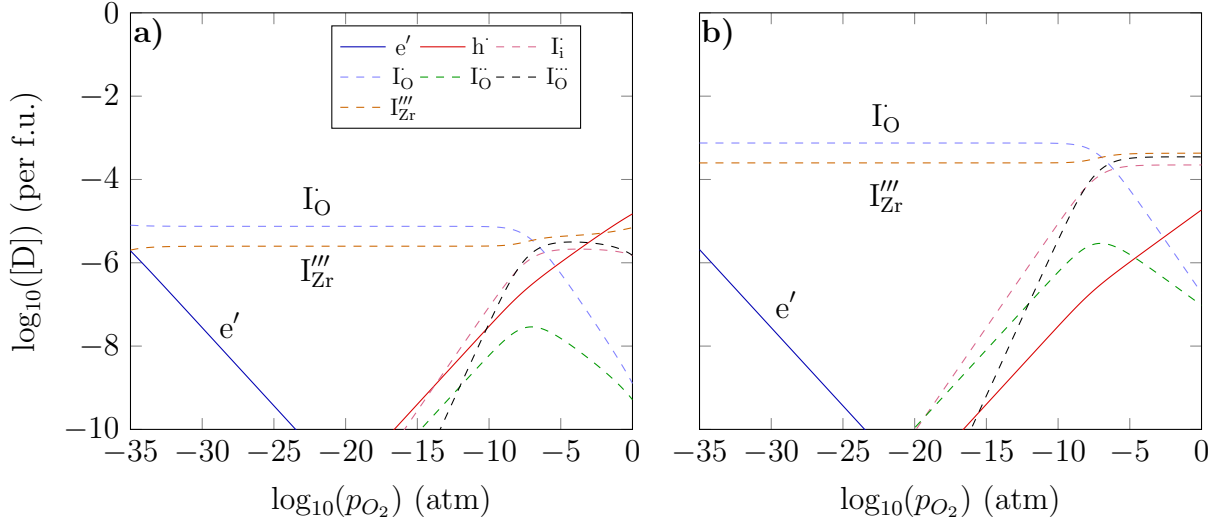


Figure 6.1: Monoclinic phase Brouwer diagrams of point defects at iodine concentrations of a) 10^{-5} and b) 10^{-3} , at a temperature of 650 K.

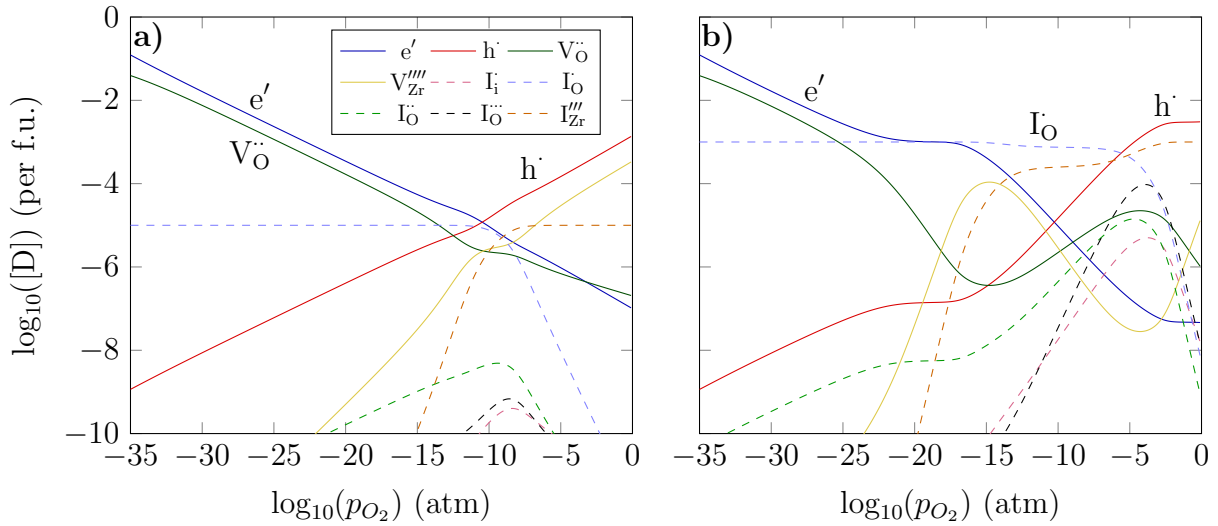


Figure 6.2: Tetragonal phase Brouwer diagrams of point defects at iodine concentrations of a) 10^{-5} and b) 10^{-3} , at a temperature of 1500 K.

6.3.4 Brouwer Diagrams

Monoclinic Phase

Brouwer diagrams associated with the monoclinic phase, at 650 K, at which this ZrO_2 phase is stable, are shown in Figure 6.1. At 650 K, this phase exhibits a relatively low concentration of intrinsic defects; concentrations of $\text{V}_{\text{O}}^{\bullet\bullet}$ and $\text{V}_{\text{Zr}}^{\bullet\bullet\bullet}$ remained below 10^{-10} parts/fu across the majority of oxygen pressures at both iodine concentrations and do not appear in the diagrams. At lower iodine concentrations, the intrinsic electronic defects, e' and h^\bullet , were more significant, with h^\bullet defects being a major fraction of the total defect population near stoichiometry (i.e. at an oxygen pressure of approximately $10^{-7.5}$ atm).

Between oxygen pressures of 10^{-35} and 10^{-10} atm, the dominant defects were $\text{I}_{\text{O}}^\bullet$ charge-compensated by $\text{I}_{\text{Zr}}^{\bullet\bullet\bullet}$. Above an oxygen pressure of 10^{-10} atm, a combination of $\text{I}_{\text{i}}^\bullet$, $\text{I}_{\text{Zr}}^{\bullet\bullet\bullet}$ and $\text{I}_{\text{O}}^{\bullet\bullet\bullet}$ defects were dominant. This demonstrates that iodine will adopt a +1 oxidation state in order to facilitate iodine incorporation into the lattice. The effective ionic radius of I^- is 2.20 Å in VI-fold coordination, compared to 1.38 Å for O^{2-} in IV-fold coordination, as is the case in ZrO_2 [3]. Iodine with a higher positive charge state will have a smaller ionic radius, and thus impose less strain on the lattice (and therefore a smaller energy penalty) in each defect configuration, including substitution on a Zr site. At the highest oxygen pressures, the Brouwer diagrams show that oxidation of iodine, substituted at an oxygen site, to the +1 oxidation state (i.e. $\text{I}_{\text{O}}^{\bullet\bullet\bullet}$) becomes a necessary charge compensating defect. This is because the energy penalty to form hole defects in this broad band insulator is too great, as is the formation of other positive charge defects such as $\text{Zr}_{\text{i}}^{\bullet\bullet\bullet}$. This may translate to iodine out-competing oxygen for oxygen sites in monoclinic ZrO_2 , with higher oxygen pressures providing very little in terms of a barrier effect.

Tetragonal Phase

Brouwer diagrams for the tetragonal phase are shown in Figure 6.2. As these diagrams were generated at a temperature of 1500 K (at which the tetragonal phase becomes stable), intrinsic

defect concentrations were significantly higher than in the monoclinic diagrams for all oxygen pressures (though trends remained the same). Intrinsic defects e' , h^\bullet , $V_O^{\bullet\bullet}$ and $V_{Zr}^{\bullet\bullet\bullet}$ were dominant across most oxygen pressures at an iodine concentration of 10^{-5} parts/fu. Only around stoichiometry do extrinsic defect concentrations approach intrinsic values (which as mentioned earlier is why this concentration of iodine was chosen). Across all oxygen pressures, I_O^\bullet and $I_{Zr}^{\bullet\bullet\bullet}$ are the major iodine defects. Between 10^{-15} and 10^{-5} atm, Figure 6.2 illustrates that the major iodine defect swaps from I_O^\bullet to $I_{Zr}^{\bullet\bullet\bullet}$.

When the iodine concentration was increased to 10^{-3} parts/fu, a significant change in defect equilibria was predicted. The oxygen pressure at stoichiometry increased from 10^{-10} to $10^{-6.5}$ atm (for monoclinic ZrO_2 , it remained at $10^{-7.5}$ atm regardless of iodine concentration). Nevertheless, I_O^\bullet and $I_{Zr}^{\bullet\bullet\bullet}$ remain the dominant defect pair between oxygen pressures of 10^{-15} and 10^{-5} atm (as they are at the lower iodine concentration). However, I_O^\bullet and $I_{Zr}^{\bullet\bullet\bullet}$ became higher concentration defects than both intrinsic $V_O^{\bullet\bullet}$ and $V_{Zr}^{\bullet\bullet\bullet}$ defects. We also observe that Zr vacancies no longer serve as the main negative charge-compensation defect near stoichiometry, leaving $I_{Zr}^{\bullet\bullet\bullet}$ as the most energetically favourable negatively-charged defect.

Unlike in the Brouwer diagrams for the monoclinic phase, for the tetragonal phase, the concentration of iodine substitutional defects on oxygen sites decreases more steeply at high oxygen pressures, peaking near stoichiometry. $I_O^{\bullet\bullet\bullet}$ in particular, which was the dominant defect at high oxygen pressures in monoclinic ZrO_2 , becomes insignificant under the same conditions in the tetragonal phase, with iodine confined to Zr sites. This behaviour is indicative of a ‘barrier’ effect against iodine at high oxygen partial pressures, with oxygen out-competing iodine for oxygen sites. Given that the inner oxide is likely to have a higher tetragonal phase fraction than the external oxide, due to the incorporation of fission products, this result could help to explain why there appears to be an oxygen effect on PCI-related SCC of zirconium alloys [83].

Another effect considered was the space charge of the system. Electrons have a higher rate of diffusion than oxygen vacancies in ZrO_2 , leading to a build-up of oxygen vacancies near the metal-oxide interface as corrosion progresses [84]. This results in an overall positive charge (since the dominant oxygen vacancy is $V_O^{\bullet\bullet}$ referred to as a space charge. When included

in our Brouwer diagrams, this space charge had a negligible effect on the concentration or charge state of iodine up to a charge of 10^{-1} holes per f.u. ZrO_2 . This corresponds to a high concentration of oxygen vacancies relative to the equilibrium concentration, predicting that a significant deviation from the equilibrium is not expected near the metal oxide interface as a result of a positive space charge.

6.4 Summary

Iodine exhibits lower incorporation energies when occupying defects in monoclinic ZrO_2 than in the tetragonal phase. However, as monoclinic is the low-temperature phase, intrinsic defect concentrations will also be low, thereby requiring additional energy input to produce vacancies when the concentration of iodine is much larger than that of the intrinsic defects. This leads to relatively large concentrations of iodine interstitial defects predicted in the monoclinic Brouwer diagrams, as interstitial sites are always available in the lattice.

Defects involving iodine in the +1 oxidation state are present in significant concentrations, especially in monoclinic ZrO_2 , indicating that filling of the p electronic sub-shell is not always energetically favourable compared to forming the smaller iodine ionic radius developed through oxidation.

The competition between iodine and oxygen for anion sites in ZrO_2 is phase and oxygen pressure dependent. At high oxygen pressures in monoclinic ZrO_2 , iodine in the +1 oxidation state is predicted to occupy oxygen sites and remains the dominant defect. In tetragonal ZrO_2 at high oxygen pressures, however, the concentration of iodine defects on anion sites decreases steeply, indicating a preference for iodine accommodated at zirconium cation sites. This is indicative of a barrier effect in the tetragonal phase with oxygen out-competing iodine for anion sites.

Chapter 7

Radioparagenesis of fission products in tetragonal ZrO_2

7.1 Introduction

Stress-corrosion cracking (SCC) in nuclear fuel pins is an issue related to early loss of structural integrity of fuel assemblies in light water reactors (LWRs). In particular, the phenomenon of pellet-cladding interaction (PCI) in combination with SCC can lead to failures where the cladding is breached, exposing fuel to the coolant [27].

Nuclear fuel claddings have unique materials challenges owing to the highly active environment in which they operate and the creation of unstable isotopes. Corrosive species in the pin such as iodine, produced directly as a result of uranium fission are known to play a role in SCC [66, 85, 86]. However, iodine nuclei produced from fission are unstable. Fission of uranium produces iodine precursors, mainly unstable isotopes of tellurium. Both iodine and tellurium are relatively common fission products, with combined independent yields from thermal fission of U_{235} above 5% [5, 67–70, 87]. In addition, xenon and caesium are also common fission products, as shown in Figure 7.1, with fission product masses firmly within the heavy nuclide peak of uranium and plutonium fission product distribution curves.

Previous work on defect equilibria in ZrO_2 considered the internal oxide layer's effectiveness as a barrier to iodine [88]. It was found that the tetragonal phase of ZrO_2 is a better barrier to iodine ingress than monoclinic ZrO_2 , especially at higher oxygen partial pressures. It is also established that tetragonal ZrO_2 will always be present on the inner surface of the cladding in significant quantities because it is self-stabilised by the stresses imposed as the oxide grows into the zirconium metal, in addition to compressive residual stresses induced by radiation damage [31]. The iodine defect study, however, only informs us about one part of the SCC process. For a more holistic understanding, the life cycle of the iodine must also be taken into account.

Nuclei produced during fission are typically neutron-rich, resulting in decay modes such as β - or neutron emission. In the case of tellurium nuclei, most decay into iodine, which then decays into xenon with different half-lives depending on the isotope. Several of these isotopes' fission yield and decay data are shown in Table 7.2. The decay chain continues with xenon nuclei decaying into caesium, many isotopes of which have half lives measured in years. At this point, conventional power reactor fuel is retired long before a significant proportion of the caesium decays into barium. For this reason we only consider the elements tellurium through caesium in this study.

The majority of thermal fission events occur in the outer rim of a fuel pellet. Given a fission product penetration depth of up to $8\text{ }\mu\text{m}$ in ZrO_2 [71], a large proportion of fission products implant within the oxide. It has also been observed in PCI failures that there is a time delay on the order of 10 minutes between the power ramping of the reactor and the subsequent breach of the cladding [89–91]. This time delay is in line with the half-lives of many Te and I isotopes (Table 7.2) such that significant proportions of these isotopes will decay during this time delay, hinting that these phenomena could be related.

With each nuclear decay comes a change in the chemical and therefore physical behaviour of the atom with its immediate environment. For example, an iodine dopant in ZrO_2 may decay into xenon, which may then have a significantly different thermodynamic equilibrium site preference from the one it inherited. Determining the behaviour of each of these elements in the oxide

layer may provide information about the initiation of SCC in fuel cladding. We have therefore adopted a quantum-mechanical calculation approach to model the behaviour of the decay chain elements tellurium through caesium within tetragonal phase zirconia.

7.2 Methodology

7.2.1 Computational Parameters

Calculations were performed using the CASTEP 8.0 density functional theory (DFT) based code [57]. Ultra-soft pseudo-potentials with a cut-off energy of 600 eV were employed. The Perdew, Burke and Ernzerhof (PBE) [58] parameterisation of the generalised gradient approximation (GGA) was used to describe the exchange correlation functional. A Monkhorst-Pack sampling scheme [59] was used for Brillouin zone integration, with a minimum k -point separation of 0.09 Å⁻¹. The Pulay method for density mixing [60] was used to improve simulation convergence.

The electronic energy convergence criterion was set to 1×10^{-6} eV and the maximum force between atoms limited to 1×10^{-2} eV Å⁻¹. A gradient-descent geometry optimisation task was run on the cell until consecutive iterations differed in energy and atomic displacement by less than 1×10^{-5} eV and 5×10^{-4} Å respectively.

Using these convergence criteria, non-defective supercells of tetragonal (3x3x2 unit cells) ZrO₂ were relaxed under constant pressure. The resulting structure was used as the starting point to which defects were introduced, and subsequently relaxed again, this time under constant volume conditions to simulate low defect concentrations [40,92]. The supercell was constructed such that its dimensions were as close to a cube as possible in order to minimise directional defect self-interaction across the periodic boundaries.

7.2.2 Defect Volumes

Defect volumes were calculated by completely relaxing an unconstrained, defective supercell using the geometry optimisation task in CASTEP. This allows the defective supercell to alter its volume in order to minimise the total energy of the system, at which point this ‘optimal’ supercell volume is recorded. The non-defective supercell volume, calculated in the same way, is then subtracted from the defective supercell volume to give the individual defect volume.

7.2.3 Defect Equilibrium Response to Oxygen Partial Pressure

Brouwer diagrams, also known as Kröger-Vink diagrams, were produced using a method outlined by Murphy et al. [93] to determine defect concentrations as a function of oxygen partial pressure. We start from the statement that the chemical potential of ZrO_2 is equivalent to the sum of the chemical potentials μ of its constituent species, Zr and O:

$$\mu_{\text{ZrO}_2(s)} = \mu_{\text{Zr}}(p_{\text{O}_2}, T) + \mu_{\text{O}_2}(p_{\text{O}_2}, T) \quad (7.1)$$

where T denotes temperature and p_{O_2} denotes oxygen partial pressure. The chemical potential of ZrO_2 in the solid state is assumed to have negligible dependence on T and p_{O_2} relative to μ_{Zr} and μ_{O_2} . Energies can be obtained for bulk ZrO_2 and Zr, but the ground state of oxygen is not correctly reproduced in DFT [41, 42]. Instead, we use the approach of Finnis et al. [43] to infer the oxygen chemical potential from standard state values. We can use the experimental Gibbs free energy to produce an equation where μ_{O_2} is the only unknown:

$$\Delta G_{f, \text{ZrO}_2}^{\ominus} = \mu_{\text{ZrO}_2(s)} - (\mu_{\text{Zr}(s)} + \mu_{\text{O}_2}^{\ominus}) \quad (7.2)$$

where $\Delta G_{f, \text{ZrO}_2}^{\ominus}$ is the experimental Gibbs energy at standard temperature and pressure and $\mu_{\text{O}_2}^{\ominus}$ is the oxygen chemical potential under the same conditions. The values of $\mu_{\text{ZrO}_2(s)}$ and $\mu_{\text{Zr}(s)}$ are calculated from the DFT energies. Once $\mu_{\text{O}_2}^{\ominus}$ is calculated, we can generalise the

chemical potential of oxygen for any value of T and p_{O_2} by appending an ideal gas relationship $\Delta\mu(T)$ and a Boltzmann distribution:

$$\mu_{O_2}(p_{O_2}, T) = \mu_{O_2}^{\ominus} + \Delta\mu(T) + \frac{1}{2}k_B \log\left(\frac{p_{O_2}}{p_{O_2}^{\ominus}}\right) \quad (7.3)$$

Using our generalised formula for μ_{O_2} , we fix the temperature within the range of thermal phase-stabilisation (1500 K for tetragonal ZrO_2) and calculate μ_{O_2} for many different values of p_{O_2} between 10^{-35} and 10^0 atm, corresponding to oxygen deficient and oxygen rich environments, respectively (p_{O_2} in air is approximately 0.2 atm). While the tetragonal phase will be stress-stabilised in practice, thermal-stabilisation in such models has been shown to qualitatively approximate the effect of stress-stabilisation, while allowing a wider range of dopant behaviours to be predicted [44]. Equilibrium defect concentrations are then calculated at each μ_{O_2} and plotted against p_{O_2} to produce a Brouwer diagram. Brouwer diagrams at extrinsic defect concentrations of 10^{-5} and 10^{-3} parts/fu (i.e. parts per ZrO_2 formula unit) were generated to examine low and high dopant concentrations, respectively. These two concentrations were examined because the amount of fission products present at a particular point in a fuel pellet depends on macroscopic parameters, including its position in the core and the time since the last shutdown, but also microscopic parameters such as the radial position in the pellet.

7.3 Results

7.3.1 Brouwer Diagrams

Tellurium

Brouwer diagrams for tellurium defects are shown in Figure 7.2. At a tellurium defect concentration of 10^{-5} parts per f.u. ZrO_2 , the dominant defect was $Te_O^{\bullet\bullet}$ over the oxygen pressure range of 10^{-28} to 10^{-7} atm. This is mainly charge compensated by intrinsic electronic defects at lower oxygen pressures, and zirconium vacancies at higher oxygen pressures. At higher oxygen

pressures, tellurium preferentially occupies zirconium sites, producing the defect Te_{Zr}''' , this time charge compensated by positive hole defects.

Tellurium on an oxygen site adopts a 0 charge state, which while not obvious (it may be expected to act like oxygen, also a group 6 element), can be reasoned when considering chemical behaviour. Oxygen on its native site will readily adopt a charge state of -2. Tellurium on the other hand, exhibits more metallic behaviour, preferring to get oxidised itself. However, the $\text{V}_{\text{O}}^{\bullet\bullet}$ site is highly reducing, and will counter the tellurium ion's proclivity to oxidise. The overall effect on tellurium in this case is to maintain its original electronic structure. Finally, when the tellurium concentration is increased to 10^{-3} parts/fu, greater occupancy on the zirconium site is predicted above oxygen pressures of 10^{-17} atm, forming the defect Te_{Zr}''' . This corresponds to a tellurium charge state of +1. While we would expect an even more positive charge state for tellurium, in this case it is the dominant negative defect by an order of magnitude and is necessary to charge compensate positive hole and $\text{Te}_{\text{O}}^{\bullet\bullet}$ defects.

In terms of defect volume, $\text{Te}_{\text{O}}^{\bullet\bullet}$ has a slightly positive volume of 2.74 \AA^3 . This is quite large for a positively charged defect ($\text{V}_{\text{O}}^{\bullet\bullet}$ has a defect volume of -40.45 \AA^3), very likely due to the large size of the tellurium atom itself. When tellurium occupies the zirconium site, the resulting Te_{Zr}''' has a defect volume of 59.93 \AA^3 . While this is lower than the defect volume of V_{Zr}''' (88.93 \AA^3)

Iodine

Iodine was previously predicted in Brouwer diagrams (Figure 7.3) to produce the defects $\text{I}_{\text{O}}^{\bullet}$ and I_{Zr}''' at low and high oxygen pressures respectively. Since the extrinsic defect site is similar for tellurium defects over most oxygen pressures, β -decay of tellurium could have directly produced these iodine defects without requiring a change of site. Thus, $\text{Te}_{\text{O}}^{\bullet\bullet}$ would decay and produce $\text{I}_{\text{O}}^{\bullet}$ with a defect volume of 29.90 \AA^3 , and Te_{Zr}''' would decay and produce I_{Zr}''' with a defect volume of 87.07 \AA^3 . At the oxygen site, this means a defect volume change from 2.74 to 29.90 \AA^3 . This increase is in large part due to the change in charge state from 0 to -1, as the ions are of similar size otherwise.

Similarly at the zirconium site, the defect volume changes from 59.93 to 87.07 Å³. Both of these are relatively large increases in defect volume and will come with an increase in lattice stress in the immediate vicinity of the defect, especially if highly constrained. Of course, this process will take place continuously over time as tellurium atoms decay, with half-lives ranging from seconds to hours depending on the isotope. It is of note however, that PCI failures tend to occur after power ramps with a time delay, even up to an hour after the transient. While not conclusive, this may hint at a mechanism involving decay processes.

Xenon

Brouwer diagrams for xenon defects are shown in Figure 7.4. At a xenon concentration of 10⁻⁵ parts/fu ZrO₂, the dominant xenon defect is Xe^{••}_O at low oxygen pressures, and a combination of Xe^{••}_O, Xe^{'''}_{Zr} and Xe^{'''}_{Zr} at stoichiometry (10⁻⁹ atm) and higher. At a higher xenon concentration of 10⁻³ parts/fu ZrO₂, Xe^{••}_O becomes the dominant defect over a greater oxygen pressure range, from 10⁻³⁰ to 10⁻⁵ atm, with Xe^{'''}_{Zr} also present in high concentrations at oxygen pressures above 10⁻²⁰ atm. As a noble gas, it is expected that xenon in a 0 charge state (Xe^{••}_O and Xe^{'''}_{Zr}) will be prevalent since the full electronic shell provides a stable configuration.

Xe^{••}_O and Xe^{'''}_{Zr} have defect volumes of 9.02 and 115.50 Å³ respectively. Following from the decay of iodine, the defect volume on the oxygen site will fall from 29.90 Å³, while the defect volume on the zirconium site increases from 87.07 Å³. The defect volume reduction on the oxygen site can be attributed to the charge state changing from -1 to 0 (i.e. I[•]_O to Xe^{••}_O), resulting in a smaller defect. The opposite is true for the zirconium site, where the charge state changes from +1 to 0 (I^{'''}_{Zr} to Xe^{'''}_{Zr}).

Caesium

Brouwer diagrams for caesium defects are shown in Figure 7.5. Caesium defects were mostly unaffected by a change in oxygen pressure, with dominant defects only changing from Cs^{••}_O to Cs^{'''}_{Zr} at an oxygen pressure of 10^{-30.5} atm, regardless of the caesium concentration. However,

because additional charge compensation for caesium defects is necessary at higher caesium concentrations, we see an increase in the concentration of $\text{V}_{\text{O}}^{\bullet\bullet}$ to compensate for the negative Cs_{Zr}''' defects.

The defect volumes of $\text{Cs}_{\text{O}}^{\bullet\bullet}$ and Cs_{Zr}''' were 4.38 and 90.37 \AA^3 respectively, less than the Xe defects on the same site. This is consistent with the fact that Cs has a much smaller first ionisation energy than Xe, therefore presenting a smaller energy barrier to reducing it's size on either site to improve lattice fit. Because of this, we do not expect further stresses being imposed on the lattice after Xe decays to Cs. We therefore consider that only Te, I and Xe will be significant in this mechanism, as the only contribution to lattice stresses due to Cs would have occurred through direct implantation after fission.

7.4 Conclusions

As fission products proceed down the decay chain from Te to Xe, the defects they produce in ZrO_2 have progressively larger volumes. The change in defect volume when Te_{Zr}''' decays and produces I_{Zr}''' is +27.14 \AA^3 . This then decays and produces the defect $\text{Xe}_{\text{Zr}}''''$, which leads to an even larger change in defect volume of +28.43 \AA^3 . Similarly, at the oxygen site, $\text{Te}_{\text{O}}^{\bullet\bullet}$ decays to produce $\text{I}_{\text{O}}^{\bullet}$, with a resulting defect volume change of +27.16 \AA^3 . The lattice mismatch of these defects in ZrO_2 will generate stresses and promote crack formation, exposing Zr metal. If enough fission products are implanted simultaneously, the rate of crack formation may become faster than new passivating oxide can be produced, and typical I-SCC mechanisms will take over to failure. This process may be a contributing factor to fuel cladding failures observed after a power ramp, with reported time delays between ramp and failure aligning with the decay rate of Te and I isotopes.

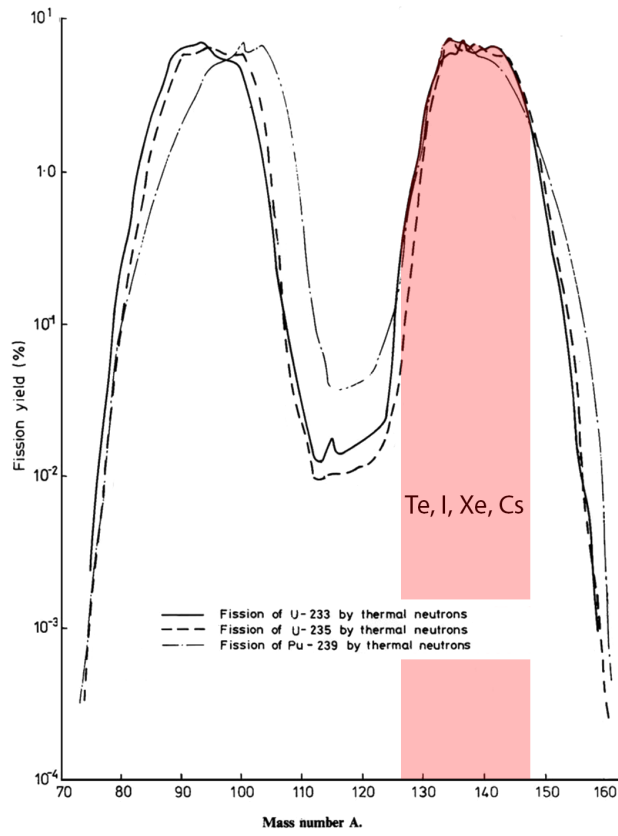


Figure 7.1: Plot of the percentage yield of nuclei with a given mass following a fission event. Range of masses corresponding to isotopes of Te, I, Xe and Cs are highlighted. Adapted from [19].

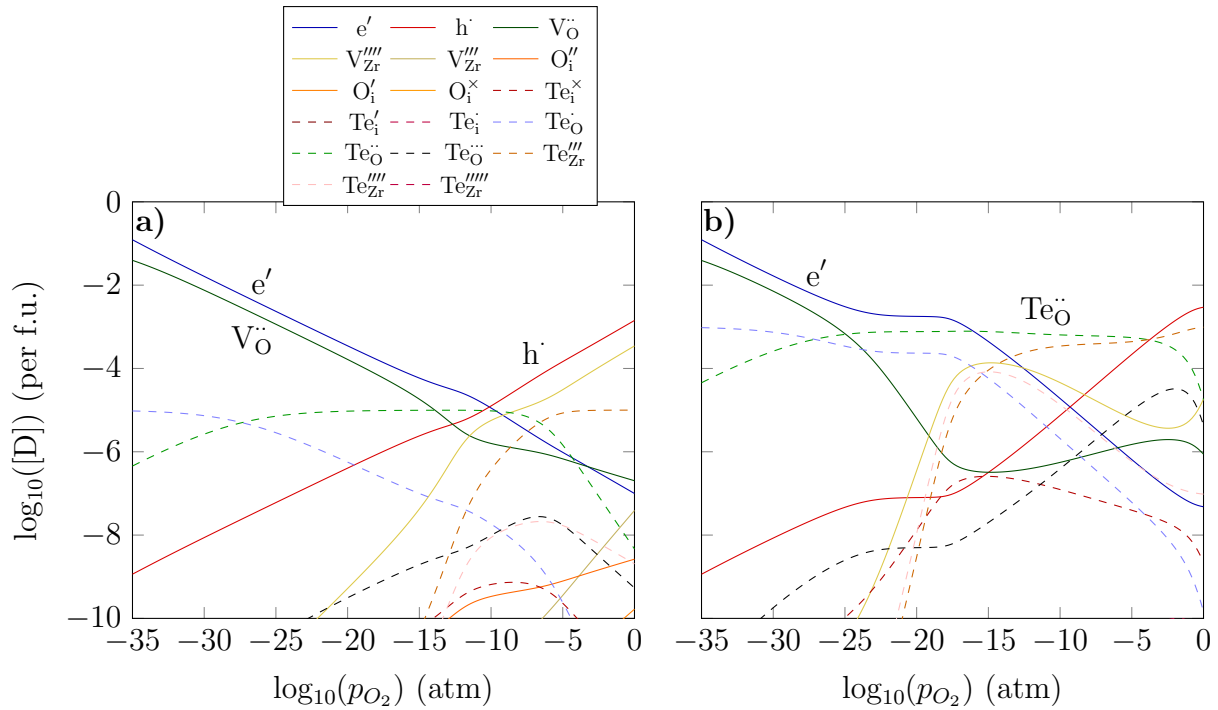


Figure 7.2: Tetragonal phase Brouwer diagrams of point defects at tellurium concentrations of a) 10^{-5} and b) 10^{-3} , at a temperature of 1500 K. Space charge = 0

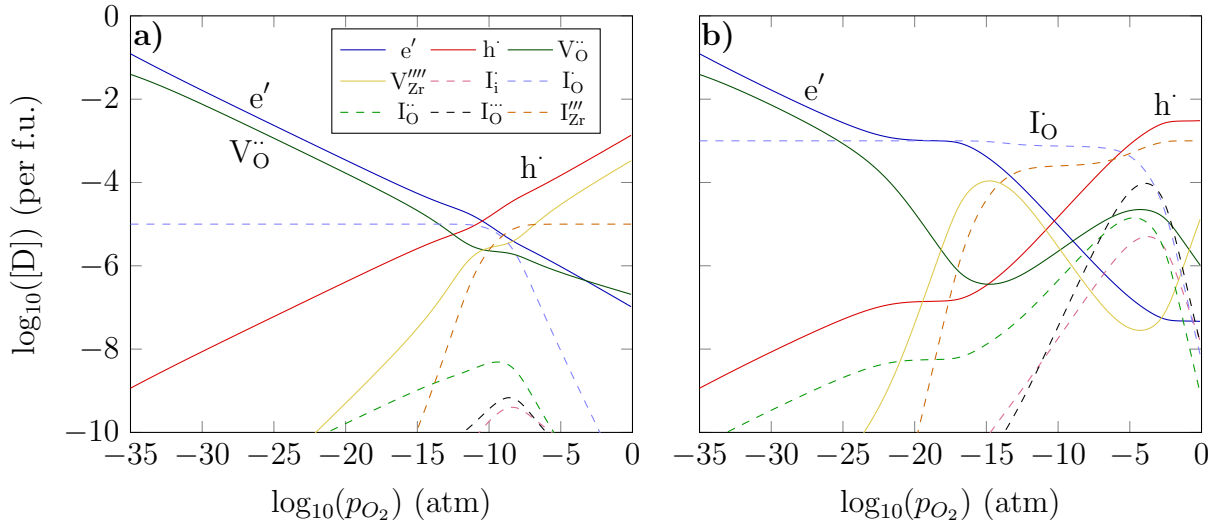


Figure 7.3: Tetragonal phase Brouwer diagrams of point defects at iodine concentrations of a) 10^{-5} and b) 10^{-3} , at a temperature of 1500 K.

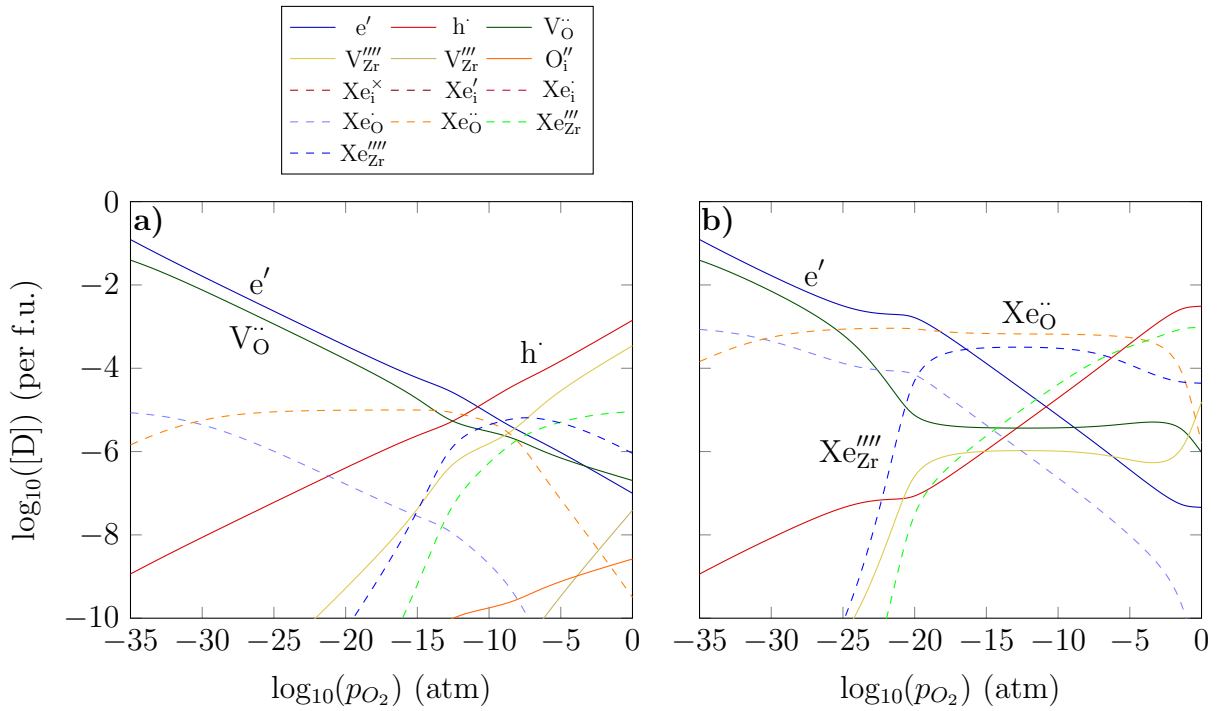


Figure 7.4: Tetragonal phase Brouwer diagrams of point defects at Xenon concentrations of a) 10^{-5} and b) 10^{-3} , at a temperature of 1500 K. Space charge = 0

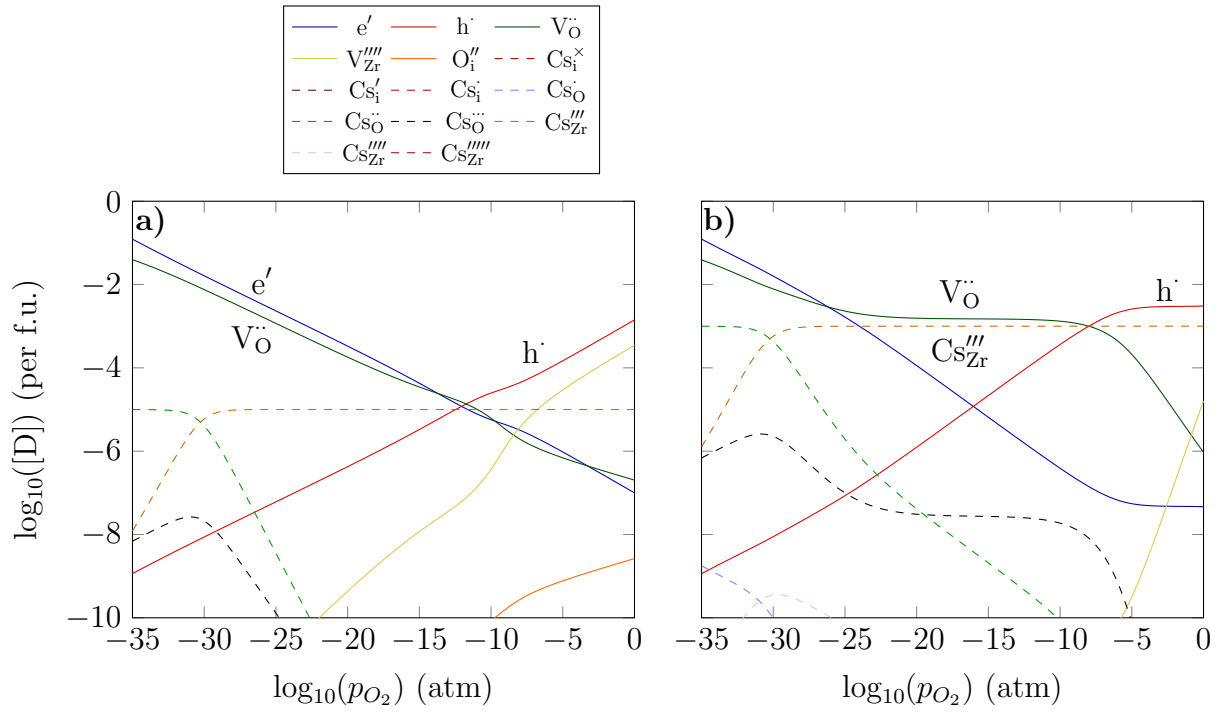


Figure 7.5: Tetragonal phase Brouwer diagrams of point defects at caesium concentrations of a) 10^{-5} and b) 10^{-3} , at a temperature of 1500 K. Space charge = 0

Table 7.1: Defect volumes and formation energies of the dominant defect types in tetragonal ZrO_2 .

| Defect type | Defect volume relative to perfect crystal (\AA^3) | Formation energy at 1500 K (eV) |
|--|--|---------------------------------|
| $\text{V}_{\text{O}}^{\bullet\bullet}$ | -40.45 | -0.92 |
| $\text{V}_{\text{Zr}}^{\prime\prime\prime}$ | 88.93 | 7.04 |
| $\text{Te}_{\text{O}}^{\bullet\bullet\bullet}$ | -18.83 | 1.07 |
| $\text{Te}_{\text{O}}^{\bullet\bullet}$ | 2.74 | 2.24 |
| $\text{Te}_{\text{O}}^{\bullet}$ | 24.61 | 5.10 |
| $\text{Te}_{\text{Zr}}^{\prime\prime\prime}$ | 83.01 | 8.85 |
| $\text{Te}_{\text{Zr}}^{\prime\prime}$ | 59.93 | 5.97 |
| $\text{I}_{\text{O}}^{\bullet\bullet\bullet}$ | -18.59 | -2.68 |
| $\text{I}_{\text{O}}^{\bullet}$ | 29.90 | 0.10 |
| $\text{I}_{\text{Zr}}^{\prime\prime\prime}$ | 87.07 | 4.17 |
| $\text{Xe}_{\text{O}}^{\bullet\bullet}$ | 9.02 | -1.18 |
| $\text{Xe}_{\text{O}}^{\bullet}$ | 32.07 | 1.84 |
| $\text{Xe}_{\text{Zr}}^{\prime\prime\prime}$ | 115.50 | 6.72 |
| $\text{Xe}_{\text{Zr}}^{\prime\prime}$ | 91.65 | 4.97 |
| $\text{Cs}_{\text{O}}^{\bullet\bullet}$ | 4.38 | 4.17 |
| $\text{Cs}_{\text{Zr}}^{\prime\prime\prime}$ | 90.37 | 5.97 |

Table 7.2: Independent fission product yields and half-lives for the major iodine isotopes and precursors in a thermal neutron reactor. Yields from [4,5]. All isotopes undergo single β -decay. Metastable states are included.

| Isotope | Independent Yield (%) | Half-life |
|-------------------|-----------------------|--------------|
| I_{131} | 0.00136 ± 0.00047 | 8.023 d [94] |
| Te_{132} | 1.61 ± 0.37 | 3.180 d [95] |
| I_{132} | 0.017 ± 0.11 | 2.295 h [95] |
| Te_{133} | 3.93 ± 0.15 | 12.5 m [87] |
| I_{133} | 0.153 ± 0.053 | 20.87 h [96] |
| Te_{134} | 6.00 ± 0.47 | 41.8 m [87] |
| I_{134} | 0.900 ± 0.08 | 52.5 m [97] |
| Te_{135} | 3.683 ± 0.56 | 19.0 s [87] |
| I_{135} | 2.550 ± 0.54 | 6.58 h [98] |

7.4.1 Radioparagenesis

The nuclei of fission products immediately after a fission event are typically neutron-rich and unstable. In the case of iodine, the stable isotope is I-127, yet isotopes up to I-143 are produced during fission. This is the true for the fission of all large nuclei, including U-233 (thorium cycle), U-235 (conventional) and Pu-239 (breeder/MOX)

Stress-corrosion cracking (SCC) in nuclear fuel pins is an issue related to early loss of structural integrity of fuel assemblies in light water reactors (LWRs). In particular, the phenomenon of pellet-cladding interaction (PCI) in combination with SCC can lead to failures where the cladding is breached, exposing fuel to the coolant [27].

This study follows previous work on defect equilibria in ZrO_2 to determine the oxide layer's effectiveness as a barrier to iodine [88]. It was found that the tetragonal phase of ZrO_2 is a greater barrier to iodine ingress than monoclinic ZrO_2 as the partial pressure of oxygen is increased. It is also known that tetragonal ZrO_2 will always be present on the inner surface of the cladding in significant quantities because it is self-stabilised by the stresses imposed as the oxide grows into the zirconium metal, in addition to compressive residual stresses induced by radiation damage. The iodine defect study, however, only informs us about one part of the

SCC process. For a more holistic understanding, the life cycle of the iodine must be taken into account as well.

Nuclear fuel claddings have unique materials challenges associated with them owing to the highly active environment and creation of unstable isotopes. Corrosive species in the pin such as iodine can be produced directly as a result of fission of uranium fuel. While it is known that iodine plays a role in SCC, one must also consider that these iodine nuclei are unstable. Fission of uranium will produce iodine precursors, mainly unstable isotopes of tellurium. Both iodine and tellurium are relatively common fission products, with combined independent yields from thermal fission of U_{235} above 5% [4, 5, 67–70].

Nuclei produced during fission are typically neutron-rich, resulting in decay modes such as β – or neutron emission. In the case of tellurium, the vast majority of unstable isotopes will decay into iodine, which then decays into xenon with varying half-lives depending on the isotope. The decay chain continues with xenon nuclei decaying into caesium, many isotopes of which have half-lives measured in years. At this point, fuel is typically retired long before a significant quantity of caesium decays into barium. For this reason we only consider the elements tellurium through caesium in this study. It should also be noted that the majority of thermal fission events occur in the outer rim of the fuel pellet, and a fission product penetration depth of up to 8 μm in ZrO_2 [71] suggests a large degree of fission product implantation within the oxide. With each nuclear decay comes a change in the chemical and therefore physical behaviour of the atom with its immediate environment. For example, an iodine dopant in ZrO_2 may decay into xenon which will then have a significantly different thermodynamic equilibrium site from the one it inherited.

Determining the effect of each of these elements in the oxide layer may provide information about the initiation of SCC in fuel cladding. We have therefore adopted a quantum-mechanical calculation approach to model the behaviour of the decay chain elements tellurium through caesium within tetragonal phase zirconia.

- We propose that crack initiation on the internal surface of the cladding may be in part due to radioparagenesis of fission products

- One mechanism is neutron-rich iodine making its way through the monoclinic ZrO_2 before being stopped by the highly passivating tetragonal ZrO_2 closer to the metal interface.
- The iodine nucleus then decays by beta- particle emission, converting from an iodine to a xenon nucleus.
- This xenon ion quickly fills its valence shell to the noble gas configuration.
- The uncharged xenon atom then imposes a large strain on the surrounding ZrO_2 due to the volume mismatch.
- This strain weakens the monoclinic ZrO_2 , and promotes crack initiation (new surface relieves the strain imposed by the xenon).
- The tetragonal ZrO_2 , now less constrained by the monoclinic layer, expands and becomes less inhibiting to iodine and oxygen ingress.
- If the iodine partial pressure is high enough relative to the oxygen pressure, the ZrO_2 layer will fail to impede iodine corrosive attack on the zirconium metal.

Xenon in a reactor will also eventually decay by beta- emission into caesium, a much more chemically reactive element.

7.4.2 Site preference of fission products

- **Tellurium** is a group 6 element like oxygen, but it displays some metallic behaviour.
- Because of its electronic structure, it may be expected to display preference for the oxygen site in ZrO_2 .
- It's metallic properties and low electronegativity, however, suggest that it may be able to fill a cation site instead, but this would require the creation of oxygen vacancies since it has a lower valence than zirconium.

- **Iodine** was shown in Chapter 4 to adopt either oxygen and zirconium sites under the right conditions
- **Xenon** is a noble gas, but is still able to form compounds with very strong oxidising agents (e.g. XeF₄). It's large size (comparison here) may make it unfavourable in both cation and anion sites, thus imposing a large lattice strain.
- **Caesium** is a group 1 metal. Its second ionisation energy is very large (removing an electron from a full *p* sub-shell), likely making it very unfavourable on a zirconium site, only made worse by its size.

7.5 Methodology

7.5.1 Simulation parameters

Calculations were performed using the CASTEP 8.0 density functional theory (DFT) based code [57]. Ultra-soft pseudo-potentials with a cut-off energy of 600 eV were employed. The Perdew, Burke and Ernzerhof (PBE) [58] parameterisation of the generalised gradient approximation (GGA) was used to describe the exchange correlation functional. A Monkhorst-Pack sampling scheme [59] was used for Brillouin zone integration, with a minimum *k*-point separation of 0.09 Å⁻¹. The Pulay method for density mixing [60] was used to improve simulation convergence.

The electronic energy convergence criterion was set to 1×10^{-6} eV and the maximum force between atoms limited to 1×10^{-2} eV Å⁻¹. A gradient-descent geometry optimisation task was run on the cell until consecutive iterations differed in energy and atomic displacement by less than 1×10^{-5} eV and 5×10^{-4} Å respectively.

- energy per atom convergence
- displacement per atom convergence
- plane-wave cutoff

- k-point spacing
- PBE GGA exchange correlation functional

7.5.2 Brouwer diagram generation

Brouwer diagrams, also known as Kröger-Vink diagrams, were produced using a method outlined by Murphy et al. [40] to determine defect concentrations as a function of oxygen partial pressure. We start from the statement that the chemical potential of ZrO_2 is equivalent to the sum of the chemical potentials μ of its constituent species, Zr and O:

$$\mu_{\text{ZrO}_2(s)} = \mu_{\text{Zr}}(p_{\text{O}_2}, T) + \mu_{\text{O}_2}(p_{\text{O}_2}, T) \quad (7.4)$$

where T denotes temperature and p_{O_2} denotes oxygen partial pressure. The chemical potential of ZrO_2 in the solid state is assumed to have negligible dependence on T and p_{O_2} relative to μ_{Zr} and μ_{O_2} . Energies can be obtained for bulk ZrO_2 and Zr, but the ground state of oxygen is not correctly reproduced in DFT [41, 42]. Instead, we use the approach of Finnis et al. [43] to infer the oxygen chemical potential from standard state values. We can use the experimental Gibbs free energy to produce an equation where μ_{O_2} is the only unknown:

$$\Delta G_{f, \text{ZrO}_2}^{\ominus} = \mu_{\text{ZrO}_2(s)} - (\mu_{\text{Zr}(s)} + \mu_{\text{O}_2}^{\ominus}) \quad (7.5)$$

where $\Delta G_{f, \text{ZrO}_2}^{\ominus}$ is the experimental Gibbs energy at standard temperature and pressure and $\mu_{\text{O}_2}^{\ominus}$ is the oxygen chemical potential under the same conditions. The values of $\mu_{\text{ZrO}_2(s)}$ and $\mu_{\text{Zr}(s)}$ are calculated from the DFT energies. Once $\mu_{\text{O}_2}^{\ominus}$ is calculated, we can generalise the chemical potential of oxygen for any value of T and p_{O_2} by appending an ideal gas relationship $\Delta\mu(T)$ and a Boltzmann distribution:

$$\mu_{\text{O}_2}(p_{\text{O}_2}, T) = \mu_{\text{O}_2}^{\ominus} + \Delta\mu(T) + \frac{1}{2} k_B \log\left(\frac{p_{\text{O}_2}}{p_{\text{O}_2}^{\ominus}}\right) \quad (7.6)$$

Using our generalised formula for μ_{O_2} , we fix the temperature within the range of thermal phase-stabilisation (1500 K for tetragonal ZrO_2) and calculate μ_{O_2} for many different values of p_{O_2} between 10^{-35} and 10^0 atm, corresponding to oxygen deficient and oxygen rich environments, respectively (p_{O_2} in air is approximately 0.2 atm). While the tetragonal phase will be stress-stabilised in practice, thermal-stabilisation in such models has been shown to qualitatively approximate the effect of stress-stabilisation, while allowing a wider range of dopant behaviours to be predicted [44]. Equilibrium defect concentrations are then calculated at each μ_{O_2} and plotted against p_{O_2} to produce a Brouwer diagram. Brouwer diagrams at extrinsic defect concentrations of 10^{-5} and 10^{-3} parts/fu (i.e. parts per ZrO_2 formula unit) were generated to examine low and high dopant concentrations, respectively. These two concentrations were examined because the amount of fission products present at a particular point in a fuel pellet depends on macroscopic parameters, including its position in the core and the time since the last shutdown, but also microscopic parameters such as the radial position in the pellet. These two concentrations were selected because 10^{-3} parts/fu is high enough to model an aggregation of iodine (such as at a crack tip), and 10^{-5} parts/fu was found to be the concentration below which iodine did not have a significant effect on defect equilibria.

- Defect concentration against oxygen partial pressure
- Find Fermi level that leads to charge neutrality

7.5.3 Defect Volumes

- compare constant pressure relaxation of defective to perfect supercell

7.6 Defect equilibria

7.6.1 Tellurium

Filler

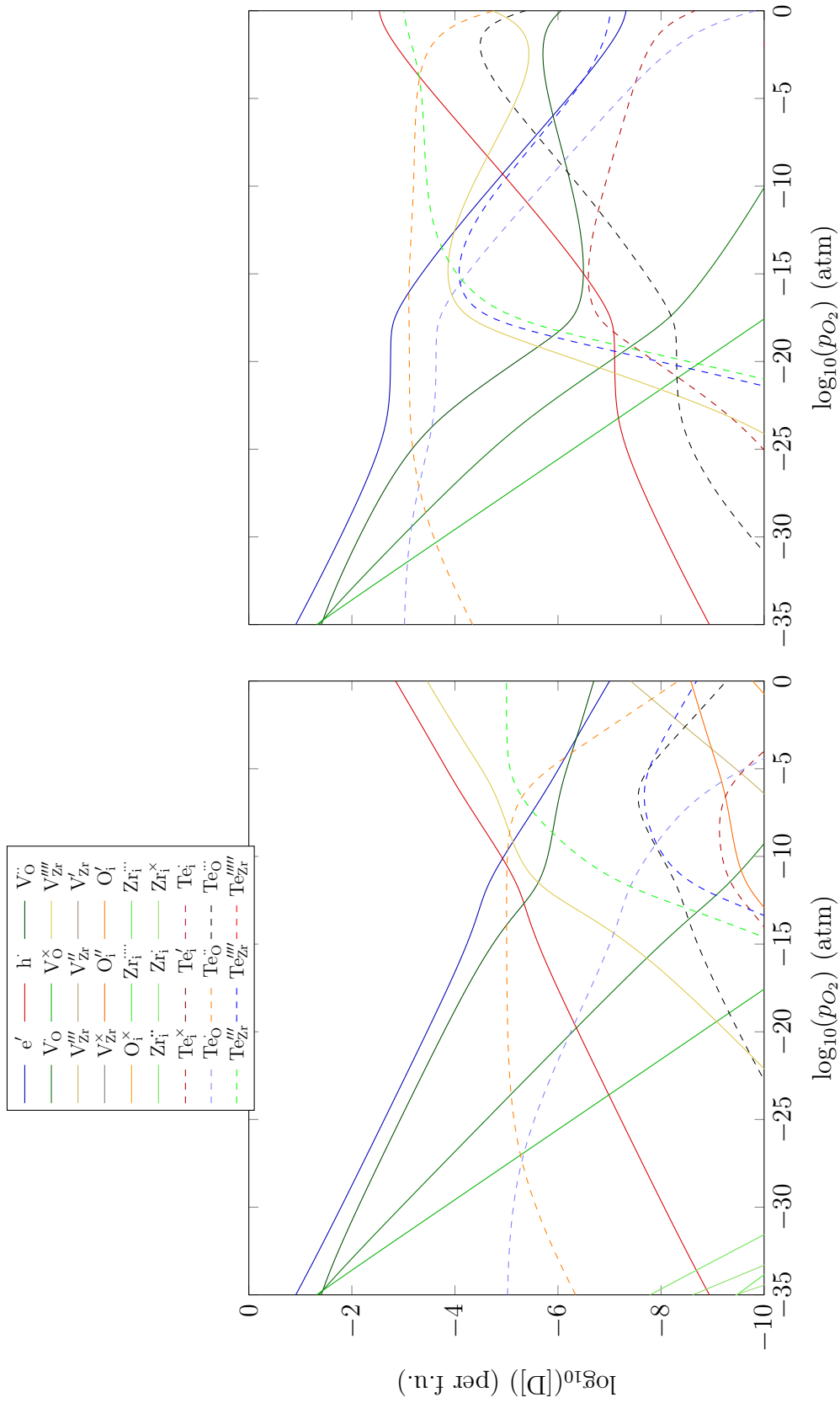


Figure 7.6: Tetragonal phase Brouwer diagrams of point defects at Tellurium concentrations of a) 10^{-5} and b) 10^{-3} , at a temperature of 1500 K. Space charge = 0

7.6.2 Iodine

- Should we just reference the Brouwer diagram for iodine again?

7.6.3 Xenon

- Xenon point defects showed a change in behaviour at high and low oxygen pressures

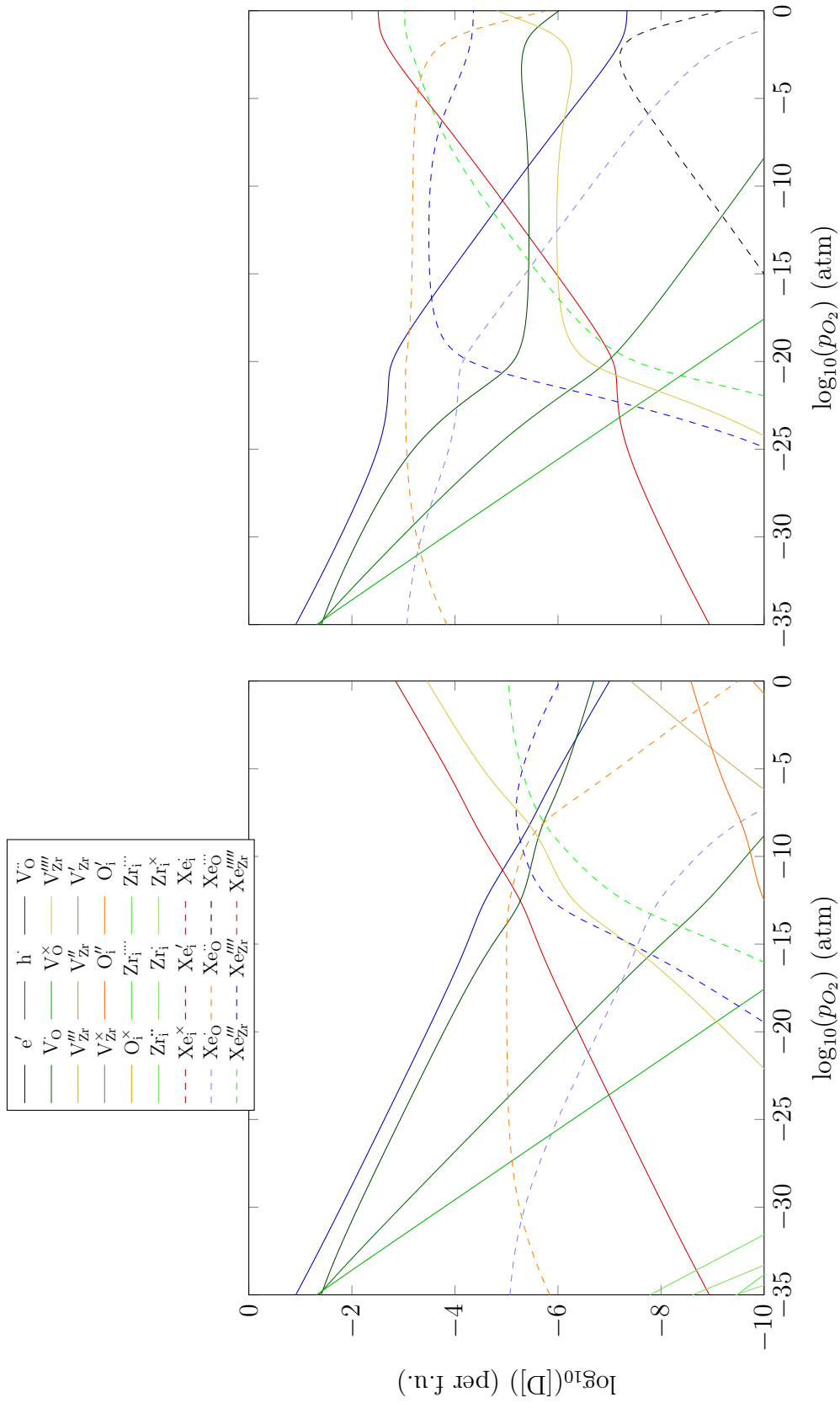


Figure 7.7: Tetragonal phase Brouwer diagrams of point defects at Xenon concentrations of a) 10^{-5} and b) 10^{-3} , at a temperature of 1500 K. Space charge = 0

7.6.4 Caesium

- Cs point defects didn't show much change in behaviour
- Defects behaviour strongly follows single ionisation preference (as expected).

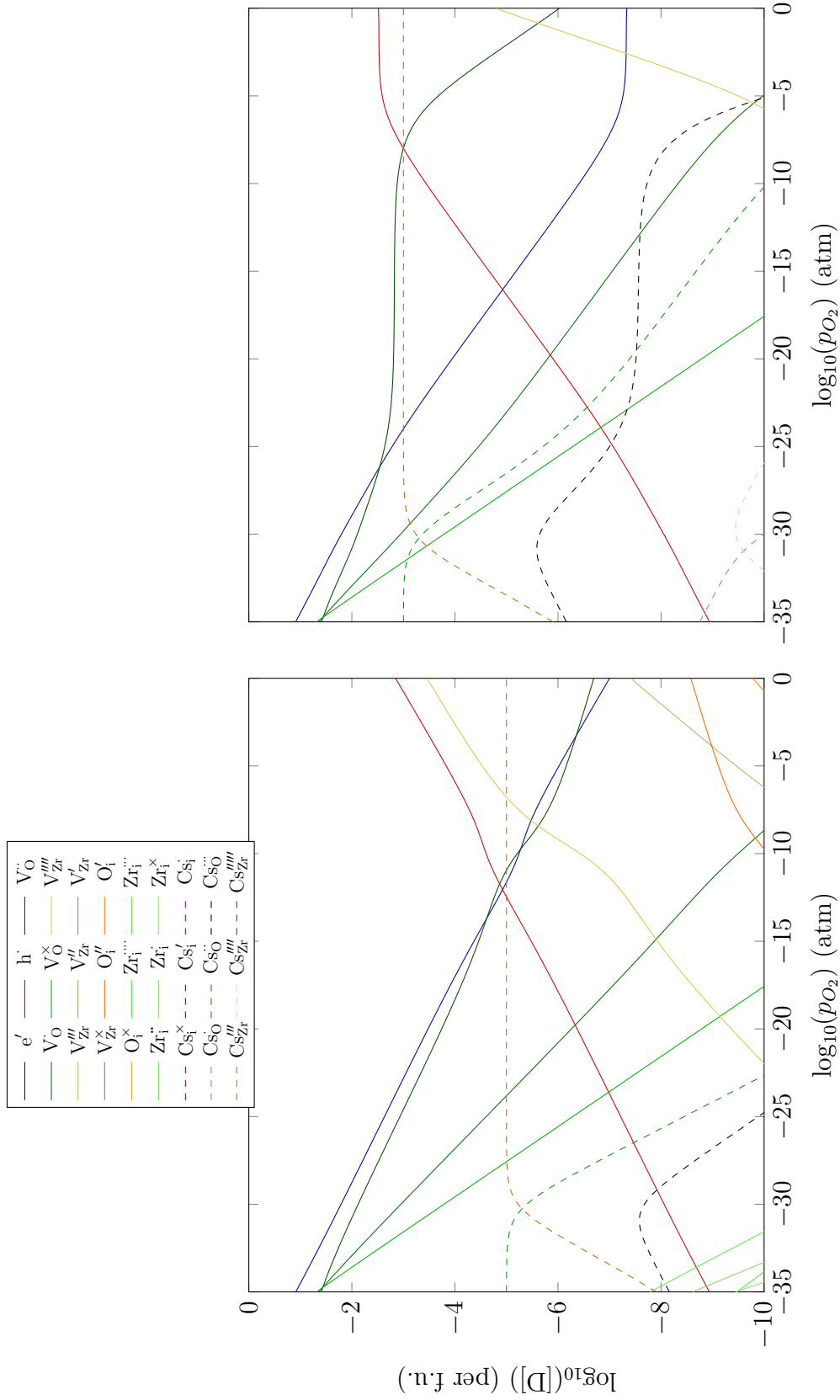


Figure 7.8: Tetragonal phase Brouwer diagrams of point defects at caesium concentrations of a) 10^{-5} and b) 10^{-3} , at a temperature of 1500 K. Space charge = 0

7.7 Summary

Filler

Chapter 8

Future work

8.1 Fission product empirical potential

In order to study the interaction of fission products with larger features in the cladding microstructure, such as dislocations and grain boundaries, it is necessary to develop empirical potentials for use in molecular dynamics simulations. Grain boundary transport is of particular interest, and this would require something on the order of 10^4 atoms to simulate to a reasonable degree of accuracy. This cannot be done using DFT currently due to the significant amount of computing resources required to run such a simulation.

The development of an iodine and xenon potential with ZrO_2 should be prioritised in order to run simulations to determine the migration of iodine within ZrO_2 , followed by the behaviour of xenon at the equilibrium iodine sites.

8.2 Grain boundary transport

Grain boundaries are interesting areas for studying species migration because diffusion towards the metal is expected to be more rapid through them than through bulk ZrO_2 .

8.3 Zr/ZrO/ZrO₂ interface study

The inner oxide is not a homogeneous structure, as described in Section 2. The presence of ZrO and even oxygen-saturated Zr metal will have an effect on the thermodynamic equilibria of different fission products. An interface study can be conducted using DFT, to determine stresses at the interfaces of Zr and ZrO, and ZrO and ZrO₂. Studying the aggregate effect of these interfaces on fission product behaviour may require larger molecular dynamics simulations, however. The crystal structure of the ZrO phase has been studied using both simulation and high-resolution electron microscopy, with two likely crystal structures being proposed [99]. Further atomistic studies must be conducted to determine the stability of each crystal structure of ZrO when constrained by ZrO₂ and oxygen-saturated Zr metal interfaces.

References

- [1] R French, S Glass, F Ohuchi, Y Xu, and W Ching. Experimental and theoretical determination of the electronic structure and optical properties of three phases of ZrO₂, 1994. (Cited on page xiii, 15)
- [2] C J Howard, R J Hill, and B E Reichert. Structures of ZrO₂ polymorphs at room temperature by high-resolution neutron powder diffraction. *Acta Crystallographica Section B*, 44(2):116–120, 1988. (Cited on page xiii, 18, 42, 52, 66)
- [3] R D Shannon. Revised effective ionic radii and systematic studies of interatomic distances in halides and chalcogenides. *Acta Crystallographica Section A*, 32(5):751–767, 1976. (Cited on page xiii, 23, 74)
- [4] A L Nichols, D L Aldama, and M Verpelli. Handbook of Nuclear Data for Safeguards: Database Extensions. *Nuclear Data Services*, 2008. (Cited on page xiv, 64, 88, 89)
- [5] A A Delucchi and A E Greendale. Fission Yields of Several Iodine Isotopes and Half-Life and Fission Yield of Te 135. *Physical Review C*, 1(4):1491, 1970. (Cited on page xiv, 64, 77, 88, 89)
- [6] N K Aras, M P Menon, and G E Gordon. Ranges of fragments from fission of U235 with thermal neutrons and the kinetic energy deficit. *Nuclear Physics*, 69(2):337–361, 1965. (Cited on page xv, 2)
- [7] BenRG. Plot of atomic isotopes, 2009. (Cited on page xv, 4)
- [8] Fastfission. Binding energy curve, 2007. (Cited on page xv, 5)

- [9] Joseph J Katz. *The Chemistry of the Actinide and Transactinide Elements (Volumes 1-5)*, volume 1. Springer Science & Business Media, 2007. (Cited on page xv, 11)
- [10] MH Rand, RJ Ackermann, F Gronvold, FL Oetting, and A Pattoret. The thermodynamic properties of the urania phase. *Revue Internationale des Hautes Temperatures et des Refractaires*, 15(4):355–365, 1978. (Cited on page xv, 11)
- [11] P-Y Chevalier, Evelyne Fischer, and Bertrand Cheynet. Progress in the thermodynamic modelling of the o–u binary system. *Journal of nuclear materials*, 303(1):1–28, 2002. (Cited on page xv, 11)
- [12] C Guéneau, M Baichi, D a al Labroche, C Chatillon, and Bo Sundman. Thermodynamic assessment of the uranium–oxygen system. *Journal of Nuclear Materials*, 304(2-3):161–175, 2002. (Cited on page xv, 11)
- [13] Chetvorno. Solid State Electronic Band Structure, 2017. (Cited on page xv, 14)
- [14] J. P. Abriata, J. Garcés, and R. Versaci. The O-Zr (Oxygen-Zirconium) system. *Bulletin of Alloy Phase Diagrams*, 1986. (Cited on page xv, 16)
- [15] X Xia. *Computational Modelling Study of Ytria-stabilized Zirconia Thesis submitted for the degree of Doctor of Philosophy Xin Xia*. PhD thesis, University College London, 2010. (Cited on page xv, 17)
- [16] Julian Haines, Jean Michel Léger, Steve Hull, Jean Pierre Petit, Altair S. Pereira, Claudio a. Perottoni, and Joao a. H. Jornada. Characterization of the Cotunnite-Type Phases of Zirconia and Hafnia. *Journal of the American Ceramic Society*, 1997. (Cited on page xv, 19)
- [17] A Gando, Y Gando, K Ichimura, H Ikeda, K Inoue, Y Kibe, Y Kishimoto, M Koga, Y Minekawa, T Mitsui, and Others. Partial radiogenic heat model for Earth revealed by geoneutrino measurements. *Nature Geoscience*, 4(9):647, 2011. (Cited on page xvi, 1, 20)

- [18] M. C. Payne, M. P. Teter, D. C. Allan, T. A. Arias, and J. D. Joannopoulos. Iterative minimization techniques for ab initio total-energy calculations: Molecular dynamics and conjugate gradients. *Reviews of Modern Physics*, 1992. (Cited on page xvi, 28)
- [19] T. R. England and B. F. Rider. *OECD Report*. NEA/NSC/DOC, 1992. (Cited on page xvii, 85)
- [20] W M Thornton. XV. The relation of oxygen to the heat of combustion of organic compounds. *The London, Edinburgh, and Dublin Philosophical Magazine and Journal of Science*, 33(194):196–203, 1917. (Cited on page 1)
- [21] Peter P King. Pressurization Of Nuclear Fuel Rods Using Laser Welding. *Proc.SPIE*, 0247:0247 – 0247 – 6, 1980. (Cited on page 6)
- [22] Tanweer Alam, Mohd Kaleem Khan, Manabendra Pathak, K Ravi, Ritu Singh, and S K Gupta. A review on the clad failure studies. *Nuclear Engineering and Design*, 241(9):3658–3677, 2011. (Cited on page 6, 8)
- [23] S Wisner and R B Adamson. Combined effects of radiation damage and hydrides on the ductility of Zircaloy-2. *Nuclear Engineering and Design*, 1998. (Cited on page 7)
- [24] Tomaž Einfeld, Odon Planinšek, and Klemen Hrovat. Methods of amorphization and investigation of the amorphous state, 2013. (Cited on page 7)
- [25] L M Wang, S X Wang, and R C Ewing. Amorphization of cubic zirconia by caesium-ion implantation. *Philosophical Magazine Letters*, 80(5):341–347, 2000. (Cited on page 7, 66)
- [26] K E Sickafus, H Matzke, T Hartmann, K Yasuda, J A Valdez, P Chodak III, M Nastasi, and R A Verrall. Radiation damage effects in zirconia. *Journal of Nuclear Materials*, 274(1):66–77, 1999. (Cited on page 7, 66)
- [27] B Cox. Pellet-clad interaction (PCI) failures of zirconium alloy fuel cladding — A review. *Journal of Nuclear Materials*, 172(3):249–292, 1990. (Cited on page 8, 64, 77, 88)
- [28] K C Radford and R J Bratton. Zirconia electrolyte cells - Part 2 Electrical properties. *Journal of Materials Science*, 14(1):66–69, 1979. (Cited on page 9)

- [29] O J Whittemore and D W Marshall. Fused stabilized zirconia and refractories. *Journal of the American Ceramic Society*, 35(4):85–89, 1952. (Cited on page 9)
- [30] L Wang and T Liang. Ceramics for high level radioactive waste solidification. *Journal of Advanced Ceramics*, 1(3):194–203, 2012. (Cited on page 9)
- [31] R A Causey, D F Cowgill, and R H Nilson. Review of the oxidation rate of zirconium alloys. Technical report, Sandia National Laboratories, 2005. (Cited on page 10, 65, 78)
- [32] F Garzarolli, H Seidel, R Tricot, and J P Gros. Oxide growth mechanism on zirconium alloys. In *Zirconium in the Nuclear Industry: Ninth International Symposium*. ASTM International, 1991. (Cited on page 10)
- [33] J K Dawson, G Long, W E Seddon, and J F White. The kinetics and mechanism of the oxidation of zircaloy-2 at 350–500° C. *Journal of Nuclear Materials*, 25(2):179–200, 1968. (Cited on page 10)
- [34] H A Porte, J G Schnizlein, R C Vogel, and D F Fischer. Oxidation of zirconium and zirconium alloys. *Journal of the Electrochemical Society*, 107(6):506–515, 1960. (Cited on page 10)
- [35] T K Gupta, J H Bechtold, R C Kuznicki, L H Cadoff, and B R Rossing. Stabilization of tetragonal phase in polycrystalline zirconia. *Journal of Materials Science*, 12(12):2421–2426, 1977. (Cited on page 19)
- [36] F A Kröger and H J Vink. Relations between the concentrations of imperfections in crystalline solids. In *Solid state physics*, volume 3, pages 307–435. Elsevier, 1956. (Cited on page 23)
- [37] W Kohn and L J Sham. Self-consistent equations including exchange and correlation effects. *Physical Review*, 140(4A), 1965. (Cited on page 25)
- [38] P J Hasnip. Introduction to First-Principles Modelling and CASTEP, 2010. (Cited on page 31)

- [39] A Samanta, T Lenosky, and J Li. Thermodynamic stability of oxygen point defects in cubic Zirconia. *arXiv preprint arXiv:1009.5567*, 2010. (Cited on page 35)
- [40] S T Murphy and N D M Hine. Point Defects and Non-stoichiometry in Li_2TiO_3 . *Chemistry of Materials*, 26(4):1629–1638, 2014. (Cited on page 36, 54, 68, 79, 92)
- [41] I Batyrev, A Alavi, and M Finnis. Equilibrium and adhesion of Nb/sapphire: The effect of oxygen partial pressure. *Physical Review B*, 62(7):4698–4706, 2000. (Cited on page 36, 55, 69, 80, 92)
- [42] A Y Lozovoi, A Alavi, and M W Finnis. Surface energy and the early stages of oxidation of NiAl(110). *Computer Physics Communications*, 137(1):174–194, 2001. (Cited on page 36, 55, 69, 80, 92)
- [43] M W Finnis, A Y Lozovoi, and A Alavi. The oxidation of NiAl: What can we learn from ab initio calculations? *Annual Review of Materials Research*, 35(1):167–207, 2005. (Cited on page 36, 55, 69, 80, 92)
- [44] B D C Bell. *The influence of alloying elements on the corrosion of Zr-based nuclear fuel cladding using density functional theory*. PhD thesis, Ph. D. Thesis, Imperial College London, Department of Materials, 2016. (Cited on page 37, 55, 69, 81, 93)
- [45] T Ukaji and K Kuchitsu. Effect of temperature on the molecular structure of iodine observed by gas electron diffraction. *Bulletin of the Chemical Society of Japan*, 39(10):2153–2156, 1966. (Cited on page 43)
- [46] T Hahn. *International tables for crystallography: Brief teaching edition of volume A, Space-group symmetry*, volume 1. Kluwer Academic Pub, 1996. (Cited on page 47)
- [47] Lionel Desgranges, Gianguido Baldinozzi, Gurvan Rousseau, Jean Claude Nièpce, and Gilbert Calvarin. Neutron diffraction study of the in situ oxidation of UO_2 . *Inorganic Chemistry*, 2009. (Cited on page 51)
- [48] G Teufer. The crystal structure of tetragonal ZrO_2 . *Acta Crystallographica*, 15(11):1187, 1962. (Cited on page 52, 66)

- [49] J X Zheng, G Ceder, T Maxisch, W K Chim, and W K Choi. First-principles study of native point defects in hafnia and zirconia. *Physical review B*, 75(10):104112, 2007. (Cited on page 53)
- [50] A S Foster, V B Sulimov, F L Gejo, A L Shluger, and R M Nieminen. Modelling of point defects in monoclinic zirconia. *Journal of non-crystalline solids*, 303(1):101–107, 2002. (Cited on page 53)
- [51] A S Foster, V B Sulimov, F L Gejo, A L Shluger, and R M Nieminen. Structure and electrical levels of point defects in monoclinic zirconia. *Physical Review B*, 64(22):224108, 2001. (Cited on page 53)
- [52] M Youssef and B Yildiz. Intrinsic point-defect equilibria in tetragonal ZrO₂: Density functional theory analysis with finite-temperature effects. *Physical Review B*, 86(14):144109, 2012. (Cited on page 53)
- [53] V M Orera, R I Merino, Y Chen, R Cases, and P J Alonso. Intrinsic electron and hole defects in stabilized zirconia single crystals. *Physical Review B*, 42(16):9782, 1990. (Cited on page 53)
- [54] C Jiang, X-Y. Liu, and K E Sickafus. First-principles prediction of the thermodynamic stability of xenon in monoclinic, tetragonal, and yttrium-stabilized cubic ZrO₂. *Physical Review B*, 83(5):52103, 2011. (Cited on page 53)
- [55] W C Mackrodt and P M Woodrow. Theoretical estimates of point defect energies in cubic zirconia. *Journal of the American Ceramic Society*, 69(3):277–280, 1986. (Cited on page 53)
- [56] C Århammar, C M Araújo, and R Ahuja. Energetics of Al doping and intrinsic defects in monoclinic and cubic zirconia: First-principles calculations. *Physical Review B*, 80(11):115208, 2009. (Cited on page 53)
- [57] S J Clark, M D Segall, C J Pickard, P J Hasnip, M J Probert, K Refson, and M C Payne. First principles methods using CASTEP. *Zeitschrift für Kristallographie*, 220(5-6-2005):567–570, 2005. (Cited on page 53, 67, 79, 91)

- [58] J Perdew, K Burke, and M Ernzerhof. Generalized Gradient Approximation Made Simple. *Physical review letters*, 77(18):3865–3868, 1996. (Cited on page 53, 67, 79, 91)
- [59] H Monkhorst and J Pack. Special points for Brillouin zone integrations. *Physical Review B*, 13(12):5188–5192, 6 1976. (Cited on page 53, 67, 79, 91)
- [60] P Pulay. Convergence acceleration of iterative sequences. the case of scf iteration. *Chemical Physics Letters*, 73(2):393–398, 7 1980. (Cited on page 53, 67, 79, 91)
- [61] P A Burr, S C Middleburgh, and R W Grimes. Crystal structure, thermodynamics, magnetism and disorder properties of Be–Fe–Al intermetallics. *Journal of Alloys and Compounds*, 639:111–122, 2015. (Cited on page 53)
- [62] M L Jackson, P A Burr, and R W Grimes. Resolving the structure of TiBe. *Culham Centre for Fusion Energy*, 2016. (Cited on page 53)
- [63] Patrick A Burr and Michael William Donald Cooper. Importance of elastic finite-size effects: Neutral defects in ionic compounds. *Physical Review B*, 96(9):94107, 2017. (Cited on page 56)
- [64] H S Rosenbaum. The interaction of iodine with Zircaloy-2. *Electrochemical Technology (US) Absorbed by J. Electrochem. Soc.*, 4, 1966. (Cited on page 64)
- [65] M Fregonese, C Régnard, L Rouillon, T Magnin, F Lefebvre, and C Lemaignan. Failure Mechanisms of irradiated Zr alloys related to PCI: Activated slip systems, localized strains, and iodine-induced stress corrosion cracking. In *Zirconium in the Nuclear Industry: Twelfth International Symposium*. ASTM International, 2000. (Cited on page 64, 65)
- [66] P S Sidky. Iodine stress corrosion cracking of Zircaloy reactor cladding: iodine chemistry (a review). *Journal of Nuclear Materials*, 256(1):1–17, 1998. (Cited on page 64, 77)
- [67] T. J. Kennett and H. G. Thode. Mass Spectrometrically Determined Independent Yields of I 128, I 130, Br 80, and Br 82 for U 233, U 235, and Pu 239 Fission. *Physical Review*, 103:323, 1956. (Cited on page 64, 77, 89)

- [68] B C Purkayastha and G R Martin. The Yields of ^{129}I in Natural and in Neutron-Induced Fission of Uranium. *Canadian Journal of Chemistry*, 34(3):293–300, 1956. (Cited on page 64, 77, 89)
- [69] N Imanishi, I Fujiwara, and T Nishi. Independent isomer yields of Sb and Te isotopes in thermal-neutron fission of ^{233}U , ^{235}U and ^{239}Pu . *Nuclear Physics A*, 263(1):141–149, 1976. (Cited on page 64, 77, 89)
- [70] S Amiel and H Feldstein. Odd-even systematics in neutron fission yields of U 233 and U 235. *Physical Review C*, 11(3):845, 1975. (Cited on page 64, 77, 89)
- [71] C Degueldre, M Pouchon, M Döbeli, K Sickafus, K Hojou, G Ledergerber, and S Abolhassani-Dadras. Behaviour of implanted xenon in yttria-stabilised zirconia as inert matrix of a nuclear fuel. *Journal of nuclear materials*, 289(1):115–121, 2001. (Cited on page 64, 78, 89)
- [72] M Peehs and G Kaspar. Experimental investigations of caesium and iodine release from irradiated UO_2 . *High Temperatures-High Pressures*, 14(5):517–522, 1982. (Cited on page 65)
- [73] S K Yagnik, B C Chang, and D J Sunderland. Effect of PWR Re-start Ramp Rate on Pellet-cladding Interactions. In *Pellet-clad Interaction in Water Reactor Fuels*. International Nuclear Information System, 2005. (Cited on page 65)
- [74] C Nonon, J C Menard, S Lansiaart, J Noiroit, S Martin, G M Decroix, O Rabouille, C Delafoy, and B Petitprez. PCI behaviour of chromium oxide-doped fuel. In *Pellet-clad Interaction in Water Reactor Fuels*. International Nuclear Information System, 2005. (Cited on page 65)
- [75] J H Yang, K S Kim, I H Nam, J S Oh, D Kim, Y W Rhee, and J H Kim. Effect of step wise variation of oxygen potential during the isothermal sintering on the grain growth behavior in Cr_2O_3 doped UO_2 pellets. *Journal of Nuclear Materials*, 429(1):25–33, 2012. (Cited on page 65)

- [76] S B Farina, G S Duffo, and J R Galvele. Stress Corrosion Cracking of Zircaloy-4 in Halide Solutions: Effect of Temperature. *Materials Research*, 5(2):107–112, 2002. (Cited on page 65)
- [77] M L Rossi and C D Taylor. First-principles insights into the nature of zirconium–iodine interactions and the initiation of iodine-induced stress–corrosion cracking. *Journal of Nuclear Materials*, 458:1–10, 2015. (Cited on page 65, 66)
- [78] A Legris and C Domain. Ab initio atomic-scale modelling of iodine effects on hcp zirconium. *Philosophical Magazine*, 85(4-7):589–595, 2005. (Cited on page 65)
- [79] G Carlot and D Davesne. Energetically favourable sites of iodine atoms in zirconium: an ab initio approach. *Philosophical Magazine B*, 82(1):73–83, 2002. (Cited on page 65)
- [80] N Ni, S Lozano-Perez, M L Jenkins, C English, G D W Smith, J M Sykes, and C R M Grovenor. Porosity in oxides on zirconium fuel cladding alloys, and its importance in controlling oxidation rates. *Scripta Materialia*, 62(8):564–567, 2010. (Cited on page 66)
- [81] M V Glazoff, A Tokuhiko, S N Rashkeev, and P Sabharwall. Oxidation and hydrogen uptake in zirconium, Zircaloy-2 and Zircaloy-4: Computational thermodynamics and ab initio calculations. *Journal of Nuclear Materials*, 444(1-3):65–75, 2014. (Cited on page 66)
- [82] A Couet, A T Motta, and R J Comstock. Hydrogen pickup measurements in zirconium alloys: Relation to oxidation kinetics. *Journal of Nuclear Materials*, 451(1-3):1–13, 2014. (Cited on page 66)
- [83] P Hofmann and J Spino. Stress corrosion cracking of Zircaloy-4 cladding at elevated temperatures and its relevance to transient LWR fuel rod behaviour. *Journal of Nuclear Materials*, 125(1):85–95, 1984. (Cited on page 75)
- [84] M Bojinov, V Karastoyanov, P Kinnunen, and T Saario. Influence of water chemistry on the corrosion mechanism of a zirconium–niobium alloy in simulated light water reactor coolant conditions. *Corrosion Science*, 52(1):54–67, 2010. (Cited on page 75)

- [85] M Fregonese, G Delette, G Ducros, and F Lefebvre. Amount of iodine responsible for I-SCC of Zircaloy-4 in PCI-conditions: recoil-implanted and thermally released iodine. *Nuclear Engineering and Design*, 186(3):307–322, 1998. (Cited on page 77)
- [86] D Le Boulch, L Fournier, and C Sainte-Catherine. Testing and Modelling Iodine-Induced Stress Corrosion Cracking in Stress-Relieved Zircaloy-4. *Nuclear Science - Seminar Proceedings*, 2004. (Cited on page 77)
- [87] IAEA. Evaluated Nuclear Data File. *Nuclear Data Services*, 2015. (Cited on page 77, 88)
- [88] A. Kenich, M. R. Wenman, and R. W. Grimes. Iodine defect energies and equilibria in ZrO_2 . *Journal of Nuclear Materials*, 511:390–395, 2018. (Cited on page 78, 88)
- [89] U Bergenlid and H Mogard. Experimental observations of the PCI failure occurrence on power ramping. *Pellet-Cladding Interaction in Water Reactors*, page 121, 1980. (Cited on page 78)
- [90] J C Wood and J R Kelm. Effects of irradiation on the iodine-induced stress corrosion cracking of Candu zircaloy fuel cladding. *Res Mechanica*, 8(3):127–161, 1983. (Cited on page 78)
- [91] P J Pankaskie. Mechanistic considerations pertinent to the PCI fuel failure phenomenon. *Pellet-Cladding Interaction in Water Reactors*, page 255, 1981. (Cited on page 78)
- [92] B D C Bell, S T Murphy, P A Burr, R W Grimes, and M R Wenman. Accommodation of tin in tetragonal ZrO_2 . *Journal of Applied Physics*, 117(8), 2015. (Cited on page 79)
- [93] S T Murphy, M W D Cooper, and R W Grimes. Point defects and non-stoichiometry in thoria. *Solid State Ionics*, 267:80–87, 12 2014. (Cited on page 80)
- [94] M M Bé, V Chisté, C Dulieu, E Browne, V Chechev, N Kuzmenko, R Helmer, A Nichols, E Schönfeld, and R Dersch. Table of radionuclides (Vol. 1-A= 1 to 150). *Bureau International des Poids et Mesures, France: Sèvres*, 2004. (Cited on page 88)

- [95] M M Bé, V Chisté, C Dulieu, X Mougeot, V P Chechev, N K Kuzmenko, F G Kondev, A Luca, M Galán, and A L Nichols. Table of Radionuclides (Vol. 6–A= 22 to 242). *Monographie BIPM-5*, 2011. (Cited on page 88)
- [96] M M Bé, V Chisté, C Dulieu, E Browne, V Chechev, N Kuzmenko, F G Kondev, A Luca, M Galán, and A Pearce. Table of radionuclides (Vol. 4–A= 133 to 252). *BIPM, Sevres*, 2008. (Cited on page 88)
- [97] A A Sonzogni. Nuclear Data Sheets for A = 134. *Nuclear Data Sheets*, 103(1):1–182, 9 2004. (Cited on page 88)
- [98] B Singh, A A Rodionov, and Y L Khazov. Nuclear Data Sheets for A = 135. *Nuclear Data Sheets*, 109(3):517–698, 3 2008. (Cited on page 88)
- [99] R J Nicholls, N Ni, S Lozano-Perez, A London, D W McComb, P D Nellist, C R M Grovenor, C J Pickard, and J R Yates. Crystal structure of the ZrO phase at zirconium/zirconium oxide interfaces. *Advanced Engineering Materials*, 17(2):211–215, 2015. (Cited on page 101)

Appendix A

ParaSweep

ParaSweep is a generalised sensitivity analysis visualisation tool which was developed during this project. Initially, it was built to help visualise the effects of changing single parameters in Brouwer diagrams, such as temperature or concentration of defects.

Appendix B

CASTEP and HPC Scripts

Throughout the course of this work, many useful scripts were created to help with preparing CASTEP jobs and analysing their outputs. These scripts have been made available online and for free at <https://github.com/v1thesource/CASTEP>. The purpose of open-sourcing these scripts is to simplify the experience for new users of CASTEP and help them save a considerable amount of time.